Influence of mixed phases on the optoelectronic properties of Cs–Pb–Br compounds

vorgelegt von
M. Eng.
Sebastián Caicedo Dávila
ORCID: 0000-0001-5135-2979

an der Fakultät II - Mathematik und Naturwissenschaften
der Technischen Universität Berlin
zur Erlangung des akademischen Grades

Doktor der Naturwissenschaften
-Dr. rer. nat.-

genehmigte Dissertation

Promotionsausschuss:
Vorsitzender: Prof. Dr. Stephan Reitzenstein
Gutachter: Prof. Dr. Michael Lehmann
Gutachter: Prof. Dr. Roland Scheer
Gutachter: Prof. Dr. Leeor Kronik
Gutachter: PD Dr. Daniel Abou-Ras
Tag der wissenschaftlichen Aussprache: 15. September 2020

Berlin 2020

Zusammenfassung

In der vorliegenden Dissertation wird ein korrelativer Ansatz zur Untersuchung des Einflusses der Phasenmischung auf die optischen Eigenschaften von Cs–Pb–Br-Verbindungen vorgestellt. Dieses Materialsystem weist drei ternäre Phasen, $CsPbBr_3$, Cs_4PbBr_6 und $CsPb_2Br_5$ auf, die in Cs–Pb–Br Materialien vorkommen, wenn sie mit verschiedenen Methoden hergestellt werden. Die Koexistenz beeinflusst die Lichtemission und kann somit die Leistung der auf diesen Verbindungen basierenden optoelektronischen Bauelemente beeinflussen.

Motiviert durch die offenen Debatten über die grüne Emission von Cs–Pb–Br untersuchte ich die Struktur, Zusammensetzung und optischen Eigenschaften von Materialien mit gemischten Phasen mittels Röntgenbeugung, energiedispersiver Röntgenspektroskopie, Kathodolumineszenz (CL) und Photolumineszenz (PL) Spektroskopie. Mit diesen Techniken wurde die räumliche Phasenverteilung von Cs–Pb–Br-Dünnschichten mit einer Auflösung von unter 50 nm untersucht. Es wurde festgestellt, dass bei drei verschiedenen Depositionsmethoden mindestens zwei der ternären Phasen koexistieren Dieses Ergebnis stimmte sehr gut mit ab-initio-Berechnungen überein, die sehr ähnliche Bildungsenthalpien für die drei Phasen zeigten.

Zunächst wurde der Einfluss der Phasenumwandlung auf die Lumineszenz von $CsPbBr_3$/$CsPb_2Br_5$-Dünnschichten untersucht. In-situ-Experimente zeigten, dass der Phasenumwandlung Kristallstrukturübergänge von $CsPbBr_3$ vorausgehen und dass sie nur bei erhöhten Temperaturen von über 583 K auftreten. PL und mikroskopische, korrelative Analysen zeigten, dass das Tempern die Defektdichte an der Grenzfläche $CsPbBr_3$/$CsPb_2Br_5$ erhöht, was zur Verringerung der grünen Lumineszenz beiträgt.

Schließlich wurden grün lumineszierende Cs_4PbBr_6 und $CsPb_2Br_5$ mittels PL und CL untersucht, wobei eingebettete, grün emittierende $CsPbBr_3$ Nanokristalle mit erhöhter Emissionsausbeute entdeckt wurden. Für Cs_4PbBr_6 und $CsPb_2Br_5$ wurden spektrale Blau- und Rotverschiebungen gemessen. Diese Emissionsverschiebungen wurden durch ein Effektive-Masse Annäherungsmodell erklärt, das die unterschiedlichen Bandlückenenergien und Dielektrizitätskonstnaten zwischen den eingebetteten Nanokristallen und dem Wirtsmaterial berücksichtigt. Der experimentell-theoretische Ansatz in der vorliegenden Arbeit erwies sich als wertvolles Werkzeug zur Untersuchung des Cs–Pb–Br-Materialsystems und trug zum besseren Verständnis ihrer optoelektronischen Eigenschaften bei.

Abstract

The current dissertation presents a correlative approach to investigate the influence of phase mixture on the optical properties of Cs–Pb–Br compounds. This material system exhibits three ternary phases, $CsPbBr_3$, Cs_4PbBr_6 and $CsPb_2Br_5$, which coexist in Cs–Pb–Br materials when deposited by various methods. The coexistence influences the light emission and by extension can affect the performance of the optoelectronic devices based on these compounds.

Motivated by the open debates regarding the green emission from Cs–Pb–Br, I investigated the structure, composition, and optical properties of mixed-phase materials by means of X-ray diffraction, energy-dispersive X-ray spectroscopy, cathodoluminescence (CL) and photoluminescence (PL) spectroscopy. Using these techniques, the spatial phase distribution of Cs–Pb–Br thin films was investigated, with a resolution of below 50 nm. It was found that for three different deposition methods, at least two of the ternary phases coexist. This result agreed very well with ab-initio calculations showing very similar formation enthalpies for the three phases.

Secondly, the influence of the phase transformation on the luminescence of $CsPbBr_3/CsPb_2Br_5$ thin films was investigated. In-situ experiments revealed that phase transformation is preceded by crystal structure transitions of $CsPbBr_3$ and that it only occurs at elevated temperatures of above 583 K. PL and microscopic, correlative analyses showed that annealing increases the defect density at the $CsPbBr_3/CsPb_2Br_5$ interface, which contributes to the quenching of the green luminescence.

Finally, green luminescent Cs_4PbBr_6 and $CsPb_2Br_5$ were investigated by means of PL and CL, which revealed embedded green-emitting $CsPbBr_3$ nanocrystals with enhanced emission yield. Spectral blue and red shifts were measured for Cs_4PbBr_6 and $CsPb_2Br_5$. These emission shifts were explained by an effective mass approximation model, which considers band-gap energy differences and dielectric mismatch between the embedded nanocrystals and the host material. The experimental-theoretical approach in the present thesis was found to be a valuable tool to investigate the Cs–Pb–Br material system and helped improving the understanding of their optoelectronic properties.

Acknowledgements

I want to gratefully acknowledge the financial support by the Helmholtz International Research School HI-SCORE (HIRS-0008), coordinated by my supervisor, PD Dr. Daniel Abou-Ras, who I would like to thank for his constant support and encouragement to my work during the past three years. Thank you for your advice for my work during the thesis, during other exciting projects and for contributing for my growth as a scientist and as a person. I also like to thank Prof. Leeor Kronik from the Weizmann Institute in Israel, who co-supervised this thesis and guided me, not only through some fascinating theoretical and computational work, but also with some career advice, which I am sure will help me become a better scientist. I would also like to thank Prof. Michael Lehmann from the TU-Berlin for his valuable input and detailed comments on the research presented in this thesis. I am grateful with Prof. Roland Scheer of University of Halle for taking the time to read my thesis in detail and for motivating an encouraging scientific discussion.

I want to thank Abou-Ras' group at the Helmholtz-Zentrum Berlin, whose members became a sort of family that supported me, not only on my scientific work, but also in many others aspects. Sasha, Hannah and Max, with whom I shared so many moments, the good ones and the not so good ones as well. Thanks for the constant support and your friendship, my *Ph.D. siblings*. To Uli (Ulrike Bloeck) who was always ready to help, to give me advice and spend some minutes in conversations that made the day nicer. Thanks are also due to Karin Regelin, who was always ready to help me swim through HZB's sometimes complex administrative processes, and always ready to share a laugh. From Kronik's group I'd specially want to thank Ayala Cohen, who mentored me during my time at the Weizmann and became a good friend. I also want to thank Georgia Prokopiou, who made my stay in Rehovot so enjoyable and also became a good friend, who is a brilliant scientist, always ready to answer my questions.

Concluding this thesis would have not been possible without the help of great scientists, from whom I learned a lot during these years, who helped me by performing measurements, synthesizing samples, pointing me to the right literature reference, or discussing ideas. In no special order, I would like to thank René Gunder, Dr. Frederike Lehmann, Dr. Sergiu Levcenco, Dr, Joachim Breternitz, Dr. José Márquez Prieto, Dr. Aboma Merdasa, Dr. Klaus Schwarzburg, Dr. Katja Höflich, Dr. Thomas Unold, Dr. Eva Unger, Carolin Rehermann, Dr. Robert Lovrinčić, Dr. Michael Sendner, Dr. Christian Müller, Prof. Dr. Klaus Lips, Holger Kropf, Harald Stapel, Jürgen Bundesmann, Prof. Dr. Susan Schorr, Dr. Hannes Hempel, Prof. Dr. Dieter Neher, Pietro Caprioglio, Dr. Martin Stortelfoht, Christian Wolff, Dr. Oana Cojocaru-Mirédin and Dr. Martin Kärgell.

When I came to Berlin I had the fortune to already have some friends and make new ones. Thanks to Flavia and Dustin for their friendship and support when I just arrived and through

these years. And to Javi, I can just say, I am lucky to have found the best person to share my life with. And last — but never least — I would like to thank my family, specially Xime and my mother Nancy, who unconditionally supported my decision to pursue research as a way of life. Thanks for everything.

Table of Contents

List of Figures

List of Tables

List of abbreviations

AFM Atomic force microscope/microscopy

APD Avalanche Photodiode

APT Atom probe tomography

AsB Angle-selective backscattered electron detector

BSE Backscatteres electron

CCD Charge-coupled device

CL Cathodoluminescence

CMOS Complementary metal-oxide semiconductor

DCM Dichloromethane

DFPT Density functional perturbation theory

DFT Density functional theory

DMF Dimethylformamide

DMSO Dimethyl sulfoxide

EDX Energy-dispersive X-ray spectroscopy. Also abbreviated as EDS in the literature

EFA Envelope function approximation

EMA Effective mass approximation

EsB Energy-selective backscattered electron detector

FIB Focused ion beam

FWHM Full width at half maximum

GIXRD Grazing-incidence X-ray diffraction

HaP Halide perovskite

LED Light-emitting diode

PBE Perdew-Burke-Ernzehof form of the generalized gradient approximation of the exchange correlation functional

Pb-HaP Lead-halide perovskite

PL Photoluminescence

PLQY Photoluminescence quantum yield

PMT Photomumtiplier tube

PV Photovoltaics

SE Secondary electrons

SEM Scanning electron microscope/microscopy

SOC Spin-orbit coupling interaction

TEM Transmission electron microscope/microscopy

TRPL Time-resolved photoluminescence

XRD X-ray diffraction

List of physical quantities and variables

a_B Effective exciton Bohr radius

a, b, c Lattice constants

β Peak integral breadth, equals area over height

ΔH Formation enthalpy

d_{hkl} Interplanar distance of the planes given by the hkl Miller's indices

e Electron (fundamental) charge

E_b Primary electron beam energy

E_{em} Emission energy

E_{exc} Exciton energy

E_g Band-gap energy

ε Relative permittivity/dielectric constant

ε_0 Vacuum permittivity

ε_i Relative permittivity of material/region i

E_{tot} Total energy

G/G_{eh} Carrier generation rate

H Full width at half maximum

$H^{(i)}(\mathbf{r}_i)$ Single-particle Hamiltonian of particle i

$H(\mathbf{r}_e, \mathbf{r}_h)$ Electron-hole Hamiltonian

h Planck's constant

$\hbar$ Reduced Planck's constant equals $\frac{h}{2\pi}$

hkl Miller's indices

I_b Primary electron beam current

λ Wavelength

m_i^* Effective mass of particle i

μ^* Reduced effective electron-hole mass

n, p Electron/hole densities

n_0, p_0 Equilibrium electron/hole densities

$\Phi(\mathbf{r}_i)$ Single particle (i) wave function

$\Psi(\mathbf{r}_e, \mathbf{r}_h)$ Exciton wave function

R Recombination rate

R_e Guren penetration depth

S_{eh}^2 Electron-hole overlap

T Temperature

τ Minority carrier lifetime

V_i^{pot} External potential for particle i

V_i^{self} Self-interaction potential of particle i

V_c Electron-hole Coulomb potential

Z Atomic number

1

Introduction

The international goals to stabilize the global mean temperature and to limit the increase of this temperature to below 2 °C require that the net antropogenic CO_2 emissions are decreased to zero by the year 2050 [1, 2]. However, this goal is already under threat due to the projected emissions of existing and commited fossil-fuel energy infrastructure [1]. Thus, renewable energy production is of vital importance in the efforts to ensure the future of the planet. The importance of photovoltaic (PV) technology is major. It accounted for $\sim 27\,\%$ of Germany's energy production in 2019 [3] and it is fundamental in the scenarios proposed to achieved the energy goals [2]. Together with energy production, more efficient electrical and electronic devices are also fundamental to achieve this goal.

Halide perovskite materials are very attractive candidates for PV, light-emission, and photodetection applications [4–6]. Despite the outstanding progress on efficiency, fundamental understanding of the origins of the outstanding optoelectronic properties that make halide perovskites so attractive is still far from being complete [7] and advanced macro- and microscopic characterization, coupled with theoretical modeling, are necessary to investigate the properties of these materials.

Among the halide perovskites, $CsPbBr_3$ is a stable compound. It has been shown to exhibit remarkable thermal and long-term stability in ambient air [5, 8–10], while performing similarly as the hybrid organic-inorganic perovskites. [5, 11], with power conversion efficiencies of above 10 % [12]. Most promising is the application of $CsPbBr_3$ as active layer in light emitting diodes (LED) [5, 13–15]. In the past years, extensive research in this application has lead to an increase in the external quantum efficiency of perovskite LED from below 1 % to above 20 %[13, 15] for thin-film based devices. Finally, stimulated emission in $CsPbBr_3$ has also been investigated for potential applications in lasers. This material is very attractive to cover the spectral green gap from 530 to 610 nm [16, 17] and to replace diode-pumped, solid state green lasers in many applications [18].

However, this halide perovskite also exhibit two additional, thermodynamically-stable ternary phases: the $PbBr_2$-rich $CsPb_2Br_5$ and the CsBr-rich Cs_4PbBr_6. These phases exhibit a higher band-gap energy and a different crystal structures than that of $CsPbBr_3$. These two phases have been shown to coexist in single crystals, thin films, powders and

nanocrystals.[19–26]. The influence of this coexistence of the different phases as well as their phase transformations on the optical properties in Cs–Pb–Br materials is still unclear.

In the present thesis, a combination of photoluminescence (PL) spectroscopy, X-ray diffraction (XRD) and correlative scanning electron microscopy (SEM) techniques — energy-dispersive X-ray spectroscopy (EDX) and cathodoluminescence (CL) — is used to investigate the phase distribution, the phase transformation and the influence on the optical properties of perovskite-related Cs–Pb–Br materials. Experimental evidence and theoretical modeling are presented to contribute to answer the following questions: Does $CsPb_2Br_5$ passivate the surface of $CsPbBr_3$ in thin films and does it reduce nonradiative recombination? At what temperature does the phase transformation $CsPb_2Br_5 \longrightarrow CsPbBr_3 + PbBr_2$ take place? What is the origin of the detected green luminescence in Cs_4PbBr_6 and $CsPb_2Br_5$, and how does the phase mixture influence the emission wavelength?

The present thesis is organized as follows:

- Chapter 2 gives a brief overview of the structure and the most attractive properties of halide perovskites for optoelectronic devices, focusing on the Cs–Pb–Br material system. The structures of the different ternary phases are presented and the implications of the dimensionality of each phase on the electronic structure are discussed briefly. Some of the open questions regarding the material system, which serve as starting point for the research presented here, are also presented.

- Chapter 3 introduces the experimental techniques and the theoretical basis for the model used throughout the thesis. The basic physics of XRD, PL spectroscopy, SEM, EDX and CL are explained and some important considerations and limitations of the experiments described in Chapters 4 to 6 are described. The effective mass approximation (EMA) and the concept of dielectric confinement — the basis of the model presented in Chapter 6 are explained.

- In Chapter 4 the coexistence of the different ternary phases is studied theoretically and experimentally measured by means of XRD and PL in thin films deposited by different methods. The spatial phase distribution is investigated by means of microscopic, correlative compositional (EDX) and optoelectronic (CL) mapping.

- In Chapter 5 the phase transformation $CsPb_2Br_5 \longrightarrow CsPbBr_3 + PbBr_2$ at elevated temperatures is investigated by means of in-situ XRD. The effect of the phase transformation on the luminescence is investigated by means of PL and time-resolved PL. Finally, the distribution of the recombination centers prior and after annealing is investigated by microscopic CL-EDX correlative analysis.

- Chapter 6 presents the results of temperature- and intensity-dependent PL on $CsPbBr_3$, and green-luminescent $CsPb_2Br_5$ and Cs_4PbBr_6. The origin of the green luminescence of the latter phases is revealed by CL-EDX microscopy. Finally, a theoretical EMA model is implemented, which aims to explain the differences in emission intensity and wavelength among the different phases.

- Chapter 7 summarizes the conclusions obtained from the experimental and theoretical investigations and presents the possible future work that can be derived from the research

presented in this thesis. The relevance of the correlative macro- and microscopic approach used during the development of the present thesis, for the Cs–Pb–Br and other perovskite materials system is highlighted.

2

The Cs-Pb-Br material system

A perovskite is a mineral of calcium titanate, with chemical formula $CaTiO_3$ that was first discovered by the German mineralogist Gustav Rose in 1839, and named after the Russian mineralogist Lev Perovski [27] . Various compound materials — such as oxides, like $SrTiO_3$ and $BaTiO_3$ — may exhibit perovskite-type structure, with stoichiometry ABX_3 and a crystal structure that consists of BX_6 corner-sharing octahedra in three dimensions, with the A site, within the cuboctahedral cavity of each unit cell, as shown in Figure 2.1 [28]. Depending on their compositions, perovskite-like materials can be insulating or semiconductive. These materials usually exhibit a cubic or tetragonal crystal structure [27], but orthorhombic, trigonal and monoclinic polymorphs are also accesible, depending on the tilting and rotation of the BX_6 octahedra [28].

2.1 Lead-halide perovskites for optoelectronics

Of special interest are the so called lead-halide perovskites (Pb-HaPs). In these materials, the X site corresponds to a monovalent halide anion, the B site is a divalent metal cation i.e., Pb^{2+}, and the A site can be a monovalent metal or organic cation, as illustrated in Figure 2.1. The unusual chemistry and physics of Pb-HaP have been studied since the 1980s [28–30]. The potential of Pb-HaP in photovoltaics (PV) started gaining interest since the appearance of the first solar cell, based on hybrid organic-inorganic (organic A cation) Pb-HaP [31]. Research on Pb-HaP materials and PV applications boomed during the last decade because of the rapid increase in power conversion efficiency of solar cells, from 3.8 % in 2009 [31] to over 25 % for single-junction solar cells and up to 28 % for multi-junction cells in 2019 [32], and the low-cost processing of the solar cells, involving mostly low-temperature solution chemistry.

In spite of this huge progress in power conversion efficiency and of the outstanding optoelectronic properties that Pb-HaP exhibit, such as high photoluminescence quantum yields, large diffusion lengths and lifetimes, there is still lack of understanding of many structure-property relationship in halide perovskites, such as the long order range in a material synthesized by relative low temperature solution chemistry, which produces a material with sharp absorption edges, the apparent less detrimental effect of defects and grain boundaries,

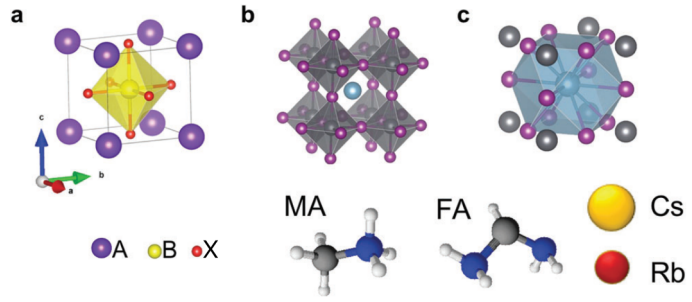

Figure 2.1: (a) General perovskite-type crystal structure with ABX_3 stoichiometry. The A site is represented with purple spheres, the B sites with yellow ones (inside the cages) and the X site in red. (b) The BX_6 octahedrally coordination around the center A site. (c) The cuboctahedral coordination around the A site. The elements or molecules for the A site in a Pb-HaP (Pb as the B site) are shown. Figure adapted from Correa-Baena et al. [6]

which results in low nonradiative recombination rates, the ion migration which leads to ionic conductance and phase separation, and the coexistence of different phases within one material [7].

Therefore, investigations of the microscopic properties of Pb-HaPs are of fundamental importance, in order to understand the structure-property relationships of these materials, which in turn can lead to optimized material synthesis and device design. In the present thesis, I investigated the correlation of microscopic optoelectronic properties and composition using scanning electron microscopy techniques, with macroscopic structural and optical properties, using X-ray diffraction and photoluminescence spectroscopy on the inorganic halide perovskite $CsPbBr_3$, and related secondary phases.

Although the hybrid organic-inorganic Pb-HaP are the materials most investigated of this kind, on account of their widely spread use as absorber material in solar cells [33, 34], inorganic $CsPbBr_3$ has also gained interest in the community because of its high moisture and thermal stability, compared with the organic-inorganic counterparts [8–10], having similar performances in optoelectronic devices [11]. This high band gap ($\sim$2.4 eV) Pb-HaP has been used as active material in light emitting diodes (LEDs) [13–15], photodetectors [35–37], solar cells [12, 38–42], and recently also in lasers [16]. $CsPbBr_3$ also offers higher stability under the electron beam than hybrid perovskites. This phenomenon has been observed by means of electron beam current (EBIC) by Klein-Kedem, Cahen, and Hodes [43]. Xiao et al. [44] studied the mechanisms by which the electron beam can damage the perovskite material by means of cathodoluminescence (CL, see Section 3.3.3). These authors found that both, knock-on defects and localized heating, contribute most to the damage. Both effects were less damaging in $CsPbI_3$ than in the organic-inorganic material (see Figure 2.2).

Inorganic Pb-HaPs share some of the very interesting properties that make hybrid perovskites so unique, and many phenomena have been studied on the inorganic materials as a model system. These include phase separation [45], polaron formation [46], anharmonic local polar fluctuations of the lattice [47], defect energetics [48], among others. Therefore, in the present thesis I focused on studying the properties of the $CsPbBr_3$ perovskite and related materials.

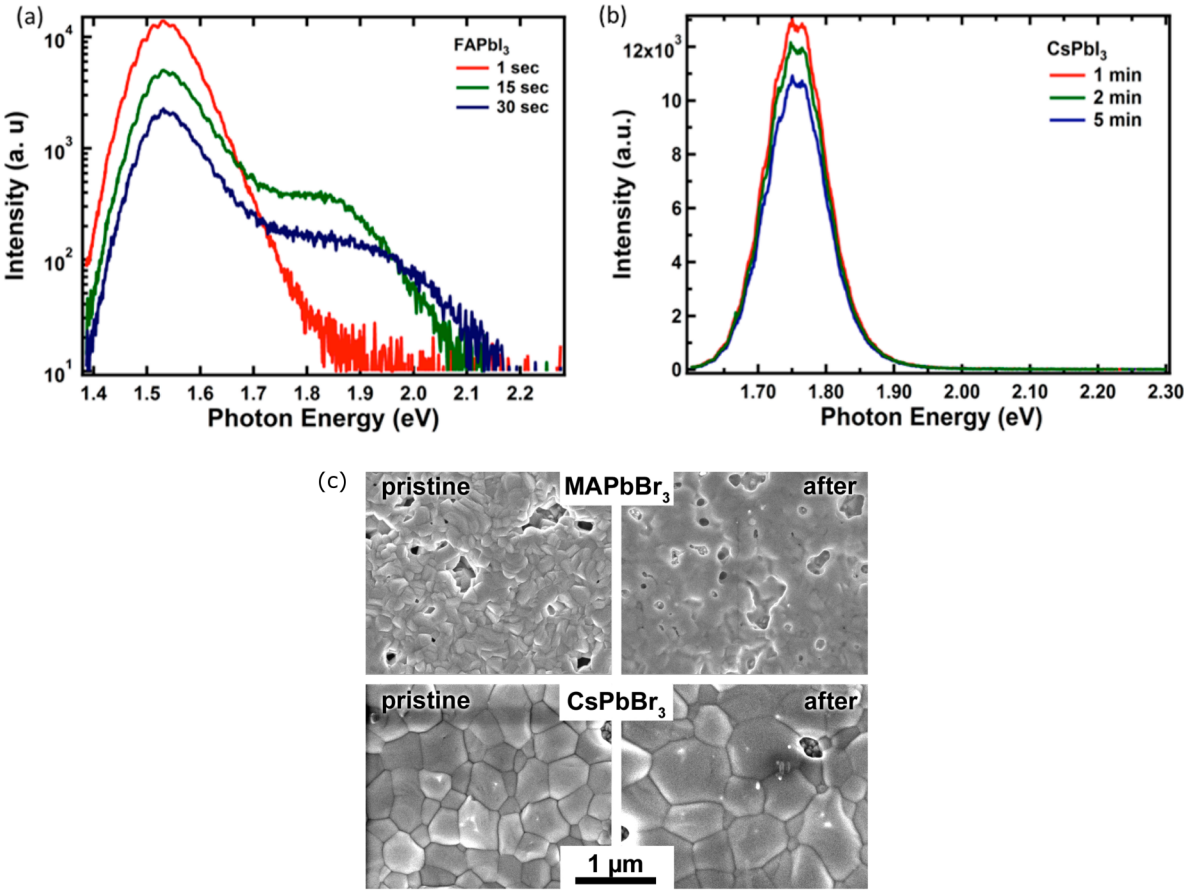

Figure 2.2: CL spectra of (a) $FAPbI_3$ (hybrid) and (b) $CsPbI_3$ measured upon electron beam exposure using an acceleration voltage of 5 kV and beam current of 12 nA within different exposure times. The rapid change and quenching of the CL spectrum of the hybrid perovskite contrasts with the more stable CL spectrum of the inorganic counterpart. Reproduced from Xiao et al. [44]. (c) SEM images if pristine and after-exposure (3 kV, 8 nA) hybrid ($MAPbBr_3$) and inorganic ($CsPbBr_3$) perovskites. The damage is evidently less in the inorganic material. Reproduced from Klein-Kedem, Cahen, and Hodes [43]

2.2 The Cs–Pb–Br material system

The $CsPbBr_3$ perovskite is particular within the inorganic Pb-HaPs since it belongs to a material system, together with two other thermodynamically stable ternary phases — the two-dimensional (2D) $CsPb_2Br_5$ and the zero-dimensional (0D) Cs_4PbBr_6. These phases can coexist in the different forms of the material: thin films, nanocrystals, powder and single crystals.[19, 20, 22–26, 49]

The atomic structure of the various ternary phases in the Cs-Pb-Br material system are shown in Figure 2.3. The CsBr-rich phase, also known as the 0D perovskite-related phase [20, 22, 50, 51], exhibits isolated $PbBr_6$ octahedra separated by Cs atoms. This phase crystallizes at room temperature in the trigonal crystal system with space group $R\bar{3}c$[50] and is a direct band gap semiconductor with a band-gap energy of ∼4.0 eV[30, 52–55]. The $PbBr_2$-rich phase, $CsPb_2Br_5$, is sometimes referred to as a 2D perovskite-related phase. It is consists of edge-sharing $PbBr_8$ bicapped trigonal prisms, [56] separated by planes of Cs atoms in a tetragonal crystal system with space group $I4/mcm$[57, 58]. This phase exhibits an indirect band-gap energy in the ultraviolet (UV) spectral region, with values reported between ∼3.35

and 3.87 eV [19, 56, 58] (this range is appropriate considering the phonon absorption at room temperature has not been reported).

Finally, the $CsPbBr_3$ phase consists of corner-sharing $PbBr_6$ octahedra with a Cs atom caged inside the lead-halide framework. This phase exhibits various crystal structures depending on the temperature. Strictly speaking, only the high-temperature (>130 °C), cubic structure can be considered a perovskite: ABX_3 stoichiometry, aristotype structure with space group $Pm\bar{3}m$, octahedral coordination of the B-cation (Pb) and corner-sharing octahedra [59, 60]. This phase also exhibits a distorted perovskite form at lower temperatures; a tetragonal structure (space group $P4/mbm$) between 80 and 130 °C, and an orthorhombic structure (space group $Pbnm$) at temperatures below 80 °C, which is the one relevant at room temperature. For simplicity, these three crystal systems of the $CsPbBr_3$ will be further on referred to as perovskites indistinctly. The perovskite phase is a direct band gap semiconductor with a band-gap energy of ∼2.4 eV[5, 11, 29, 38, 61].

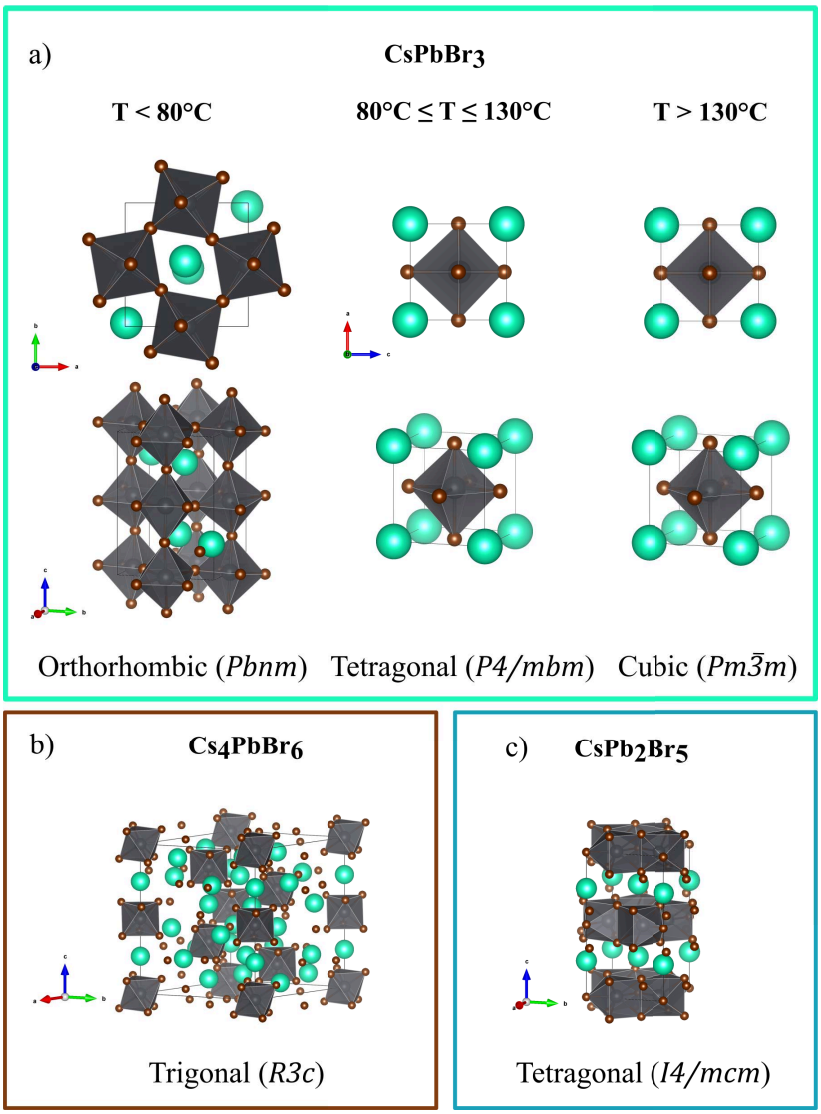

Figure 2.3: Ternary phases in the Cs–Pb–Br material system: (a) the perovskite $CsPbBr_3$ in all its different crystal structures, (b) the "zero-dimensional" and (c) "two-dimensional" perovskite-related structures (non-perovskites)

2.2.1 The "zero dimensional" Cs_4PbBr_6

In spite of its large band-gap energy, Cs_4PbBr_6 many times exhibits a strong green luminescence [30, 62–66]. The origins of such luminescence is still unclear and a matter of debate with two main opinions prevailing: (1) the green luminescence is intrinsic to the Cs_4PbBr_6, generated by defect-mediated radiative recombination, and (2) the green luminescence originates from confined $CsPbBr_3$ nanoscale domains embedded in the Cs_4PbBr_6 bulk [51] (see Figure 2.4). A very elegant summary of this issue was provided by Akkerman, Abdelhady, and Manna [51]. Here, I reproduce some of the most important aspects reported in the literature. It is important then to discuss some fundamental aspects of the electronic structure and the optical characterization in this material.

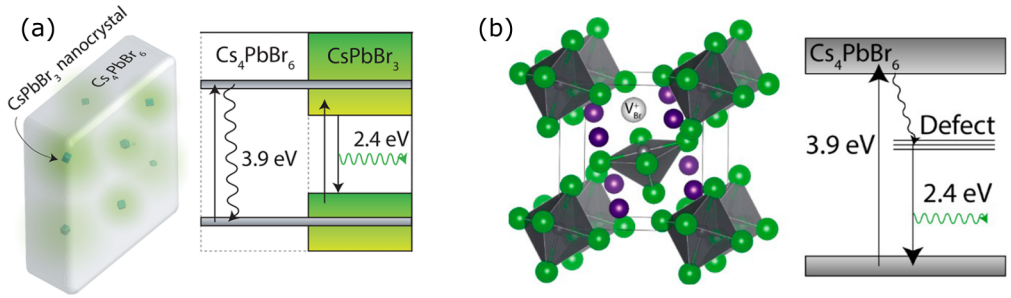

Figure 2.4: Recombination mechanisms proposed in the literature to explain the green luminescence in Cs_4PbBr_6. (a) Embedded $CsPbBr_3$ nanoinclusions with high PLQY due to quantum confinement, and (b) defect mediated radiative recombination via mid-gap levels, created by Br vacancies (V_{Br}). Figure adapted from ref. [51]

The crystal structure described at the beginning of this Section implicates some changes in the electronic structure of Cs_4PbBr_6, compared with that of $CsPbBr_3$. Perhaps the most important one is that, owing to the separation between $PbBr_6$ octahedra, the p orbitals of the Br — which mostly form the valence band — overlap with the s and p orbitals of only one Pb ion — mostly conduction band. This is in strong contrast to the orbital overlap in $CsPbBr_3$, where p orbitals of Br exhibit a good overlap with 2 adjacent Pb ions (see Figure 2.5). The low coupling between $PbBr_6$ means that the band-gap energy is larger due to low hybridization, there is low band dispersion (i.e., large carrier effective masses), and also that the electronic transitions (excitons) are confined to isolated octahedra [51, 67].

The electronic structure of defects in Cs_4PbBr_6 has also been studied. Yin et al. [68] calculated the defect formation energies and charge transition levels of defects in Cs_4PbBr_6, and found that the Br vacancy (V_{Br}) level can be positioned about 2.25 eV above the valence band maximum. However, the defect formation energy for V_{Br} is high in moderate and Br-rich conditions, which are usually the case to synthesize the material [51, 63, 64, 69]. Additionally, Han et al. [67] calculated the excitation and emission energies of excitons bound to V_{Br}, as well as the exciton binding energy and Stokes shift. They found very large Stokes shift (~ 0.8 eV) and exciton binding energy (~ 0.6 eV), — consistent with the confinement of the wavefunction in the individual octahedra — with emission energies in the range of the green luminescence (~ 2.5 eV).

Regarding the optical characterization of this particular material, the photoluminescence (PL) spectrum observed in green luminescent Cs_4PbBr_6 closely resembles that of $CsPbBr_3$

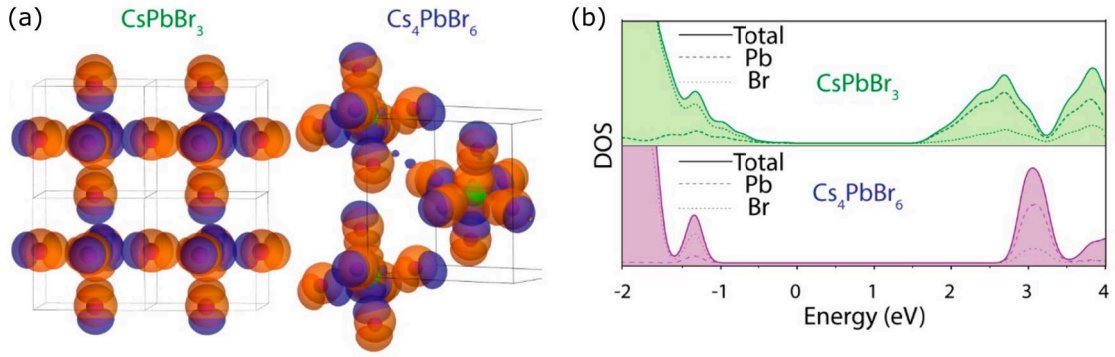

Figure 2.5: (a) Schematic representation of the overlap of p orbitals of Br (p_i, with i=x, y or z shown, depending on the orientation of the relevant overlapping orbital) with s an p orbitals of Pb, for $CsPbBr_3$ and Cs_4PbBr_6. (b) Density of state (DOS) and DOS projected on the Pb and Br orbitals, showing the contributions to the conduction and valence bands. Figure adapted from Akkerman, Abdelhady, and Manna [51]

nanocrystals: it exhibits a sharp peak, with full width at half maximum (FWHM) usually between 15–25 nm [51, 63, 70, 71], short lifetimes in the ns range, a small stokes shift of about 30 meV [51, 62, 71] (see Figure 2.6).

The small stokes shift, the absorption edge in the visible range and the very sharp transition point to the conclusion that the green luminescence in fact stems from $CsPbBr_3$ nanoinclusions. The theoretical evidence, further supports this conclusion, since the emission of the exciton bound to the V_{Br} should exhibit a very large Stokes shift. Additionally, the sharp emission contrasts with the known defect emission in layered Ruddlesden-Popper layered materials, which exhibit a very broad emission, and again, a large Stokes shift, and similar confinement of the exciton to their layers [51, 72, 73]. Furthermore, the nature of defects in Cs_4PbBr_6 is still unclear. Cohen et al. [48] have shown that the nature of defects in $CsPbBr_3$ is dynamic, and that the charge transition level of the V_{Br} can change due to the anharmonic vibration of the lattice. If defect dynamics in Cs_4PbBr_6 would resemble those in $CsPbBr_3$ this would change the interpretation given by Yin et al. [68]. More recently, Ma et al. [74] studied the PL of Cs_4PbBr_6 as a function of pressure, comparing it with that of $CsPbBr_3$ nanocrystals, and the calculated defect position as a function of pressure. Their results show an incongruence between change defect level and PL energy positions, but a good agreement of the trend

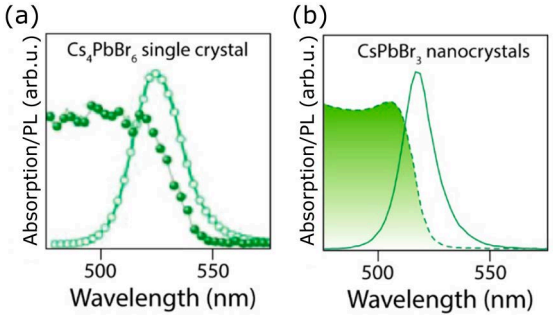

Figure 2.6: Absorption and PL spectra of (a) Cs_4PbBr_6 single crystal and (b) $CsPbBr_3$ nanocrystals. Notice the remarkable resemblence between PL width and Stokes shift of both spectra. Adapted from refs. [22, 51, 71]

with that of $CsPbBr_3$ nanocrystals, supporting again that the green luminescence stems from $CsPbBr_3$ nanocrystals embedded in Cs_4PbBr_6.

2.2.2 The "two-dimensional" $CsPb_2Br_5$

Another phase in the Cs–Pb–Br material system is the so-called 2D $CsPb_2Br_5$. Similar to the Cs_4PbBr_6, the atomic structure of this phase also imposes some confinement of the wavefunction to the $PbBr_8$ planes, as shown by the very low dispersion of the A–M, Γ–Z and R–X paths in the Brilloin zone — parallel to *c* direction [56] (see Figure 2.7). Also, in spite the large, indirect band gap, Wang et al. [75] first reported green luminescence from allegedly pure $CsPb_2Br_5$ nanoplatelets with high photoluminescence quantum yield (PLQY). Similar findings were published in References [23, 76, 77], who attribute the green luminescence to defects, similar to the claim made for Cs_4PbBr_6. Li and coworkers have used $CsPb_2Br_5$ nanoparticles embedded in borosilicate glasses to study their temperature stability, and noticed that the green luminescence decreases with temperature and at the same time the PL spectra red shifts [78, 79]. However, no clear explanation was given for these results.

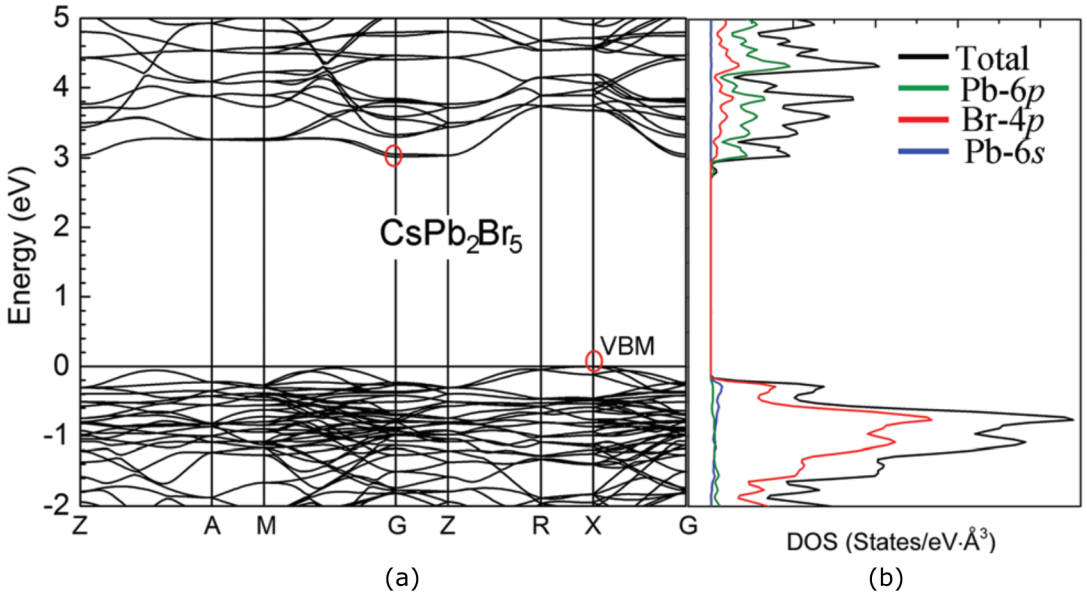

Figure 2.7: (a) Band structure of $CsPb_2Br_5$ showing the low dispersion caused by the reduced dimensionality of the atomic structure. (b) DOS and PDOS of $CsPb_2Br_5$, showing the contributions of p orbitals of Pb to the conduction band and of the p orbitals of Br to the valence band. Figure adapted from ref. [56]

Li et al. [80] investigated how luminescent $CsPbBr_3$ nanocubes can be transformed into $CsPb_2Br_5$ nanosheets by reacting in excess of $PbBr_2$. They measured the evolution of the PL at different reaction times, and found that at long reaction times the PL and absorption edge corresponding to the $CsPbBr_3$ vanished. However, they also measured an unexplained initial increase in the green PL peak. These results support the hypothesis that the green luminescence in $CsPb_2Br_5$ is not intrinsic to the material, but it rather stems from inclusions of $CsPbBr_3$, which have been supported by other works on $CsPb_2Br_5$ and on $CsPbBr_3/CsPb_2Br_5$ core-shell nanostructures with very similar optical properties [81, 82].

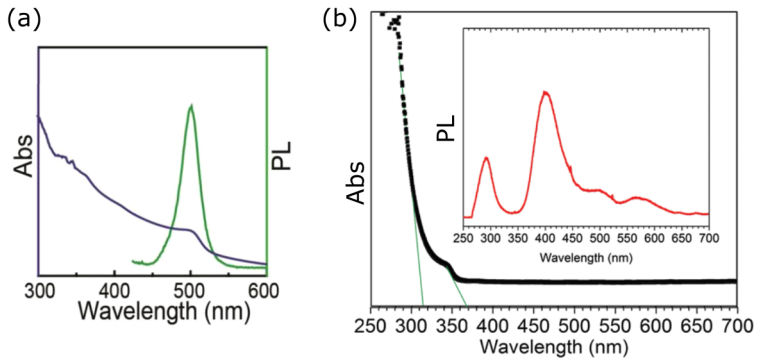

Figure 2.8: PL and absorption spectra of a (a) luminescent and (b) non-luminescent $CsPb_2Br_5$. The non-luminescent $CsPb_2Br_5$ does not exhibit an absorption edge in the visible range, and also no sharp green emission, but rather a broad one characteristic of defect transitions. Figure reproduced from Refs. [56, 76]

Comparing the PL and absorption spectra of luminescent and non-luminescent $CsPb_2Br_5$ (see Figure 2.8) leads to the assumption that the luminescence is due to $CsPbBr_3$ inclusions. The PL and absorption spectra of luminescent $CsPb_2Br_5$ are almost identical to that of luminescent Cs_4PbBr_6, discussed in Section 2.2.1, and exhibit an absorption edge around 500 nm, and a sharp emission peak at the same range, with a small Stokes shift. This optical properties have been reported by different authors in luminescent $CsPb_2Br_5$ [23, 75, 76, 79]. By contrast, non-luminescent $CsPb_2Br_5$ exhibits no absorption edge in the visible range, and two well defined radiative transitions around 300 and 400 nm, which can be assigned to band-to-band and exciton recombination. Defect-related transitions can also be detected around 500 and 600 nm (and towards the yellow and red spectral region at 170 K) as broad transitions with lower intensity [56]. Thus, the experimental evidence gives rise to the assumption that the green luminescence in $CsPb_2Br_5$, just as in Cs_4PbBr_6, is caused by embedded $CsPbBr_3$.

2.2.3 Some open questions on the optical properties in Cs–Pb–Br

Although it can be concluded that the green luminescence in Cs_4PbBr_6 and $CsPb_2Br_5$ is originated from confined $CsPbBr_3$ nanocrystals, which explains the high PLQY, the origin of some of the observed properties remains unknown. As pointed out by Akkerman, Abdelhady, and Manna [51], the PL peak position in $CsPbBr_3/Cs_4PbBr_6$ composites always lies between 515 and 524 nm, which would imply a narrow range of sizes. Smaller sizes would imply a blue shift which is not observed in most of the cases, and when observed it is unstable and shifts towards green, as shown by Chen et al. [55]. On the other hand, the luminescence of $CsPbBr_3/CsPb_2Br_5$ composites — when prepared from $CsPbBr_3$ nanocrystals — can exhibit a red shift, which is counterintuitive from an expected size reduction [23]. Additionally, a red shift (together with lost in PLQY) can also be observed when annealing luminescent $CsPb_2Br_5$ [79]. These phenomena need a comprehensive explanation.

Furthermore, there is still uncertainty whether the high PLQY is only due to the quantum confinement in the nanocrystals, or there is an influence of the secondary phases on the optical properties of $CsPbBr_3$. For instance, Quan et al. [54] suggested that the lattice match between $CsPbBr_3$ and Cs_4PbBr_6 aids the passivation of defects at the surface of $CsPbBr_3$, enhancing

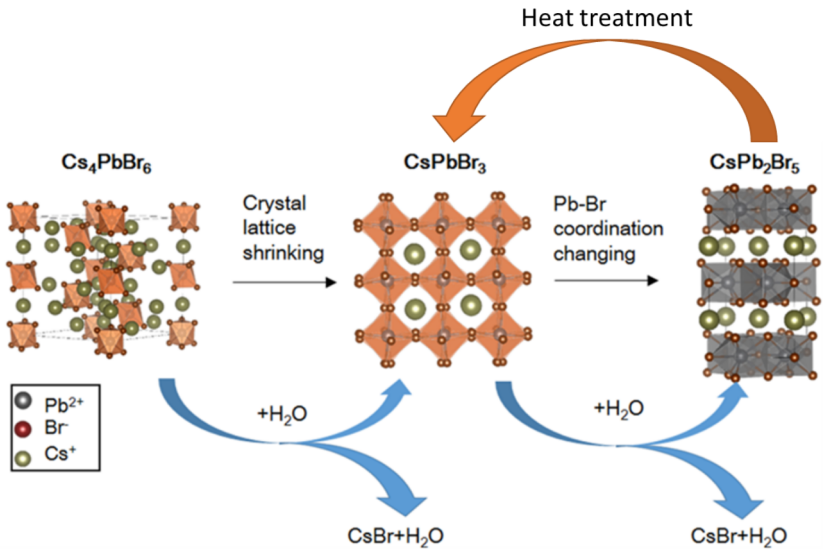

Figure 2.9: Shematic representation of the water- and temperature-induced phase transformations among the Cs–Pb–Br ternary phases. Figure adapted from ref. [49]

the luminescence. In contrast, Ling et al. [83] suggested that shallow traps at the interface between the materials can enhance the PL. Similar passivation hypotheses have been proposed for $CsPb_2Br_5$, due to the enhanced luminescence, and the enhanced solar cell efficiency in the presence of this secondary phase [39, 82, 84]. However, it is still unclear whether the passivation effect is in fact responsible for the enhanced luminescence. Other possible mechanisms for the high PLQY have been proposed. For instance, [85] proposed that the difference in dielectric constants between Cs_4PbBr_6 and $CsPbBr_3$ could result in dielectric confinement (see Section 3.4.3), which in turn enhances the oscillator strength and increases radiative recombination. Tan et al. [86] proposed a similar mechanisms for $CsPbBr_3/CsPb_2Br_5$ systems. However, an in-depth study of this effect on these materials is not available.

Another important aspect that can affect the optical properties in Cs–Pb–Br materials is the transformation between phases. Liu et al. [49] showed the influence of the solvent in the phase transformation among the Cs–Pb–Br ternary phases. They found that the solvent can influence the coordination of Pb^{2+} ions, influencing the resulting phase. Dimethyl sulfoxide (DMSO), for instance, favors 6-fold coordination of Pb^{2+} and the formation of Cs_4PbBr_6 and $CsPbBr_3$. Water, on the other hand, favors 8-fold coordination and the formation of $CsPb_2Br_5$. Water can also precipitate CsBr and induce the transformation $Cs_4PbBr_6 \longrightarrow CsPbBr_3 \longrightarrow CsPb_2Br_5$, as shown in Figure 2.9. More recently, Maity and Pradhan [25] have also reported that the transformation from $CsPbBr_3$ to $CsPb_2Br_5$ is reversible under heat treatment. These phase transformatios help explaining some of the effects observed in the literature when Cs–Pb–Br systems are subject to humidity or annealing [23, 79, 86, 87].

In the present thesis, I focus on studying three main topics, related to the Cs–Pb–Br system: (1) the phase coexistence and microscopic phase distribution in thin films deposited with different methods in Chapter 4, (2) the temperature-induced phase transformation in thin films and its implication in the optical properties in Chapter 5. The passivation hypothesis was investigated by a series of macro- and microscopic characterization methods. (3) Finally, in Chapter 6 the issues of the peak position and enhanced PLQY in $CsPbBr_3/Cs_4PbBr_6$ and

$CsPbBr_3/CsPb_2Br_5$ mixed-phase materials are investigated by comparing PL spectroscopy, and microscopy results with a theoretical model that considers quantum and dielectric confinement in $CsPbBr_3$.

3

Experimental and simulation methods

In order to study the physical properties of the Cs–Pb–Br material system, in the present thesis a set of different experimental techniques that allow to investigate the structure, composition and optoelectronic properties of thin film materials were combined. In the first three sections of the present chapter, the basic principles of the experimental techniques used throughout the thesis are presented. The specifics of the setup — equipment, parameters, etc.— for each experiment are presented together with the results in Chapters 4 to 6. In the final section the theoretical framework used to model the optical properties of the mixed-phase Cs–Pb–Br materials, in Chapter 6, is presented.

It is important to mention that the description of the techniques and theory given in this chapter is far from being complete or exhaustive. However, it describes the basic physical principles of the experiments and theory necessary to understand the results described in this thesis.

3.1 X-ray diffraction

X-rays can be elastically and coherently scattered — i.e., diffracted — when they interact with a solid, crystalline material. This elastic scattering process can be explained in terms of classical electromagnetic theory. The oscillating electromagnetic field of the X-rays interacts with the electrons in the material and makes them oscillate with the same frequency. In turn, electrons in an atom become a source of electromagnetic radiation with the same frequency and wavelength. The contribution of the radiation of all the atoms in a plane generates constructive and destructive interference of the scattered radiation, which limits the scattered x-rays to specific scattering angles with respect to the impinging beam.

For a family of planes with hkl Miller's indexes, the intensity of the diffracted X-rays also depends on the geometry of the crystal and the wavelength. As shown in Figure 3.1, two parallel beams — 1 and 2 — incident at an angle θ with respect to two parallel planes, separated by an interplanar distance of d_{hkl}, are diffracted in the beams 1' and 2'. Constructive interference only takes place when the path length difference between $\bar{1}2$ and $1'\bar{2}'$ is an integer

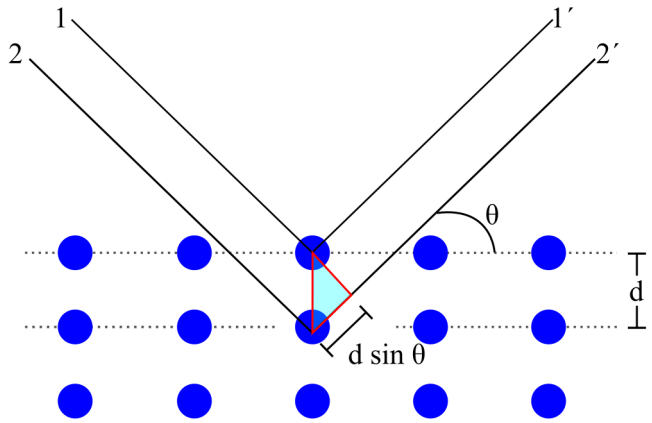

Figure 3.1: Schematic of the reflection of X-rays on lattice planes. The interplanar distance is $d = d_{hkl}$ and the Bragg or diffraction angle is θ.

multiple of the incident X-ray wavelength, λ. This condition is summarized in Bragg's law of diffraction:

$$\lambda n = 2d_{hkl} \sin\theta \tag{3.1}$$

where n is a positive integer that ensures Bragg condition for diffraction. The family of planes with interplanar distance d_{hkl} reflect the X-rays at the same angle 2θ with respect to the incident beam.

If the material exhibits crystallites with random orientation (e.g. a powder), the diffracted intensities are uniform and depend on the atomic positions within the crystal. If the crystallites are not randomly distributed, some Bragg peaks (also called Bragg reflections, or Bragg peaks from here on) can exhibit low intensity. This is indicative of preferred orientation or texture. This can be observed in polycrystalline thin films and is a consequence of the crystallization or recrystallization process.

In most of the X-ray diffraction (XRD) experiments presented throughout this thesis, a Bragg-Brentano, or $\theta - 2\theta$ configuration was used, in which the θ angle of both the X-ray source and the detector is changed, so that the 2θ angle can be swept during the measurement (see Figure 3.2a).

3.1.1 Grazing incidence XRD

For very thin films measured in Bragg-Brentano configuration, the path length of the X-rays in the sample is short, which can lead to low peak intensity and bad signal-to-background ratio. To address this issue, grazing-incidence X-ray diffraction (GIXRD) is a good option. This is a low angle geometry, in which the X-ray source is kept at a shallow angle ($\sim 1°$) and the detector is scanned over the 2θ range of interest. Since the angle of the incident X-rays is kept fixed, the planes that are not parallel to the surface also contribute to the diffraction, which increases the peak intensity.

Since the path length is increased, the interaction volume with the thin film also increases. The surface sensitivity is also increased by the large projection length of the X-rays over the

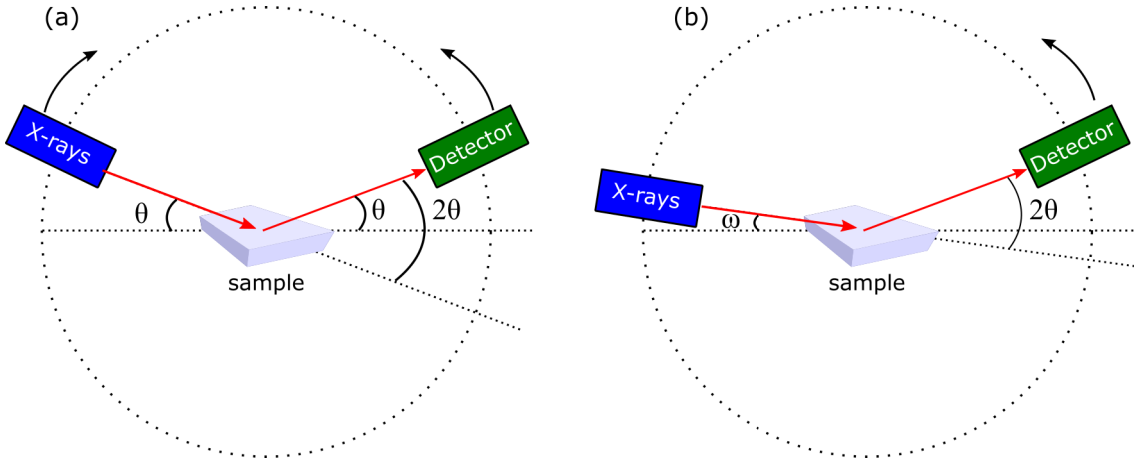

Figure 3.2: Schematic of the geometries used in the present thesis: (a) Bragg-Brentano, in which both the X-ray source and detector move, and (b) GIXRD, in which the X-ray source is fixed at a shallow angle ω, and the detector is scanned over 2θ.

surface of the sample, achieved by the shallow angle. A graphical summary of both geometries is presented in Figure 3.2.

The measured XRD patterns can be used to identify the different phases present in a material by comparing the peak positions with those of reference materials, since it is related to the interplanar spacing of a family of hkl planes. In the case of the different phases in the Cs–Pb–Br material system, crystallographic information is available in the literature [88].

XRD offers a lot of additional information — depending on the quality of the measurement, of course. In this thesis, the Le Bail method is used for fitting of peak intensities and extraction of cell parameters. Methods based in the integral intensity and width analysis are used to extract volume fractions and domain sizes. The methods are shortly described in the following:

- **The Le Bail method** uses an iterative 2 step process to extract the cell parameters using least-squares methods. For each diffraction peak, an initial to-fit peak with arbitrary intensity $I(calc)$ is set. The intensity is taken as the sum of the intensity values at points along the peak profile after partitioning ($y_i(calc) = \sum_n y_i(n)$). This intensity and can include several overlapping peaks (accounting for different phases, for instance). The values of the observed profiles for each individual peaks can be calculated as:

$$I_{obs}(n) = \sum_i y_i(obs) \frac{y_i(n)}{y_i(calc)} \tag{3.2}$$

  These values can be used for least-squares fitting of the profile, and the estimation of the cell parameters a, b, c, α, β and γ using the model of a reference system.

- **Integral intensities and breadths** can be used to estimate the volume fraction of a phase and the domain size and micro strain. It is straightforward that the intensity of the peaks associated to a specific phase is higher if the volume of that phase is larger. However, the width of a peak can change due to instrumental factors or changes in the sample. The instrumental broadening arise from several sources, like the X-ray source not being perfectly monochromatic, divergence of the incident or diffracted beams, among several others (see references [89, 90] for further details). The broadening

produced by the sample can be caused by changes in the coherently diffracting domain size (sometimes referred to as crystallite size), lattice distortions (microstrain) due to dislocations, concentration gradients and stackig faults. There are different approaches to separate the instrumental, domain size and strain contributions from the breadth of the peak profile. These are discussed in more detail in section 5.2.2, where they are used to evaluate the measured data.

3.2 Photoluminescence spectroscopy

When light with sufficient energy excites a material and brings it out of thermal equilibrium, electrons can move to higher energy states, creating an electron-hole pair. When electrons transition from a higher occupied states to lower unoccupied states, i.e. recombine with holes, spontaneous light emission can occur. This phenomenon of light emission upon light excitation is known as photoluminescence (PL).

3.2.1 Radiative transitions

PL emission can occur in different ways. Figure 3.3 shows a simplified summary of the radiative transitions (the ones leading to luminescence) in semiconductors. Here the ones considered during the thesis are briefly described:

1. Band-to-band recombination, in which an electron in the conduction band recombines with a hole in the valence band. This process usually occur with carriers at the edge of the bands, but thermal distribution leads to broadening of the luminescence.

2. Exciton recombination. Excitons are electron-hole pairs bound to each other by their Coulomb interaction. A hydrogenic model can be used to estimate the binding energy of electron and hole and is described in Section B.3.

The processes 3 to 6 involve recombination from or to defect levels. Depending on the energy depth within the band gap of these levels, they can also lead to nonradiative recombination.

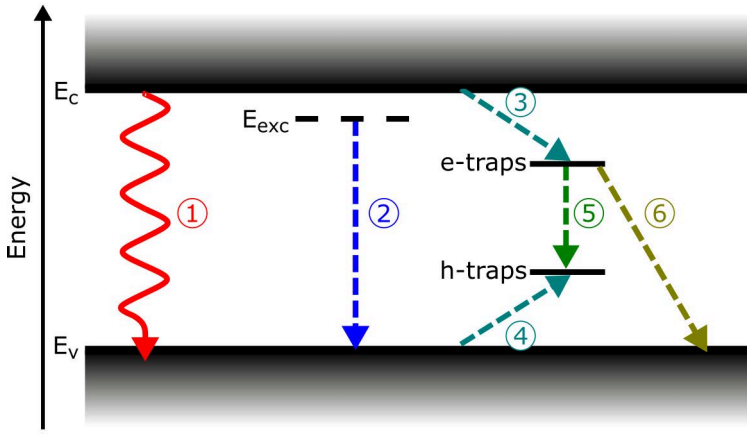

Figure 3.3: Schematic of the different transitions between the conduction (E_C) and valence (E_V) bands, the exciton (E_{exc}) and trap levels. The various recombination pathways are shown. See text for discussion.

3.2.2 Injection conditions and dominant recombination

In a PL experiment, the spontaneous emission rate can be written as [91]: $R = B(\Delta n(n_0 + p_0) + \Delta n^2)$, where Δn is the generated excess carrier density, n_0 and p_0 are the equilibrium carrier densities and B is the material-specific radiative recombination coefficient. From these equations two different conditions can be identified:

- **Low injection:** When the number of electron-hole pairs generated by the excitation is much lower than the equilibrium carrier density: $n_0 \gg \Delta n$ for an n-type material, and $p_0 \gg \Delta n$ for a p-type material. Under these conditions — and assuming a p-type material the recombination rate can be approximated as $R \approx B\Delta n p_0$ (for an n-type material replace p_0 with n_0).
- **High injection:** When the number of generated pairs is much larger than the equilibrium carrier density, $p_0 \ll \Delta n$ ($n_0 \ll \Delta n$), the radiative recombination rate can be approximated to $R \approx \Delta n^2$.

Note that under high injection conditions, the radiative lifetime (which is determines by minority carriers) is much lower than in low injection conditions. The injection conditions depend lastly on the pump fluence, i.e., the power of the excitation light. Since the radiation rate depends on the excitation power, it can be used to identify the different types of recombination in a PL experiment. A model by Vietmeyer et al. [92] describes how the different recombination paths depend on the pump fluence. Vietmeyer et al. [92] describe the solutions to the rate equations (see details of this equations in e.g., Refs [92–94]) for different pump fluences. In the sake of brevity, only the results relevant to the analysis in this thesis are described:

- Under low excitation power, carrier trapping (paths 3 and 4 in Figure 3.3), and trap-assisted, nonradiative recombination (path 5) dominate. The steady state solutions then yield $n, p \propto G$, where G is the generation rate. Since the emission intensity is proportional to the radiative rate, $I_{em} \propto k_r np$, we have that the PL intensity depends on the excitation intensity as $I_{em} \propto I_{exc}^2$.
- For higher pump fluences, monomolecular recombination through paths 2 and 6 (e.g., free and bound excitons) dominate the recombination. The solutions are then $p \propto G$ and $n \propto \sqrt{G}$, and the emission intensity behaves like $I_{em} \propto I_{exc}^{1.5}$.

In general, using the the relation:

$$I_{em} \propto I_{exc}^m \tag{3.3}$$

the type of recombination can be identified, using intensity-dependent PL measurements. By plotting the PL intensity as a function of the excitation intensity — both in logarithmic scale — the value of m can be fitted. When $1 < m < 2$, emission by recombination of localized states (e.g., donor-assisted, or exciton) is dominant. When $m \simeq 2$, trap-assisted recombination is dominant. This method has been widely used in the literature for classic semiconductor materials[95, 96], nanostructures [92], and halide perovskites[94].

3.2.3 Experimental setup for photoluminescence

A typical experimental setup for PL measurements is shown in Figure 3.4. The excitation source can be any light source with suitable wavelength range. However, the most common excitation sources are lasers, for instance gas lasers like a helium-neon laser (633 nm) or argon laser (514 nm), or solid-state laser diodes. The light is focused onto the sample by a flat mirror, a lens or parabolic mirror. Light emitted from the sample is collected by a lens or off-axis parabolic mirror, filtered to prevent unwanted higher orders and focused into a monochromator through an entrance slit (not depicted in the figure). Light exits the monochromator through an exit slit (not depicted) and hits the detector, which can be a photodiode, photomultilier tube (PMT), avalanche photodiode (APD), a two-dimensional (2D) array — such as an InGaAs or charge-coupled device (CCD) array — or a camera — e.g., complementary metal-oxide semiconductor (CMOS) or CCD. The latter allow the collection of full spectra or full images at once.

To determine the PL quantum efficiency, the setup must be calibrated to account for absolute photon numbers. The most common setup uses an integration sphere (see Kirchartz et al. [94]), but the setup used in the measurements of Chapter 5, a hyperspectral imaging setup was used. The sample is illuminated with a homogeneous, broad beam, and the luminescence recorded as a complete image, using a CCD camera. A filter — tunable band-pass liquid crystal — is used for spectral resolution.

The setup for time-resolved photoluminescence (TRPL) is similar to the one for steady state. In a typical configuration, a single photon sensitive detector (PMT or APD) is used in combination with time-measurement electronics, which measure the time passed between the pulse excitation and the first photon recorded. The measurement is repeated at a high rate (kHz-MHz), and a histogram of photon emission times is recorded, which resembles the photoluminescence decay. Typical time resolutions are ~ 50 ps. It is important to ensure that the repetition rate is well below the inverse of the longest decay time of the sample to avoid artifacts.

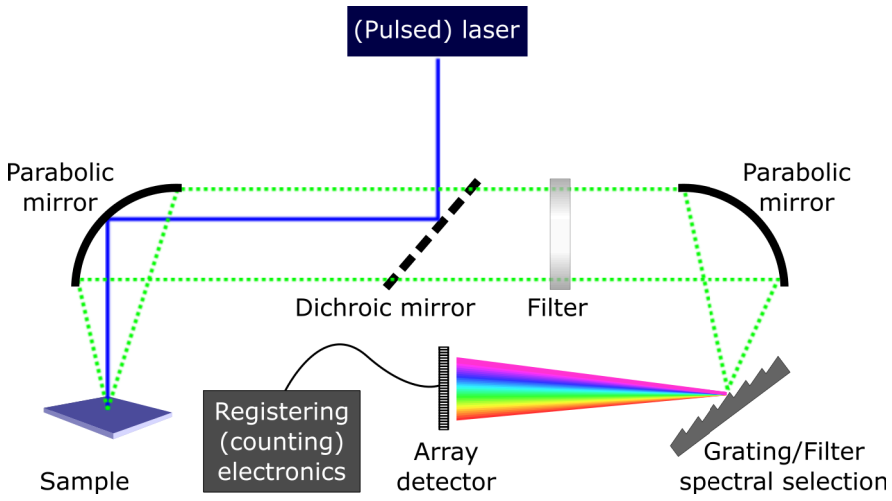

Figure 3.4: Typical experimental setup for (TR)PL measurements. The laser light is focused on the sample and the emission is then collected into the spectrograph. Time counting electronics and high-repetition pulsed lasers are used in TRPL, while array detectors are used for steady-state measurements.

3.3 Scanning electron microscopy

Most of this thesis concerns itself with microscopic properties of the Cs–Pb–Br material system, and how they correlate with a macroscopic property of the material, i.e., the luminescence. In order to do that, the composition and optoelectronic properties of the material, using high spatial resolution techniques based on the scanning electron microscope (SEM) was the focus of investigation. In this section, an overview of the physics behind the two techniques used for this purpose is given: Energy-dispersive X-ray spectroscopy (EDX, or EDS) and cathodoluminescence (CL) microscopy and spectroscopy. The interested reader is referred to the books by Goldstein et al. [97] and Yacobi and Holt [98] for in-depth descriptions of the techniques, physics and instrumentation. Here a brief description of the SEM generalities, and then the specific techniques is given.

The light diffraction limit, first introduced by Abbe in 1873 [99] limits the spatial resolution of optical microscopes. Described by $d = \lambda/(2n\sin\alpha)$, the diffraction limit is determined by the wavelength of light, λ, and the numerical aperture $n\sin\alpha$, where n is the refractive index of the medium, and α is the aperture angle of the objective lens. Maximizing $n\sin\alpha$, or minimizing λ increases the spatial resolution, which is why some commercial microscopes use high n oil as imaging medium. However, due to the relatively large wavelength of visible light, there is few room for improvement below resolution of about 250 nm.

In an SEM, a beam of high energy — and thus low wavelength — electrons is focused on the sample's surface and scanned across it. The electrons generated, or scattered by the sample are collected by a variety of detectors. The signal of the detectors is then used to generate an image of the sample's surface pixel by pixel. The interaction of the electron beam with the sample involves a variety of scattering processes. Elastic scattering — without the loss of energy — is the process by which an impinging electron deviates from it's original trajectory. This deviation increases the narrow angular range of the interaction considerably within the sample. On the other hand, electrons impinging in the sample lose energy by inelastic scattering. The lost energy is transferred to the atoms in the material of the sample, by means of interactions with the inner- and outer-shell electrons. For instance, when a beam electron ejects a weakly bound, outer-shell electron, a secondary electron is formed. By contrast, when a tightly bound, inner-shell electron is ejected, subsequent electronic transitions lead to emission of characteristic X-rays. Additionally, the deceleration of electrons in the electric field produced by the arrangement of ions (atomic nuclei screened by orbital electrons), produces X-ray emission in a continuum energy range from a couple of eV up to the beam energy, known as *Bremsstrahlung*, or "braking radiation". In a semiconductor, the impinging electrons can also excite electrons from the valence to the conduction band, generating electron-hole pairs, which can either diffuse and be extracted, generating electrical current, or recombine, emitting light. Incident electrons can also excite phonon modes, leading to heating of the samples.

Inelastic scattering is the one responsible of limiting how far does the electron beam travel inside the sample. The Gruen range of electron penetration in the material is given by [98] $R_e = (k/\rho)E_b^\alpha$, where ρ is the material density, E_b is the electron beam energy, and k and α depend on the atomic number and the beam energy. Although different approaches exist to estimate R_e, for low acceleration voltages, the one proposed by Everhart and Hoff [100] is

commonly used:

$$R_e = (0.0398/\rho)E_b^{1.75}[\mu m] \tag{3.4}$$

where ρ is given in g/cm^3, and E_b is given in keV.

The interaction of the electron beam leads to a variety of physical phenomena, and output signals, many of which can be measured in order to extract not only morphological, but also compositional, crystallographic, optoelectronic, and electrical information from the sample under study.

3.3.1 Electron imaging and electron detectors

When imaging in an SEM, two main types of electrons emitted from the sample are used: secondary electrons (SE) and backscattered electrons (BSE). They can be identified by their energies. While SE electrons exhibit rather small energies — between a few to 50 eV — BSEs cover the higher energy range, from about 50 eV up to the energy of the primary beam [97, 101].

This difference between SEs and BSEs make them sensitive to different material properties, such as topography, surface potential, atomic number, crystallographic orientation, among others. In the following some of these properties and the detectors used to image them are described.

3.3.1.1 Secondary-electron detection

As stated above, SE electrons are generated by means of inelastic scattering, when primary beam electrons eject outer shell electrons. They exhibit low kinetic energy and a sharp energy distribution that depends on the material. However, it is considered that no secondary electron is produced for kinetic energies above 50 eV.

SEs are produced along the complete path of the incident electron until it completely loses energy and is absorbed by the material. However, due to the low energy of SEs, they rapidly lose energy while traveling through the material and only a fraction of them reach the surface with enough kinetic energy to escape the material. This implies that only SEs generated very close to the surface (a couple of nm) can escape and be detected. This is the reason why SE detectors are used to image the topography and surface of the material. Additionally, potentials on the surface — either sample surface potential, bias- or doping-induced — can affect the imaging, since a positive potential on the surface will retard the ejected SE, while a negative potential will repel it. Negatively charged regions will then appear brighter than positively charged ones. Voltage contrast, doping, or surface potential contrast can be then obtained from SE detectors [102]. Two types of SE detectors were used in the experiments described in this thesis: Everharth-Thornley detector and in-column, or in-lens detector.

- **Everhart-Thornley detector:** In this type of detector, the low-energy SEs are accelerated away from the microscope column, towards a scintillator coated with a thin metal film positively-biased ($\sim$ 10 kV) in front of a photomultiplier. To prevent deflection of the primary beam, the scintillator is surrounded by a Faraday cage with a positive bias (much lower than that of the film on the scintillator). The design of

the detector does not avoid the collection of BSEs. The mixed BSE and SE complex information, creates an apparent "illumination" of the SE image [97].

- **In-lens detector:** The magnetic field of the objective lens in an SEM also projects into the specimen chamber. SEs and BSEs electrons can be captured by the magnetic field and spiral through the lens. However, due to their different energies, their trajectories are also different. Thus, they can be detected by different detectors inside the SEM column, allowing efficient separation of BSE and SE electrons. Therefore, in-lens detectors are much more sensitive to the sample surface (topography and potential).

3.3.1.2 Backscattered electron detection

A significant part of the electrons in the impinging primary beam, can undergo a series of scattering events that reverse their direction of travel, returning towards the surface and exiting the sample. These electrons are the backscattered electrons, BSE. They carry important information and are one of the main signals in SEM imaging.

The scattering cross-section model proposed by Rutherford [103] can be used to represent the multiple elastic scattering, responsible of the trajectory deviations giving rise to the narrow angle (or Rutherford) BSEs. Within this model, the scattering cross-section is proportional to the squared of atomic number of the material, i.e. $\sigma \propto Z^2$. The relativistic corrections the model includes can be ignored for $E_b < 50\,\text{keV}$, and the Rutherford model is accurate for beam energies between 20 and 50 keV[98]. This implies that Rutherford electrons are scattered as $\propto Z^2$, which makes them a useful tool for Z-contrast imaging [97, 98, 101].

By contrast, for lower E_b, and high Z, the more complex Mott scattering model must be used, which will not be discussed here. It is sufficient to state that this model is appropriate for single elastically scattered BSEs. This electrons "bounce" back from the surface at very large angles. They are however more sensitive to the crystal orientation of the surface, and can be used for so-called channeling-contrast imaging, as shown in Figure 3.5 [101]. Different detectors can be used for each of these types of BSEs. In the following the energy-selective, in-column detector (EsB) and the angle-dispersive (AsB) detector are briefly described.

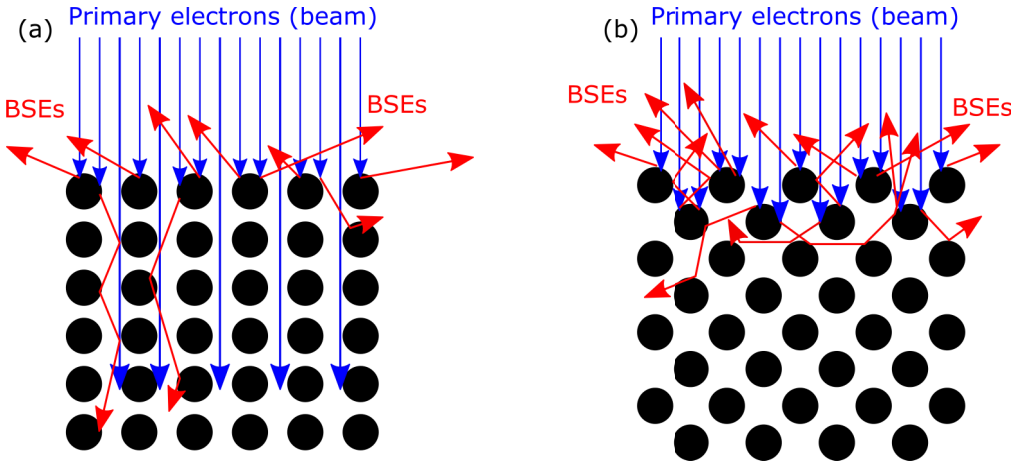

Figure 3.5: Schematic representation of the channeling contrast mechanism. Mott-type BSEs are less efficiently scattered by a crystal aligned to the primary electron beam and the region appears darker (a). In the case that the crystal is not aligned to the beam, BSEs are mmore effitiently scattered and the region appears brighter (b).

- **EsB detector:** This detector is positioned in the column, similarly to the SE in-lens detector. However it is located above the in-lens detector and it is selective for Rutherford-type BSEs.

- **AsB detector:** This detector is positioned just beneath the end of the pole piece. it is capable of detecting Mott-type BSEs scattered at large angles ($> 60°$), thus identifying them from the Rutherford-type ones [104]. This detector offers crystallographic, or channeling contrast, as already explained (see Figure 3.5).

3.3.2 Energy-dispersive X-ray spectroscopy

As already stated in section 3.3, inelastic scattering of beam electrons can lead to the ejection of an inner-shell electron in an atom of the sample. This leaves the atom in a higher energy state that can be relaxed by filling the gap in the inner-shell by an electron from an elevated state. This process produces the emission of a photon with energy equal to the difference in the ionization energies for electrons in the involved shells. This energy difference is characteristic of each specific element, and measuring it gives us information about the chemical composition of the sample (see figure 3.6).

One of the ways with which the characteristic X-rays from the sample can be detected is by means of the charge pulses generated on a semiconductor detector. The Silicon drift detector, is based on the absorption of the X-ray quantum by an inner-shell atom of the Si, generating a photoelectron. This is then scattered inelastically inside the Si crystal, generating electron-hole pairs, which under an applied potential can drift towards the electrodes and generate a measurable charge pulse. The number of generated charges is proportional to the energy of the incident X-ray photon, thus, the detector can respond to any photon energy within given limits (typically from 50 eV to 30 keV) the process has been named "energy-dispersive", although no actual photon dispersion occurs [97]. An X-ray spectrum can then be reconstructed by assigning the pulse information to specific energy slots. This is the principle for energy-dispersive X-ray spectroscopy (EDX).

Based on this principle, compositional analysis based on single spectrum, or elemental maps, can be acquired, by scanning the electron beam several times over the sample in order to collect good statistically significant data (rule of thumb, 10 000 counts per X-ray line). The spatial resolution of EDX measurements is determined by two important factors: (1) the electron beam acceleration voltage, which — as described by Equation 3.4 — determines the penetration depth and interaction volume of the beam with the sample. This will determine how big is the excitation volume, from which the measured X-rays stem; and (2) the mean free path of the X-ray photon selected for analysis. Photons with lower energies have shorter mean free paths and can be scattered or reabsorbed inside the sample. This implies that the photons measured at these lower energies are originated closer to the surface, in a smaller excitation volume, thus improving the spatial resolution.

3.3.3 Cathodoluminescence mapping and spectroscopy

As mentioned in Section 3.3, the impinging electrons in an SEM can generate electron-hole pairs, which can recombine in similar manners as those described in Section 3.2.1.

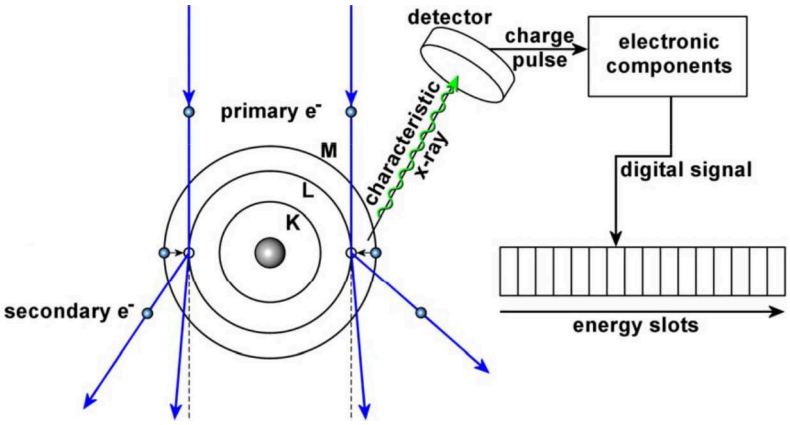

Figure 3.6: Schematic of the working principle of EDX in an SEM. Note that no actual photon dispersion occurs, rather an energy slot assignment according to counted charge pulses. Figure adapted from Abou-Ras, Kirchartz, and Rau [101].

Measuring the emitted light can give us similar information to that in PL spectroscopy, with the added advantage of a high spatial resolution of the SEM. Cathodoluminescence (CL) is the microscopy/spectroscopy technique used for this purpose.

3.3.3.1 Details of emission in CL

Although CL and PL are fairly similar techniques, exciting the sample with the electron beam implicates some crucial differences in the generated radiative transitions, which are worth discussing, in order to properly interpret CL results. First, exciting the sample with a high-energy electron beam results in much higher generation rates and injection condition (see section 3.2.2) than in PL. While a photon with energy higher than the band gap is expected to generate one electron-hole pair, each impinging electron can generate between 10^2 to 10^3 electron-hole pairs [91]. The generation rate of electron-hole pairs per second and unit volume can be estimated using an empirical model that takes into account the electron beam parameters and the composition of the material (see details in Appendix A) [91, 98, 105, 106]:

$$G = \frac{E_b I_b}{e(2.1E_g + 1.3)}(1-\eta)\left[\frac{4}{3}\pi\left(\frac{R_e}{2}\right)^3\right]^{-1} \tag{3.5}$$

where E_b is the primary beam energy, I_b the beam current, E_g the material band gap, e the electron charge, η the backscattering coefficient, which depends on the composition of the material (see Appendix A, Equation A.3), and R_e the Gruen penetration depth, as per Equation 3.4.

This relation is important for halide perovskite materials, owing their relatively low carrier density. The work presented here on $CsPbBr_3$ — and other work carried out on mixed-cation, mixed-halide materials [107] — has shown that the generation rate at beam conditions limit to the setup used, can go as high as 10^{24}–$10^{26}\,cm^{-3}\,s^{-1}$, which some orders of magnitude higher than low injection conditions in PL ($\sim 10^{21}\,cm^{-3}\,s^{-1}$ [85]). Therefore, the measurements reported here are dominated by bimolecular recombination, exhibit very short lifetimes and should be considered as excitation maps, rather than as emission maps i.e., the measured CL emission stems from the area excited by the electron beam.

Finally, CL resolution depends on the beam energy and the excitation volume, and on the carrier diffusion length inside the material [108]. However, injection conditions can influence the spatial resolution as well. The reduced lifetime and diffusion length at high injection can improve the effective spatial resolution at the expense of not being able to capture other types of recombination. This is specially useful when trying to identify emitting domains or phases inside the material, as reported in the present thesis and related published works [107, 109].

3.3.3.2 CL modes and experimental setup

A typical CL setup is shown in Figure 3.7. Typically, a parabolic mirror is positioned above the sample. A hole in the mirror allows the electron beam to excite the surface of the sample. The mirror focuses the light emitted from the sample through quartz window into an optical system outside the SEM chamber. From this point, the system resembles the optical path described for a PL system: Lenses focus the light through a set of filters (for monochromatic maps, no filter for panchromatic maps) into a PMT, or through an input slit to a monochromator, which disperses the light onto an array detector (InGaAs array, CCD or CMOS camera) for hyperspectral mapping.

Depending on the configuration, intensity maps, either monochromatic or panchromatic, can be measured. This type of measurements is quick, and allow to reduce the intensity of the interaction of the beam, and avoid beam-induced damage. It is specially useful for phase identification, and the study of the luminescence in relation to the microstructure, composition or other properties [101][109][107][110]. A spectrum can be also collected pixel-by-pixel, acquiring hyperspectral maps. These are specially useful for studying the different types of recombination, peak positions, peak shifts etc. with high spatial resolution.

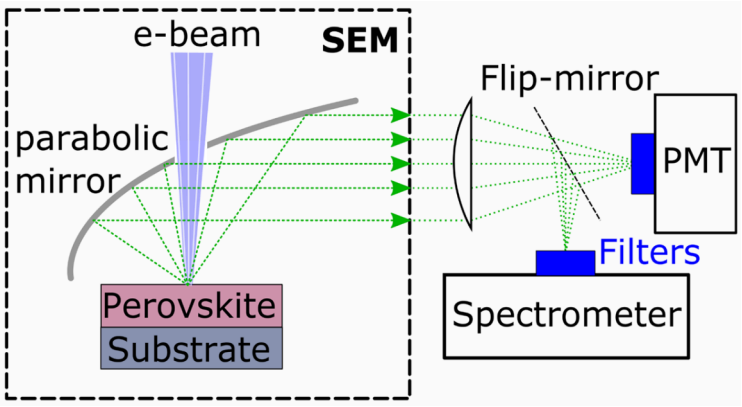

Figure 3.7: Typical CL setup in an SEM. A parabolic mirror colects and focuses the light emitted from the sample into an optical system outside the SEM chamber. Both intensity maps (PMT) and hyperspectral maps (spectrometer) are possible.

3.4 Theoretical considerations

As described in Section 2.2, Cs–Pb–Br materials can form composites with $CsPbBr_3$ embedded in either Cs_4PbBr_6 or $CsPb_2Br_5$. The quantum confinement of $CsPbBr_3$ nanocrystals partially explains the enhanced luminescence, but other phenomena, such as the emission energy and other possible mechanisms for the enhancement of the PLQY remain unexplained.

Since one of the aims of the present thesis is to model the effects that dielectric effects can have in the luminescence of Cs–Pb–Br composites, this section overviews the most important theoretical aspects and limitations of the models described in Section 6.4.

3.4.1 The Brus approximation to exciton emission

Brus [111] generalized the expression for excitons in the effective mass approximation (EMA) and envelope function approximation (EFA) (see Appendix B.3, Equation B.11) to include the confinement effects and electron-hole correlation in a simplified form for the exciton emission energy:

$$E_{em} \simeq E_g + \frac{h^2}{8\mu^* r^2} - \frac{\mu^* e^4}{8\varepsilon^2 \varepsilon_0^2 h^2} \tag{3.6}$$

where only the first bound state is considered.

Another important result of the effective mass approximation in confined systems, and of the Wannier-Mott exciton model is the exciton Bohr radius:

$$a_B = \frac{\hbar^2 \varepsilon}{\mu^* e^2} \tag{3.7}$$

The size of the nanocrystal, relative to a_B determines the confinement regime: *strong confinement* when the size of the nanocrystal is much smaller than a_B, and the motion of both electron and hole are quantized, and the *weak confinement*, when the size of the nanocrystal is larger than a_B and the confinement effects do not interfere with the relative motion of electron and hole, leading to the quantization of the center of mass only. An *intermediate confinement* regime can be defined when the size of the nanocrystal is comparable to a_B in semiconductors with very different electron and hole effective masses. Thus, the effect of quantum confinement in each particle is different. The electronic structure and approximations for these different regimes are described in detail by Efros and Rosen [112] and in the book by Bányai and Koch [113].

3.4.2 Many-particle systems

A more exact description of the exciton can be done by solving the many particle system that includes the electron, hole and their correlation explicitly in the Hamiltonian, instead of an approximation from their relative position, as the Hamiltonian in Equation B.7b. To this end, the Hamiltonian and wave equation of the electron-hole system can be expressed as:

$$H(\mathbf{r}_e, \mathbf{r}_h) = -\nabla_e \frac{\hbar^2}{2m_e^*} \nabla_e - \nabla_h \frac{\hbar^2}{2m_h^*} \nabla_h + V^{(e)}(\mathbf{r}_e) + V^{(h)}(\mathbf{r}_h) + V_c(\mathbf{r}_e, \mathbf{r}_h) \tag{3.8a}$$

$$H(\mathbf{r}_e, \mathbf{r}_h)\Psi(\mathbf{r}_e, \mathbf{r}_h) = E_{exc}\Psi(\mathbf{r}_e, \mathbf{r}_h) \tag{3.8b}$$

where the first two terms in Equation 3.8a are the kinetic operators of the electron and hole, $\mathbf{r}_{e/h}$ is the electron (hole) position, $\Psi(\mathbf{r}_e, \mathbf{r}_h)$ is the two-particle wavefunction, and the potentials $V^{(e/h)}$ include not only the confinement potential, but other single particle interactions that

will be described in Section 3.4.3. Finally the last term include the Coulomb interaction between electron and hole, which usually contains a term of the form $1/|\,\mathbf{r}_e - \mathbf{r}_h\,|$ (as in Equation B.6), but in a more complete sense, should also include the effect of the mismatch of the dielectric constant of the nanocrystal and its surrounding medium.

The details of how Equation 3.8b is solved can be found in Section 6.4.2 and references therein. Here it is more important to define the exciton energy and exciton binding energy. If the top of the valence band is taken as reference, the total energy of the exciton in, e.g. the bulk crystal is simply the sum of the energies of the free electron and hole, i.e. the electronic band gap, minus the Coulomb attraction. This can be approximated as in Equation B.10, where the second term was defined as the exciton binding energy. However, in the confined nanocrystal, quantum confinement shifts the single particle states from their positions at the band edges, as shown in Figure 3.8. Therefore, the exciton energy is defined as:

$$E_{exc} = E_g + E_e + E_h - E_{eh} = \langle \Psi | H(\mathbf{r}_e, \mathbf{r}_h) | \Psi \rangle \tag{3.9}$$

where E_e and E_h are the electron and hole single-particle energies, and E_{eh} is the two-particle interaction energy. The exciton energy can be obtained as the expectation value of the energy of Equation 3.8b.

The exciton binding energy for the two-particle system can be defined by:

$$E_b = E_{e1} + E_{h1} - E_{exc} \tag{3.10}$$

where E_{e1} and E_{h1} are the eigenvalues of the lowest single-particle bound states — i.e. the confinement energies, not to be confused with $E_{e,h}$ which include self-interaction corrections.

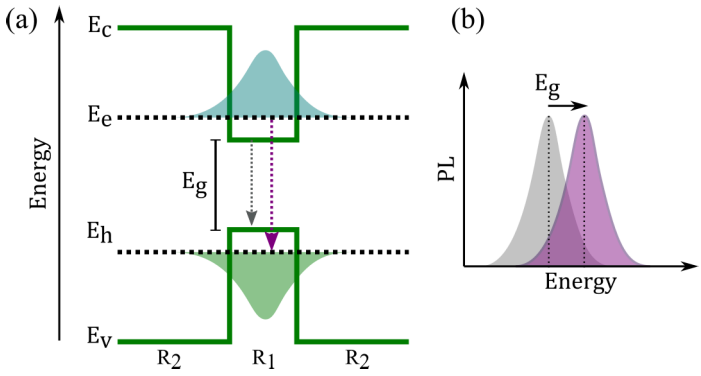

Figure 3.8: (a) Band diagram schematic showing the shifts of the electron and hole energies as a result of quantum confinement in region R_1 embedded in R_2 with larger band gap. (b) Schematic of the PL spectra showing the shift in the emission energy, as a result of the confinement.

3.4.3 Dielectric confinement

When the nanocrystal is embedded in a matrix material, as it is necessary to be useful in many technnological applications, and as it is the case in Cs–Pb–Br systems, and such matrix material has a smaller dielectric constant, the dielectric mismatch between the nanocrystal and the environment is responsible for the dielectric confinement effect. Dielectric confinement was first described by Keldysh [114] and then confirmed experimentally [115, 116] and it can influence the exciton binding energy, as well as the optical properties of confined semiconductors

In the context of classical electrodynamics, a charge near to a dielectric interface induce the appearance of polarization charges at said interface [117, 118]. Depending on the relative magnitude of the dielectric constants, the induced charges can have the same sign as the original charge, if the dielectric constant of the material hosting the carrier (ε_1) is larger than that of the adjacent material (ε_2). This constitutes the phenomenon of dielectric confinement. In contrast, if the dielectric constant of the host material is smaller than that of the adjacent material ($\varepsilon_1 < \varepsilon_2$), the induced charges have the opposite sign. This phenomenon is illustrated in Figure 3.9.

The charges induced at the interface generate two new contributions to the energy of carriers, that must be taken into account in the Hamiltonian (Equation 3.8a): *the self-polarization interaction*, which is a single-particle contribution that arises from the interaction of the source charge with its own induced charges, and the *polarization of the Coulomb interaction*, which is a many-particle contribution that arises from the interaction of a carrier with the charges induced by the other. The details of how these interactions are described in the Hamiltonian and considered in the model are given in Section 6.4.2.

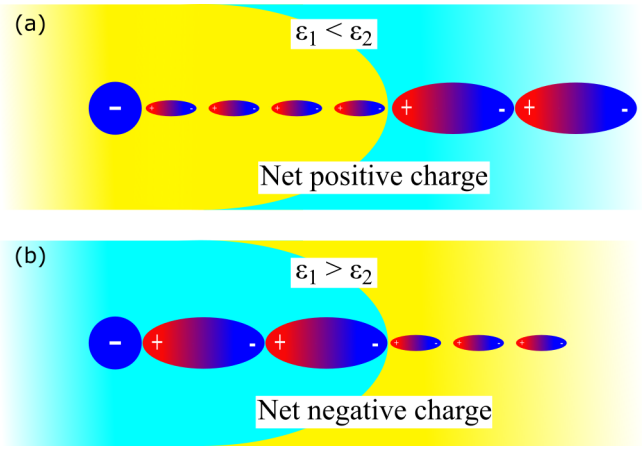

Figure 3.9: Schematic showing how a negative charge embedded in a dielectric medium with relative dielectric constant ε_1 induces a polarization charge when it is near an dielectric interface with a material with dielectric constant ε_2. (a) When $\varepsilon_1 < \varepsilon_2$ the net charge induced at the interface is positive (in general, it has the opposite site), but (b) when $\varepsilon_1 > \varepsilon_2$, the net charge induced at the interface has the same sign as the source charge. The ovals represent the polarization of the dielectric and their size represent the polarizability of the material.

4

Spatial phase distribution in Cs-Pb-Br thin films

In this Chapter the results of investigation of the phase distribution of Cs–Pb–Br thin films deposited on a glass substrate using different common deposition techniques are presented. First, density functional theory (DFT) is used to calculate the formation enthalpies of the different phases, showing that the different ternary phases can coexist, owing to their close formation energies. The question of how one phase can transform into another and how this can affect the material properties is formulated. Then, a set of experiments — and results thereof — used to deposit and investigate the structural and optical properties (at a macroscopic level) of Cs–Pb–Br thin films are described. Finally, a correlative microscopy characterization approach was used to investigate the spatial phase distribution in said thin films, based on their optoelectronic properties and composition, using cathodoluminescence (CL) and energy-dispersive X-ray spectroscopy (EDX) experiments.

4.1 Formation enthalpies and phase coexistence in Cs-Pb-Br system

Ab-initio calculation of formation enthalpies in Cs–Pb–Br

Using the crystal structures described in Section 2.2 as a starting point, Ayala Cohen, from the Weizmann Institute of Science (WIS), Israel, calculated the formation enthalpies of the

different phases. These are computed simply by subtracting the energies per formula unit (E_{tot}) of reactants from that of the products:

$$\Delta H = \sum E_{tot}(products) - \sum E_{tot}(reactants) \tag{4.1}$$

It is important to note that for the perovskite phase, only the formation enthalpy of the room-temperature, orthorhombic structure was calculated, since it is the one relevant to compare with the experimental results. Now, considering the formation of the different phases from the elements that compose them, the formation enthalpies summarized in Table 4.1 are obtained. The large negative values indicate that all the three phases, as products of the reaction of the composing elements, are enthalpically stable.

Table 4.1: Formation enthalpies per formula unit of the Cs–Pb–Br ternanry phases from the reaction of the composing elements

Reaction	Formation enthalpy ΔH (eV)
$Cs + Pb + 3\,Br \longrightarrow CsPbBr_3$	-3.92
$Cs + 2\,Pb + 5\,Br \longrightarrow CsPb_2Br_5$	-7.08
$4\,Cs + Pb + 6\,Br \longrightarrow Cs_4PbBr_6$	-5.91

However, these reaction do not reflect the experimental synthesis properly. The materials in the Cs–Pb–Br system are synthesized from binary precursors CsBr and $PbBr_2$. Table 4.2 summarizes the formation enthalpies calculated for the reaction of the binary precursors. Note that the formation enthalpies decrease for all of the phases (a simple consequence of the stability of the binary precursors), but they preserve the negative sign, meaning that the ternary phases formed from the binary precursors are enthalpically stable as well. This result can be compared with the formation enthalpy calculated for the hybrid halide Perovskite (HaP) $CH_3NH_3PbI_3$ (MAPbI for breivity). For the reaction $MAI + PbI_2 \longrightarrow MAPbI_3$ the formation enthalpy is only $-0.02\,eV$ — value provided by Ayala Cohen, WIS (unpublished data). This value suggests that this HaP is only marginally stable, as reported in the literature [119, 120], and agrees with experimental data which shows that $MAPbI_3$ exhibits serious stability issues [10, 119].

Table 4.2: Formation enthalpies per formula unit of the Cs–Pb–Br ternanry phases from the reaction of binary precursors

Reaction	Formation enthalpy ΔH (eV)
$CsBr + PbBr_2 \longrightarrow CsPbBr_3$	-0.24
$CsBr + 2\,PbBr_2 \longrightarrow CsPb_2Br_5$	-0.31
$4\,CsBr + PbBr_2 \longrightarrow Cs_4PbBr_6$	-0.51

An interesting result of these calculations is how the formation enthalpies of the different ternary phases compare with each other. From the values in Table 4.2, a straightforward conclusion is that Cs_4PbBr_6 is the most stable of all the ternary phases, followed by the $CsPb_2Br_5$. The perovskite follows the $CsPb_2Br_5$ closely ($\sim$50 meV difference). The implications of the similar formation enthalpies of the $CsPbBr_3$ and $CsPb_2Br_5$ phases are discussed in more detail in Chapter 5.

It is worth noting that the formation enthalpies obtained from DFT calculations cannot be regarded as exact. They depend on the use of pseudopotentials which replace the charge

density of the core electrons for a smooth density. The different nature of the reactants and the use of the same pseudopotential for all the compounds in the reaction increases the error. However, this approach offers a coarse semiquantitative estimation of the formation enthalpies and the stability of the different phases. The results presented here are in good agreement with those published by Yin et al. [68], — who used a higher level of theory — which supports the validity of our approach.

The calculation of the enthalpies, as described above, were performed using the Vienna Ab-initio Simulation Package (VASP) [121]. using the Perdew-Burke-Ernzerhof (PBE) form of the generalized gradient approximation to describe the exchange-correlation interactions [122]. Dispersion interactions were included within the Tkatchenko-Scheffler scheme[123] using an iterative Hirshfeld partitioning of the charge-density [124, 125]. Core electrons are described by the projector augmented waves method[126, 127]. For the ternary phases, $PbBr_2$ and CsPbr, plain wave basis sets with cutoff energies of 600, 800 and 300 eV were used. The k-space integration was performed on a $3 \times 3 \times 3$ grid for Cs_4PbBr_6, a $4 \times 4 \times 4$ grid for $CsPb_2Br_5$, a $5 \times 5 \times 5$ grid for $CsPbBr_3$ and CsBr, and a $6 \times 7 \times 6$ grid for $PbBr_2$. Relaxation of the ternary phases was performed using the GADGET optimizer[128] until all forces acting on the atoms were below 0.01 eV/Å. The energy convergence criterion for each ionic step was set to 10^{-6} eV.

The theoretical results described above confirm that the ternary phases of the Cs–Pb–Br material system can coexist, as it has been shown in experimental reports for single crystals [19, 49], powders [25, 129], nanocrystals [20, 22, 24, 26] and thin films [23, 24, 109, 110]. The latter form is the most attractive form of $CsPbBr_3$ for applications in optoelectronic devices such as solar cells[12, 38–42], light emitting diodes (LEDs)[13–15], lasers[16] and photodetectors[35–37]. Since the phase coexistence can affect the optical and electrical properties of the material — and by extension the performance of devices — in the remainder of the present Chapter the phase coexistence and spatial distribution in Cs–Pb–Br thin films deposited by different methods are investigated experimentally.

4.2 Thin film deposition and macroscopic characterization

In order study the coexistence and distribution of phases, Cs–Pb–Br thin films were characterized by means of photoluminescence (PL) and UV-vis spectroscopies, and X-ray diffraction (XRD). The films were provided by Dr. Robert Lovrinčić, Dr. Christian Müller and Dr. Michael Sendner from the InnovationLab GmbH and Heidelberg University. Details of the synthesis are provided in the following subsection. A reference $CsPbBr_3$ powder sample, used as structural reference, was synthesized in house by Dr. Frederike Lehmann.

4.2.1 Sample preparation

4.2.1.1 Synthesis of the thin films

The Cs–Pb–Br thin films were deposited on a glass substrate using three different synthesis methods, commonly used to deposit HaP-based materials and devices [5]: Two solution-processed methods e.g., single- and two-step spin coating, and a physical deposition method i.e., coevaporation of CsBr and $PbBr_2$, as shown in Figure 4.1.

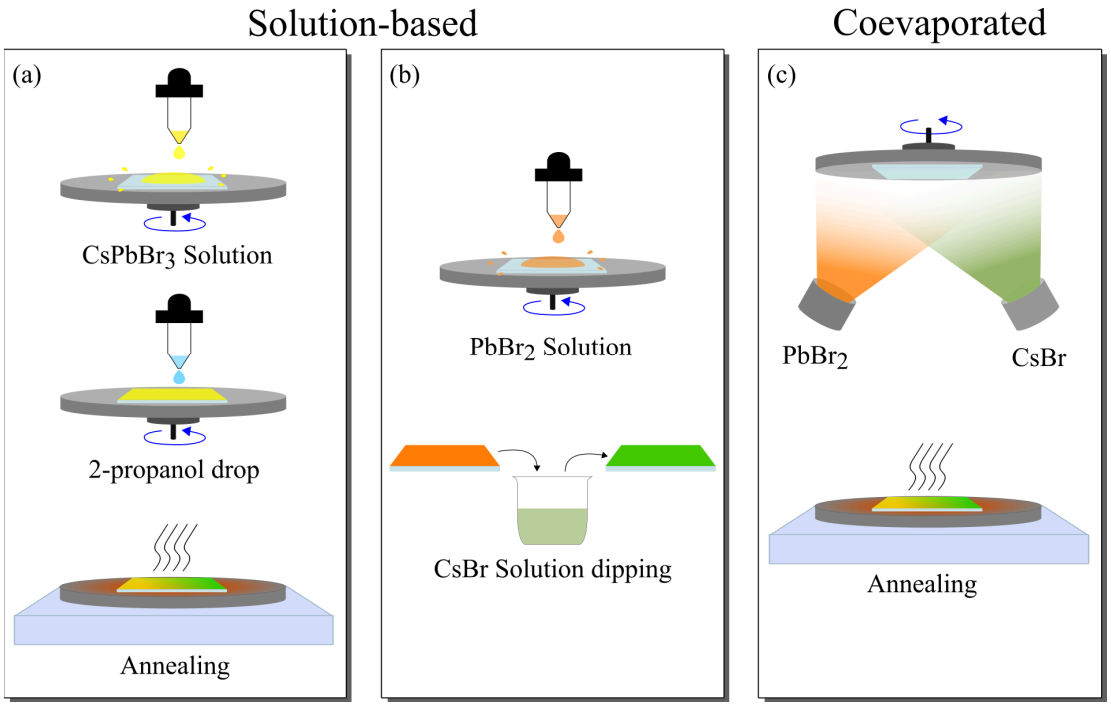

Figure 4.1: Schematics of the different methods used to deposit the thin films studied in this Chapter. Two solution-based methods: (a) single- and (b) two-step spin-coating, and (c) a physical vapor coevaporation method.

1. ***Single-step spin-coated film* (SC1).** A 0.8 M solution of 1:1 $PbBr_2$ and CsBr in dymethyl sulfoxide was spin-coated on a glass substrate, preheated at 75 °C. During the third spin step, 2-propanol was dropped on the spinning substrate. The resulting film was dried on a hot plate at 70 °C for 15 min.

2. ***Two-step spin-coated film* (SC2).** A 1.0 M solution of $PbBr_2$ in dimethylformamide (DMF) was spin-coated on a glass substrate, preheated at 75 °C. The resulting $PbBr_2$ film was dipped in a solution of CsBr in methanol. The procedure is based on the one reported by Kulbak, Cahen, and Hodes [11].
   Both the processing of SC1 and SC2 were carried out in inert (N_2) atmosphere.

3. ***Coevaporated film* (CE1).** $PbBr_2$ and CsBr were thermally coevaporated onto a glass substrate in a high-vacuum chamber with a base pressure in the order of 10^{-7} mbar. The deposition rates were monitored using two calibrated quartz microbalances. The film was then annealed at 100 °C in an inert (N_2) atmosphere for 15 min. A similar sample (CE2) was simultaneously deposited on a Si substrate. This sample was used for APT analysis and phase transformation studies as described in Chapter 5.
   It was inevitable to have an excess of $PbBr_2$ towards the end of the coevaporation process, which influenced the secondary phase obtained with this deposition technique.

4.2.1.2 Synthesis of the powder sample

The $CsPbBr_3$ powder was obtained from an equimolar solution of CsBr and $PbBr_2$ in DMF. The solution was stirred overnight at 60 °C and then the solvent was evaporated at 85 °C, followed by annealing at 140 °C for 1 h. The powder, as well as the films were synthesized

and stored in an inert (N_2) atmosphere to avoid potential degradation due to exposure to the environment.

4.2.2 Macroscopic characterization

4.2.2.1 Phase identification using XRD

As a first characterization step, all the phases present in the films were identified using XRD. The diffractograms in Figure 4.2 were acquired in a PANalytical X'Pert MPD Pro X-Ray diffractometer in Bragg-Brentano (θ–2θ) configuration. A Cu cathode was used as radiation source (Cu $K\alpha$ radiation $\lambda = 0.154\,\text{nm}$) and the 2θ angle was measured between 10° and 70°. Special thanks are due to René Gunder for the XRD measurements.

All of the diffractograms exhibit peaks that can be assigned to the orthorhombic, *Pbnm* phase of $CsPbBr_3$ [130]. However, additional peaks that can be indexed to additional phases were detected; SC1 contains trigonal, $R\bar{3}c$ Cs_4PbBr_6 [50], SC2 contains the tetragonal, $I4/mcm$ $CsPb_2Br_5$ [57] and the cubic, $Pm\bar{3}m$ CsBr [131, 132], and CE1 contains $CsPb_2Br_5$.

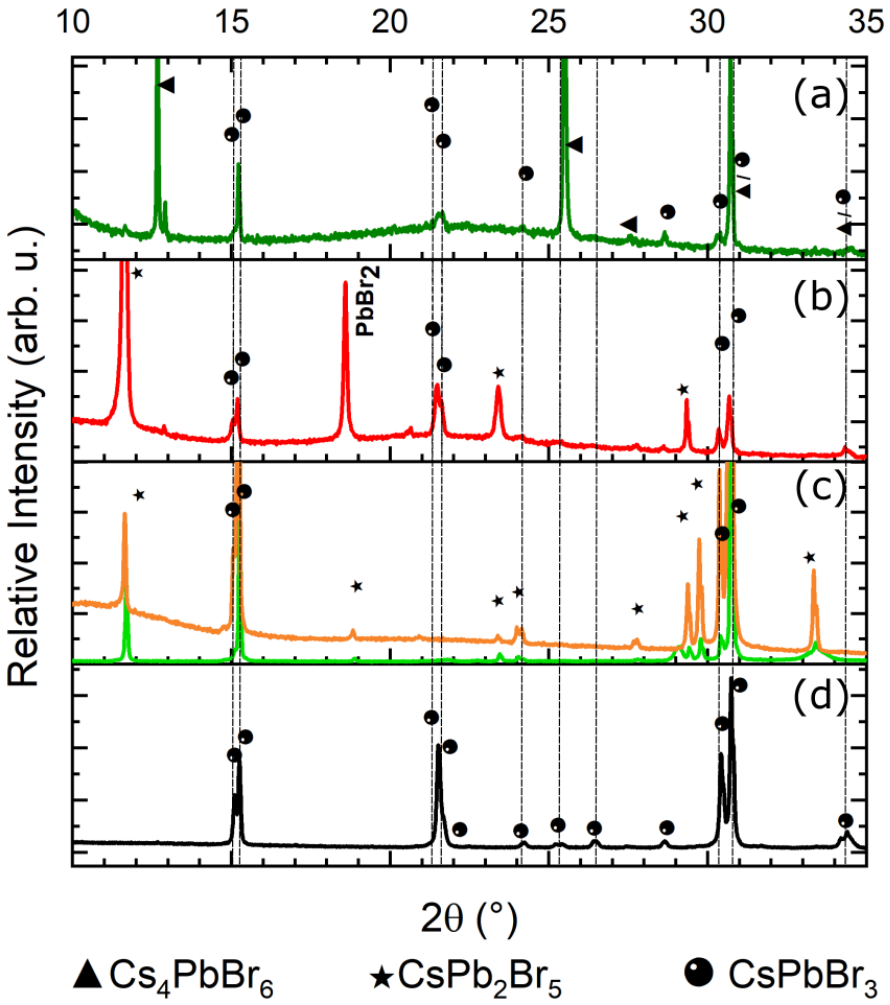

Figure 4.2: X-ray diffractograms of the (a) single- and (b) two-step solution-processed films (SC1 and SC2), the (c) coevaporated film on glass (CE1, orange) and on Si (CE2, red), and (d) reference $CsPbBr_3$ powder. The patterns were indexed according to: Cs_4PbBr_6 PDF 01-077-8224 [50], $CsPbBr_3$ PDF 01-072-7929 [130] and $CsPb_2Br_5$ PDF 00-025-0211 [57]. Adapted from Caicedo-Dávila et al. [109].

When the diffractograms of the thin films (Figues 4.2a to c) were compared with the one of the $CsPbBr_3$ powder it was found that the peak around $2\theta = (21.55 \pm 0.09)°$, characteristic of a lattice spacing of 0.41 nm is not present in the pattern of the CE films and it is shallow in those of the SC1 and SC2 films. Similar diffractograms were reported in the literature[133] and they are characteristic of textured films, i.e. films with a preferential orientation. The XRD results suggest that coevaporated films exhibit much stronger $\langle 110 \rangle$ texture of the $CsPbBr_3$ phase than the solution-processed ones.

4.2.2.2 Optical characterization with PL and UV-vis

After having identified the phases by means of XRD, the optoelectronic properties of the films were investigated with aim of identifying possible differences among them. Emission was measured by means of photoluminescence (PL) spectroscopy, and absorption by means ultraviolet–visible (UV-vis) spectroscopy in transmission mode. The PL spectra in Figure 4.3 were measured using a CCD detector coupled to a 1/2 m grating monochromator. The films were excited with a 409 nm diode laser with a spot radius of ∼100 µm and an excitation density in the range from 0.3 to 0.9 W/cm^2. Light in the spectral range from 1.7 to 2.8 eV was detected with a resolution of 0.002 eV. Special thanks are due to Dr. Sergei Levcenco for performing the PL measurements.

The absorption spectra in Figure 4.3 were estimated as $a = 1 - T$, being T the measured transmission (therefore, CE2 cannot be measured). The latter was acquired using a LAMBDA 950 UV-vis spectrometer from Perkin Elmer, equiped with a halogen lamp, a prism monochromator and a Peltier-controlled photomultiplier tube (PMT). The spectral resolution of the measurement was set to 2 nm (∼ 0.13 eV), in the range from 300 to 700 nm. However, due to problems in the instrument, the transmission below 380 nm (∼ 3.3 eV) could not be measured accurately. Since the transmission spectra was measured, and reflection was not taken into account, a quantitative analysis of the absorption, nor obtain an accurate value for the optical band gap are possible. Nevertheless, these measurements are enough for the purpose of comparing the optical properties of the films deposited by different methods.

From the PL spectra only one emission peak (in the probed visible spectral range) was detected at ∼2.35 eV. This transition can be assigned to the free exciton recombination in

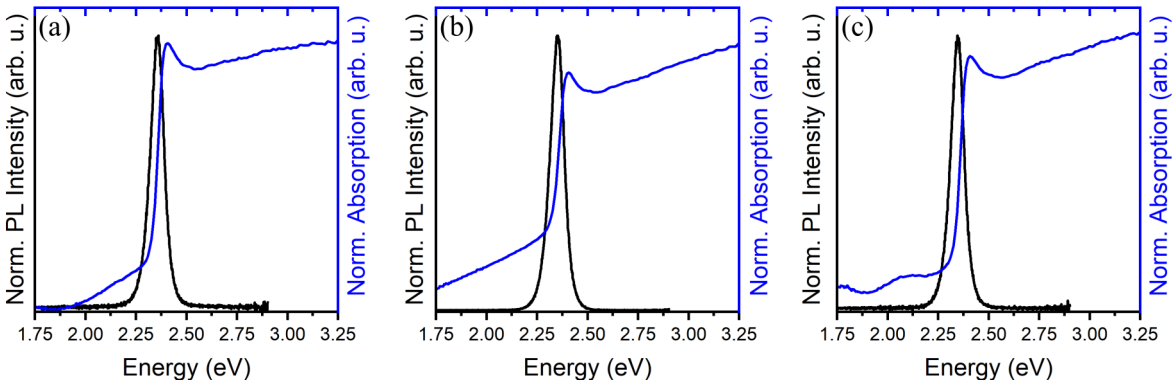

Figure 4.3: Absorption and normalized PL Spectra of the Cs–Pb–Br films on glass substrate: (a) single- and (b) two-step solution-processed films (SC1 and SC2), and (c) coevaporated film (CE1). Absorption and emission dominated by the $CsPbBr_3$ phase, present in all the synthesized films.

bulk$CsPbBr_3$ [5, 11, 29, 38]. All the films exhibit a Stokes shift of ~ 57 meV and a full width at half maximum (FWHM) of ~ 80 meV (18 nm), consistent with values reported in the literature [30, 69, 129, 134, 135] Since the secondary phases detected by XRD have been reported to have large band-gap energies [19, 30, 52–55], it is reasonable to assume that the 409 nm laser cannot excite these other phases, rendering them invisible in the PL experiments. The absorption spectra also exhibit a characteristic exciton peak, similar to experiments reported in the literature at room temperature [136], but no absorption edge for the secondary phases is detected.

4.3 Microscopic characterization and phase distribution

After identifying the phases in the films and measuring their optical properties in the visible spectrum, the microscopic phase distribution was investigated using a correlative microscopy approach. Additional to the topography and morphology, investigated using atomic force microscopy (AFM) and scanning electron microscopy (SEM) imaging, EDX and CL mapping were combined to identify the spatial distribution of the phases present in the films by correlating the composition and optical properties.

EDX maps were measured using an Oxford Instruments XMax80 X-ray detector in a Zeiss UltraPlus SEM, at an acceleration voltage of 10 kV and a beam current of $\sim$1 nA. The Cs-L, Pb-M and Br-L X-ray characteristic line series were used to analyze the composition of the samples. CL hyperspectral maps were measured using a SPARC system from Delmic in a Zeiss MERLIN SEM. The light was focused using a parabolic aluminum mirror through a quartz window outside the SEM and dispersed by a monochromator grating of 300 lines/mm blazed at 500 nm. A Kymera 193i spectrometer equipped with a Zyla 5.5 sCMOS camera from Andor was used to measure the spectra. The exposure time was varied during the acquisition between 20 and 100 ms to ensure good signal-to-noise ratio while avoiding detector saturation. CL measurements were performed at an acceleration voltage of 8 kV and a current of 200 pA for SC1 and 900 pA for SC2 and CE1. All the hyperspectral maps were treated by subtracting the background (acquisition with the same CL parameters, but with the electron beam blanked) and compensated with the system spectral transfer function. The energy position and intensity maps were obtained by fitting the spectrum at each pixel of the hyperspectral map to a sum of Lorentz functions, centered at the emission peaks (which were automatically detected).

The AFM topography maps were acquired in a Smart SPM-1000 from AIST-NT in tapping (AC) mode. We used a poly-silicon cantilever (HA FM/WC from TipsNano) with a nominal resonance frequency of 380 kHz and spring constant of 34 N/m for all measurements. All topography maps were flattened by subtracting an average plane. The roughness and thickness values were extracted from the AFM data using the Gwyddion software[137].

4.3.1 Single-step, spin-coated film

The SC1 film exhibits a porous matrix film with precipitate islands embedded in it, as shown in the surface topography maps in Figure 4.4. SEM of the cross section reveals that the precipitates are thicker than the matrix film. The thickness of the precipitates, measured with the AFM, is between 700 and 750 nm, $\sim$ 3 times thicker than the matrix film, which thickness

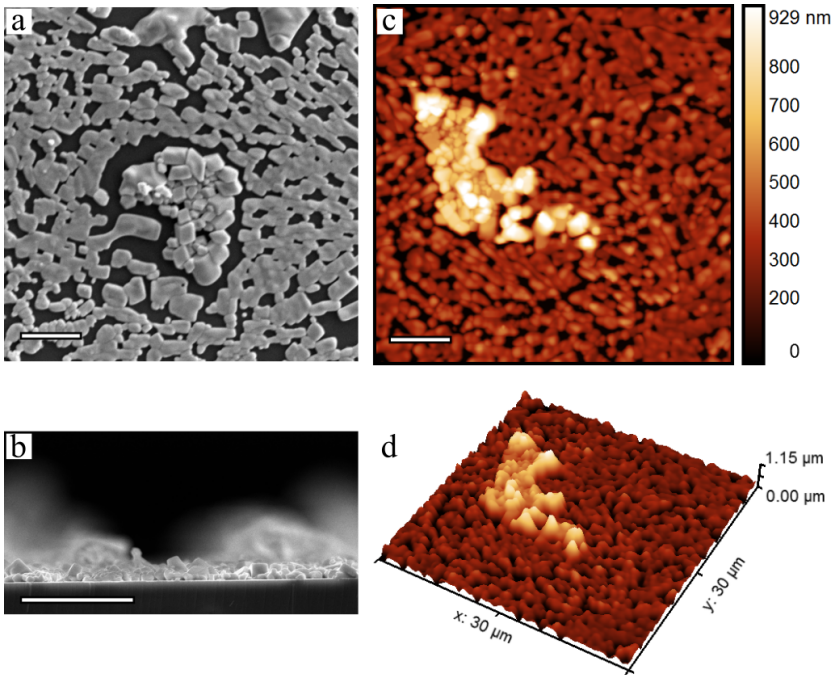

Figure 4.4: Morphology and topography of the single-step, solution-processed film, spin-coated on a glass substrate, SC1. SEM images of (a) the surface and (b) the cross section, and AFM (c) image and (d) 3D topography. Note that the precipitates are about three times thicker than the matrix film. All scale bars are 5 micron. Figure taken from Caicedo-Dávila et al. [109]

was measured between 250 and 300 nm. It is important to point out here that the SEM and AFM maps in Figure 4.4 are only sample maps, representative of the overall topography. The measurement of the thickness was averaged over a larger area of 100×100 µm^2.

The composition of the film and the different regions — islands and matrix film — was investigated using EDX mapping. Figure 4.5 shows the elemental maps for Cs, Pb and Br over a region that includes both matrix film and precipitates. No difference was measured between the precipitate and the matrix region in the Br map. In contrast, the Cs map exhibits stronger signal in the precipitate region, while the Pb signal in the same region is weaker. A line scan was extracted across the precipitate (including a region of matrix film around it), in which the enhancement in Cs signal and the depletion in Pb is measurable. Table 4.3 summarizes the net counts averaged on the different regions — precipitates and matrix — and their count ratio. Since the quantitative analysis is sensitive to the choice of k ratio, and requires a well calibrated standard[97], the average counts are used for EDX analysis, instead of giving absolute values. This serves as a measure of the changes in composition of one phase, relative to the other. The EDX atomic percentage — calculated with k ratios provided in the Oxford Instruments library — is also included as a reference.

Table 4.3: Average EDX net counts measured on the various regions of the SC1 film. The elemental concentrations in at% on each region are given in parentheses. The corresponding ratios between regions **R1** and **R2** are also provided

Region	Cs-L counts	Pb-M counts	Br-L counts
R1. Precipitates	29 **(37)**	40 **(9)**	195 **(54)**
R2. Matrix film	15 **(20)**	78 **(20)**	196 **(60)**
R1/R2 ratio	1.9 **(1.8)**	0.5 **(0.5)**	1.0 **(0.9)**

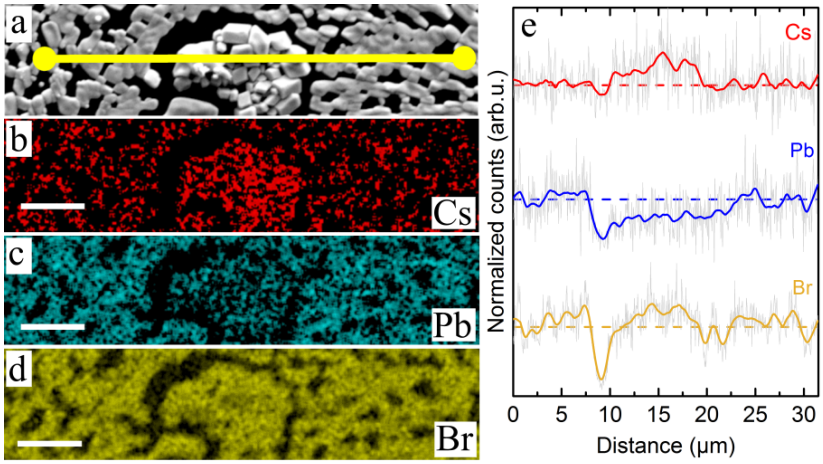

Figure 4.5: Composition of the single-step, solution-processed film, spin-coated on a glass substrate (SC1) shown in Figure 4.4 (a) SEM image showing the path used to obtain the EDX line scan in (e), and the corresponding composition maps, showing the distribution of (b) Cs, (c) Pb, and (d) Br. The precipitates exhibit an increase in Cs and depletion of Pb counts, compared with the matrix film, while Br remains constant, as confirmed by the line scan in (e). All scale bars are 5 µm. Figure taken from Caicedo-Dávila et al. [109]

The change in the Br-L counts between regions is negligible, Pb counts reduce to the half on the precipitates and Cs counts almost double. Considering the three ternary phases in the Cs–Pb–Br material system and calculating the ratios of atomic percentage for each of the phases, as summarized in Table 4.4, it was possible to assign $CsPbBr_3$ to the matrix film and Cs_4PbBr_6 to the precipitates. The elemental concentrations calculated using the k ratio from the Oxford Instruments library also agree well with those theoretical ones when assuming $CsPbBr_3$ and Cs_4PbBr_6 phases, as listed in the first section of Table 4.4. These results agree well with the phases detected by means of XRD.

Table 4.4: Elemental concentrations (at.%) in the ternary phases of the Cs–Pb–Br material system. The ratios of atomic percent for the different combination of ternary phases are also given

Phase	Cs (at.%)	Pb (at.%)	Br (at.%)
$CsPbBr_3$	20.0	20.0	60.0
Cs_4PbBr_6	36.4	9.1	54.5
$CsPb_2Br_5$	12.5	25.0	62.5
$Cs_4PbBr_6/CsPbBr_3$	1.82	0.45	0.91
$CsPbBr_3/CsPb_2Br_5$	1.6	0.8	1.04
$Cs_4PbBr_6/CsPb_2Br_5$	2.95	0.36	0.87

In addition to the composition, the microscopic emission properties of the films were investigated by means of CL on the exact same area where the EDX maps were acquired. CL maps in Figures 4.6a, and b show that the matrix film is luminescent and the precipitates dark in the probed spectral region — between 1.7 and 2.6 eV. The accumulated CL spectrum over the measured region, shown in Figure 4.6c, exhibits a narrow emission peak at 2.35 eV with a FWHM of 82 meV, consistent with the measured PL spectrum in Figure 4.3a. CL intensity maps were also acquired using the PMT, in order to be able to detect weak signals that may not be recorded by the CL hyperspectral map, owing to the optical losses of the system. The

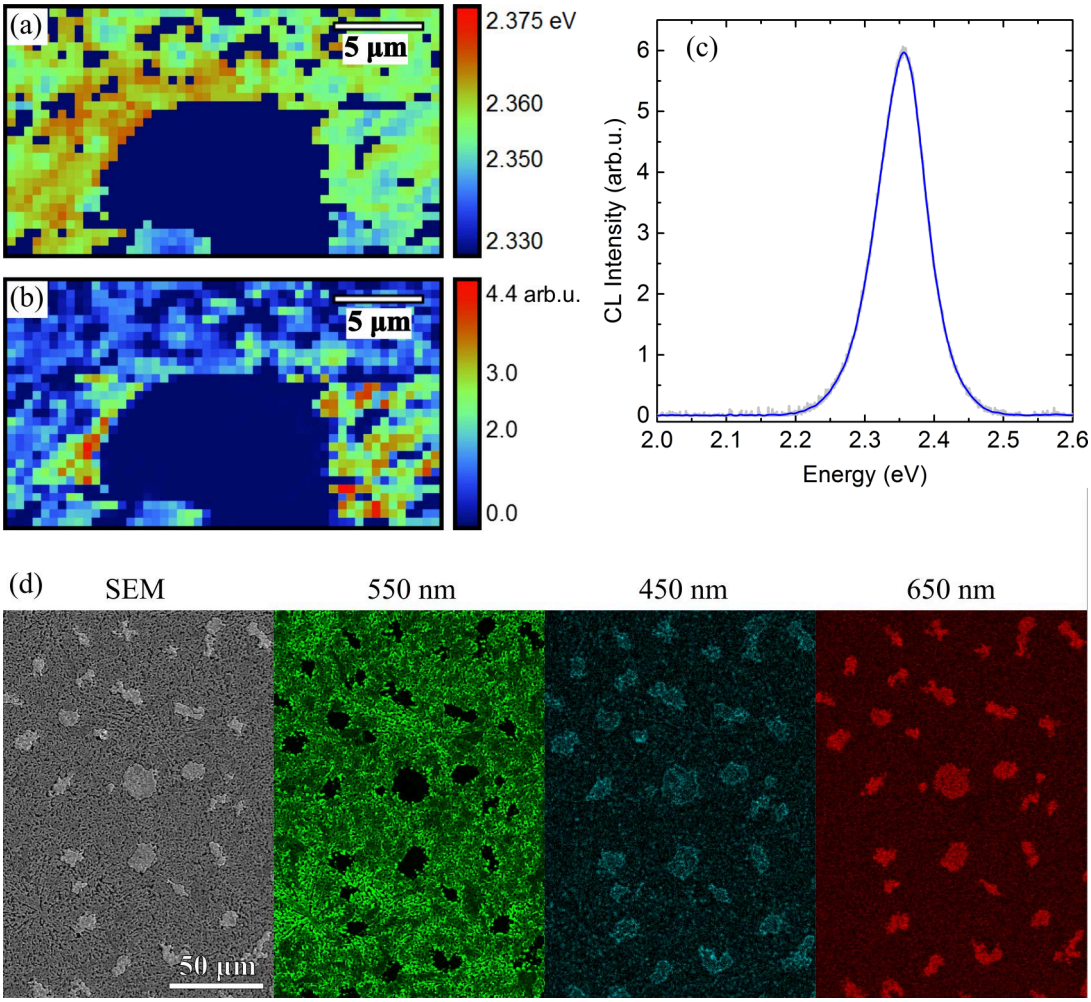

Figure 4.6: CL maps of the spin-coated film on glass (SC1): (a) map of the energy position of the CL emission peak, (b) hyperspectral CL intensity map, (c) accumulated CL spectrum, and (d) CL intensity maps at different emission wavelengths, showing the difference of emission between precipitates and matrix film. The precipitates show no measurable CL response in the green region of the visible spectrum, whereas the matrix film exhibits a strong luminescence at 2.35 eV with no significant changes of peak position. Figure adapted from Caicedo-Dávila et al. [109]

CL intensity maps in Figure 4.6d were acquired using band-pass filters with a bandwidth of 50 nm, centered at wavelengths of 450, 550 and 650 nm. These maps show that the precipitates exhibit emission at energies both higher and lower than the matrix film, but are completely dark in the green spectral region (550 nm). Considering that Cs_4PbBr_6 has been reported to be a direct semiconductor with band-gap energy of ~4.1 eV, the emission of the precipitates cannot be attributed to the band-to-band transition of Cs_4PbBr_6. However, recent theoretical work by Yin et al. [68] showed that Cs_4PbBr_6 can exhibit deep transition levels that could give rise to emission at energies comparable to the ones detected in the CL intensity maps. A quantification of exact energy positions is not possible in the CL experiments.

4.3.2 Two-step, spin-coated film

In contrast to SC1, the SC2 film features a small-grain, closed film with islands precipitated on top of it, as shown in Figure 4.7. These "cauliflower" shaped precipitates are micrometer-sized and exhibit a high contrast ratio with the underlying film, when measured using the in-lens

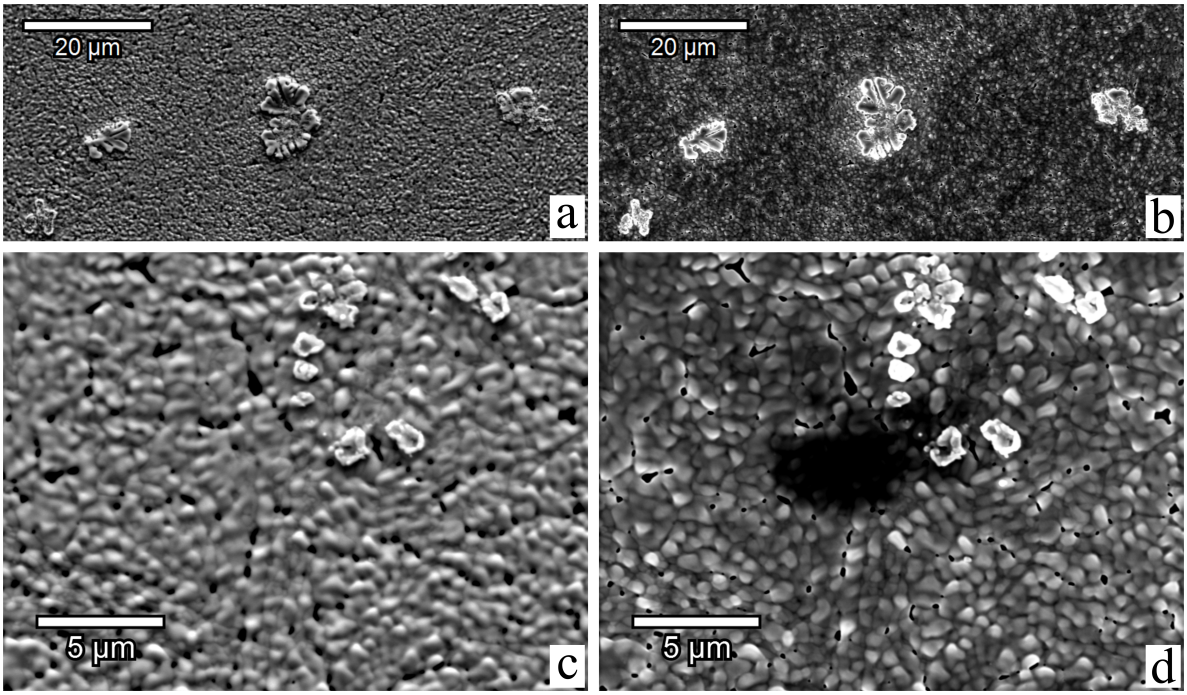

Figure 4.7: SEM images of the two-step, solution-processed film on a glass substrate (SC2). (a) and (b) show the film and the cauliflower precipitates on top; (c) and (d) show magnified images and the small-grain underlying matrix film. The images acquired with the in-lens detector — (b) and (d) — show the high contrast in the precipitates region, associated with a different surface potential. Figure reproduced with permission from Caicedo-Dávila, Funk, et al. J. Phys. Chem. C **2019** 123, 29, 17666 - 17677. Copyright 2019 American Chemical Society.[109]

secondary electron detector. Low-energy electron images acquired by this detector provide information on surface properties, such as the surface potential of the material. Thus, the SEM images in Figures 4.7b and d suggest that the precipitates are of a different material than the matrix film.

The composition maps of the film measured by EDX (Figure 4.8) exhibit a similar behavior to those of the SC1 film. However, the Cs enrichment and the Pb depletion on the islands is much stronger than for the SC1 film. Table 4.5 shows the average counts for the composing elements and the precipitate-to-matrix ratio, and the estimated atomic concentrations (in at.%) as reference.

Table 4.5: Average EDX net counts measured on the various regions **R1** and **R2** of the SC2 film. The elemental concentration in at.% on each region is written in bold font and parentheses. The corresponding ratios between regions are also given

Region	Cs-L counts	Pb-M counts	Br-L counts
R1. Precipitates	136 **(41)**	93 **(8)**	410 **(51)**
R2. Matrix film	47 **(20)**	195 **(20)**	393 **(60)**
R1/R2 ratio	2.9 **(2.0)**	0.5 **(0.4)**	1.0 **(0.9)**

The relative composition of matrix/precipitates cannot be assigned to any of the ternary phases (see Table 4.4). Since the elemental concentration estimated from EDX suggests that the matrix film is the $CsPbBr_3$ phase, the composition of the precipitates can be attributed to phase mixtures, most likely $CsPbBr_3 + CsBr$. This is confirmed by the XRD patter (Figure 4.2b), which indicates that the film contains the binary precursor CsBr.

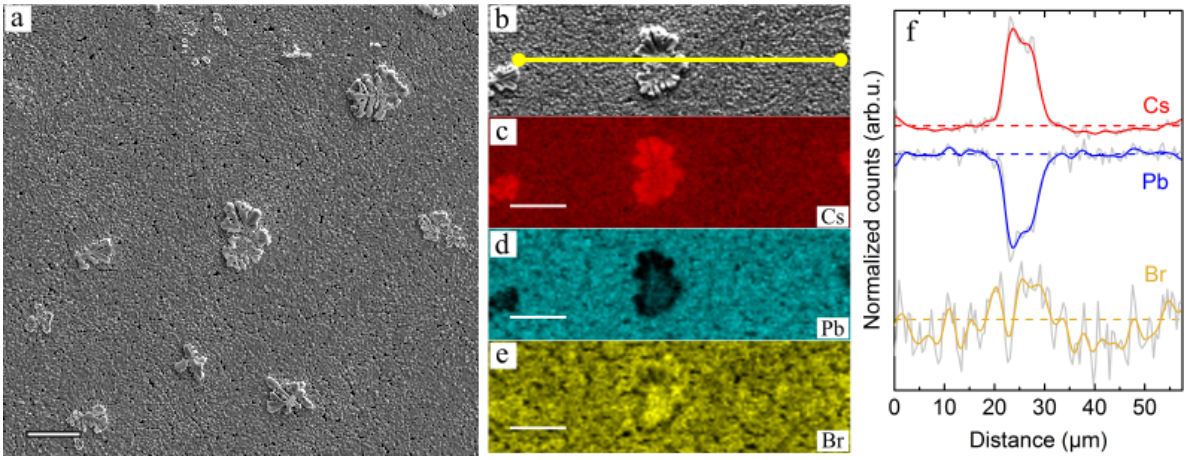

Figure 4.8: (a) SEM image of the Cs–Pb–Br film deposited with the two-step solution process. (b) Section of the SEM image showing the path of the line scan in (f), The corresponding elemental maps showing the distribution of (c) Cs, (d) Pb, and (e) Br are also shown. Note the secondary phase islands deposited on top of the film, which exhibit strong enhancement of Cs and depletion of Pb. All scale bars are 10 µm. Figure reproduced with permission from Caicedo-Dávila, Funk, et al. J. Phys. Chem. C **2019** 123, 29, 17666 - 17677. Copyright 2019 American Chemical Society [109].

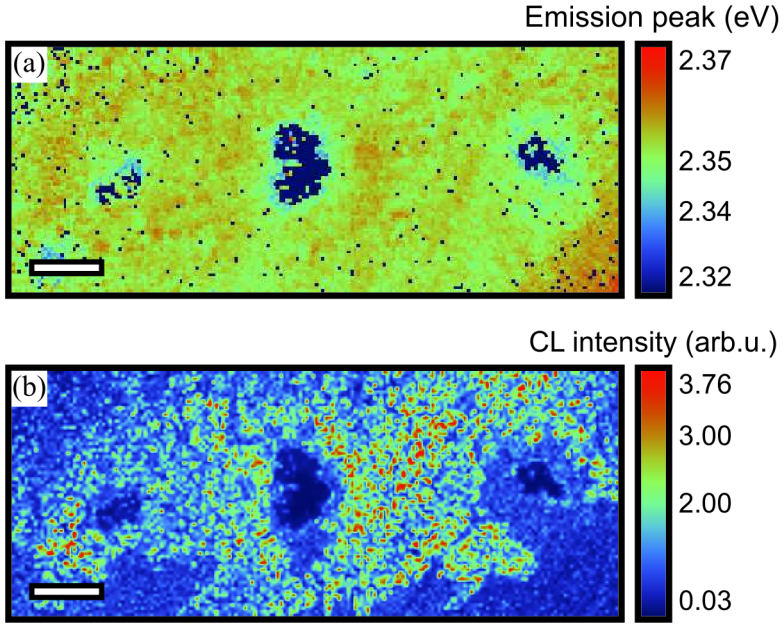

Figure 4.9: CL emission maps of the two-step, solution processed film deposited on glass shown in Figure 4.7. (a) Energy position map of the CL peak and (b) CL intensity. The islands on top of the film are dark in the visible range. All scale bars are 10 µm. Figure adapted from Caicedo-Dávila et al. [109]

CL measurements in Figure 4.9 of the exact same position reveal that the matrix film exhibits uniform luminescence at 2.35 eV, —characteristic of the $CsPbBr_3$ phase — confirming the EDX results. Similar to the SC1 film, the emission is quenched on the Cs-enriched, Pb-depleted precipitates.

Finally, EDX and CL correlative analysis of the cross-section of the film — shown in Figure 4.10 — reveals that the $CsPbBr_3$ phase is homogeneously distributed throughout the whole

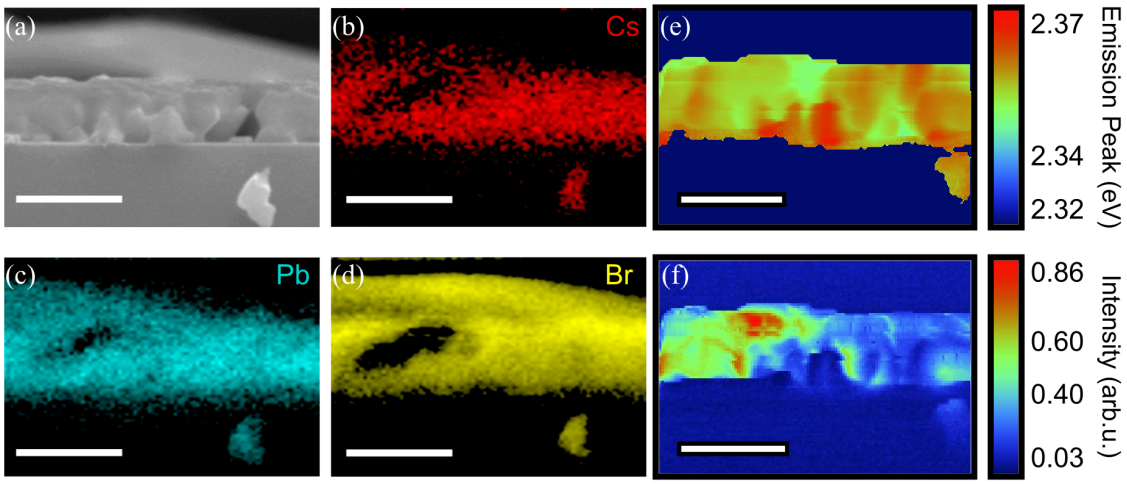

Figure 4.10: (a) SEM image of the cross section of the two-step, solution-processed film on glass, and its corresponding composition maps showing the distribution of (b) Cs, (c) Pb, and (d) Br. No composition changes were detected along the cross section of the film. The CL emission maps showing the (e) peak energy position and (f) intensity, exhibit a rather uniform transition energy and intensity distributions. All scale bars are 1 µm and the exposure time for the CL measurements was 20 ms. Figure adapted from Caicedo-Dávila et al. [109]

film thickness. This deposition method produced the most uniform closed film among the ones studied in the present thesis.

The microscopy analysis does not reveal the presence of $CsPb_2Br_5$. It is possible that the $PbBr_2$ film spin-coated during the first step has a nonuniform distribution over the substrate, leading to nonuniform reaction during the dipping step. Since the microscopic analysis was carried out only on the center of the sample — usually used as active device area — it might have missed the $CsPb_2Br_5$ towards die edges of the substrate.

4.3.3 Coevaporated films

The surfaces of CE1 and CE2 — in Figure 4.11 — exhibit closed films with apparent grain sizes of about few 10 to few 100 nm. The surface covered by the film exhibits height variations of tens of nanometers, which implies that the film thickness might change slightly over the film. Embedded within the film, micron-sized porous structures were found, which are between 200 and 230 nm higher than the film surrounding them, as revealed by AFM topography measurements shown in Figure 4.11. From AFM analysis the thickness (∼720 nm) and roughness (∼14 nm) of the film were also measured.

The SEM images acquired using the in-lens detector exhibit high contrast in the regions between the grains in the porous structures and in the regions of the closed film with smaller grains, as shown in Figures 4.11f and h. The contrast is more pronounced for the film coevaporated on Si (Figure 4.11f) than for that on glass (Figure 4.11f). Again, these results suggest a difference in surface potential and can imply a different composition of the high contrast regions regions. However, the EDX maps, shown in Figure 4.12, exhibit no difference in composition over a large area of the film, and the elemental concentrations (in at.%) — as in Table 4.6 — suggest a composition corresponding to the $CsPb_2Br_5$ phase, in good agreement with the XRD results.

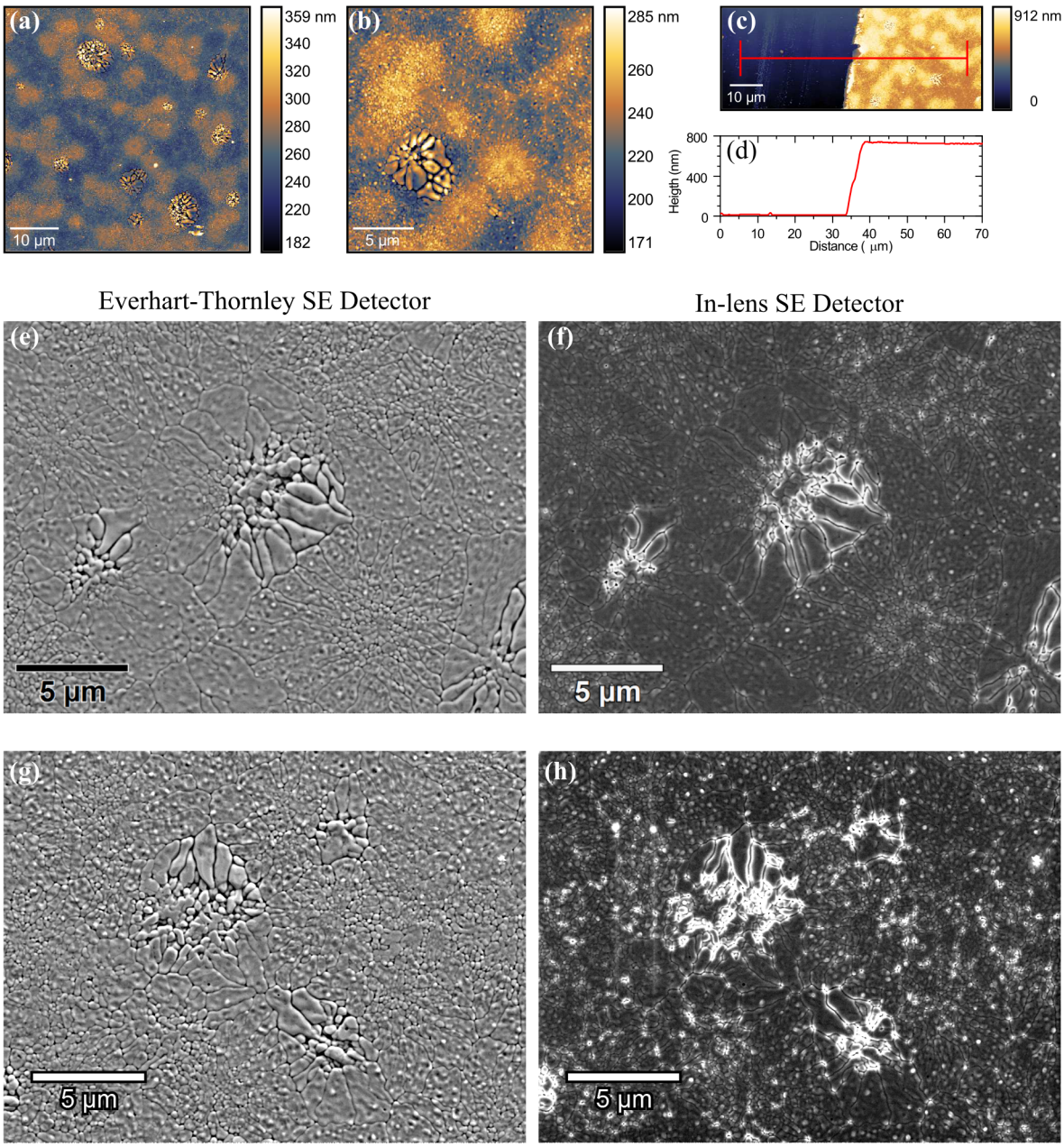

Figure 4.11: Morphology and topography of the coevaporated Cs–Pb–Br films. (a) AFM topography map of the film on a glass substrate, and (b) an enlarged topography map showing the structures embedded in the film and the surrounding closed film areas. (c) AFM topography of a section of the film and the glass substrate used to measure the film thickness, and (d) the line scan extracted from the profile shown in red. The thickness is in average 720 nm but slight variation along the film can be expected, as it is shown in the topography maps. SEM images measured using an Everhart-Thornley (e and g) and in-lens (f and h) secondary electron detectors of the film coevaporated on glass (e and f) and on Si (g and h). The morphology of the films is almost identical, with differences in the in-lens images, indicating a difference of the surface potential of the films.

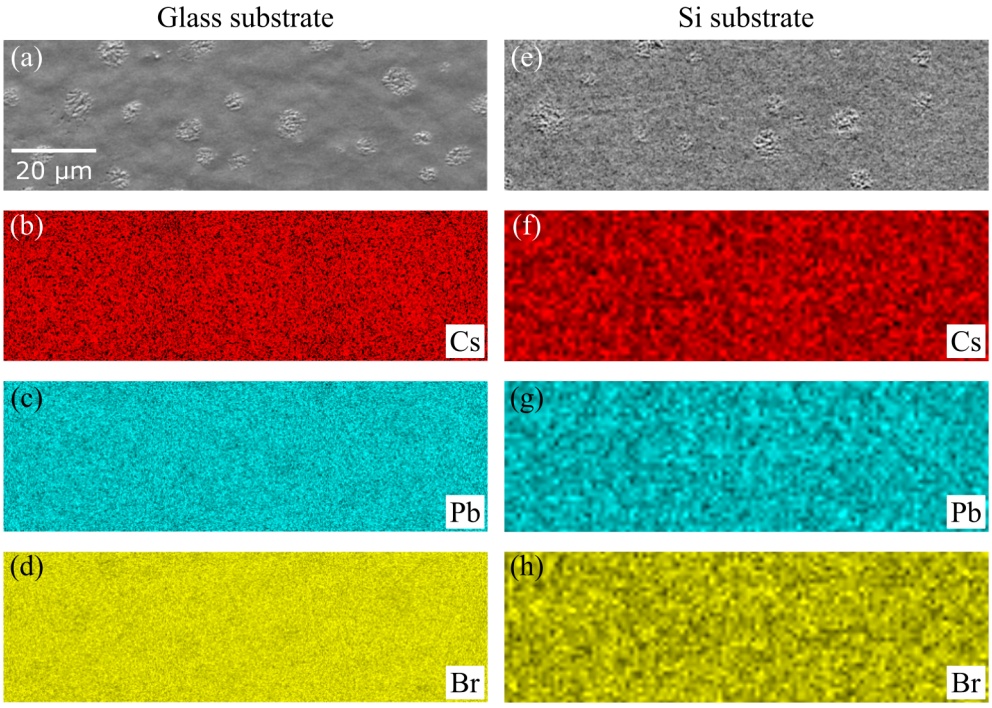

Figure 4.12: SEM images (a,b) and EDX elemental distribution maps using the (b,f) Cs-M, (c,g) Pb-M, and (d,h) Br-L lines of the films coevaporated on glass (a-d) and on Si (e-h). No change in the composition of the surface of the films was detected for either sample.

Table 4.6: Elemental concentrations in at.%, estimated from EDX on the surfaces of the coevaporated films

Film	Cs (at.%)	Pb (at.%)	Br (at.%)
CE1: glass substrate	13	25	62
CE2: Si substrate	13	25	62

CL maps were acquired on the same surface region (Figure 4.13) in order to investigate the optical properties and verify the uniformity of the composition. However, the surface exhibits a nonuniform distribution of the luminescence in the visible range, which contrasts to the uniform composition measured by EDX. The high-intensity luminescence regions (Figures 4.13a and d) correlate well with the the high-contrast areas measured with the in-lens detector (Figures 4.11f and h). This indicates that the surface potential difference measured with the in-lens detector is related to the luminescence. Additionally, hyperspectral CL mapping reveals that the intensity and the emission energy position measured on the surface are also correlated: The regions of high-intensity luminescence are characterized by sharp (130 meV) transitions at 2.35 and 2.38 eV for CE1 and CE2, while the regions of low-intensity luminescence exhibit a broad (620 meV) emission at ~ 1.7 eV.

Notice that, in contrast with the solution-processed samples, the PL and CL spectra of the surface of the coevaporated films exhibit some important differences: First, a low-energy peak appears in the CL spectrum, which was absent in the PL spectrum; second, the energy position of the emission peak in the green spectral region in the film coevaporated on glass exhibits a blue shift with respect to the PL peak; and third, the width of the green emission peak (2.35 to 2.38 eV) of the CL spectrum is considerably larger than that of the PL spectrum.

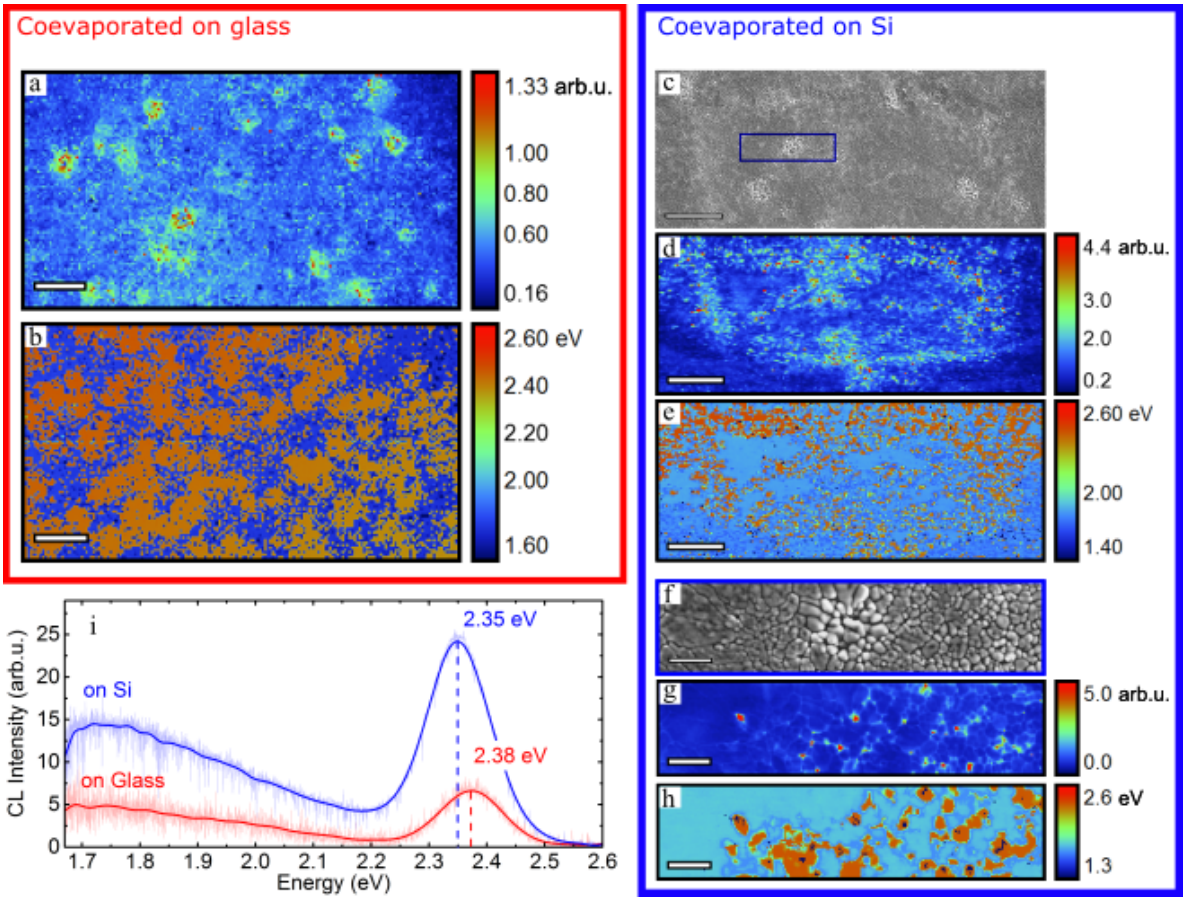

Figure 4.13: CL emission maps of the Cs–Pb–Br films coevaporated on (a,b) glass and (c–h) Si substrates: (a) CL emission intensity map showing the distribution of the integrated luminescence on the surface (same area as in Figure 4.11e). (b) The CL peak energy position map. (c) SEM image of the surface of the film coevaporated on Si, (e) CL intensity and (d) CL peak energy position over the surface. (f) SEM image of a magnified region (shown in the blue rectangle), the corresponding (g) CL intensity and (h) CL peak position. The green emission dominates in the small- grain areas and between the cracks of the structures. (i) Accumulated CL spectra of both films (on glass and Si), showing the blue shift and broadening of the green band for the film on glass. Scale bars in (a–e) are 10 and 2 µm (f–h). Figure taken from Caicedo-Dávila et al. [109]

These differences are discussed in detail later in Section 4.3.4, but first the origin of these emission peaks was identified.

The high-energy, green emission can be assigned to the characteristic emission of $CsPbBr_3$ and the low, broad energy is similar to defect emission[93, 138], which origin we will discuss in detail in Chapter 5. Having established the existence of the $CsPbBr_3$ by means of XRD and CL, and having found no correlation with the composition measured by EDX, opens the question of how the phases are spatially distributed. To further investigate this question, cross-sectional correlative analysis was performed. In the CL maps in Figure 4.14 two layers with different emission maxima were identified. These emissions are similar to the ones measured on the surface of the film and allow identifying two different layers: a highly luminescent bottom layer, with a sharp (82 meV) emission peak at 2.35 eV and a low luminescent top layer with a broad (470 meV) emission at 1.8 eV. The EDX cross-sectional maps and line scans in Figure 4.15 reveal a difference in composition between the layers. The bottom layer exhibits Cs enrichment and a slight Pb depletion with respect to the EDX net counts measured on the surface layer. The EDX results are summarized in Table 4.7. The Cs trend agrees well with the

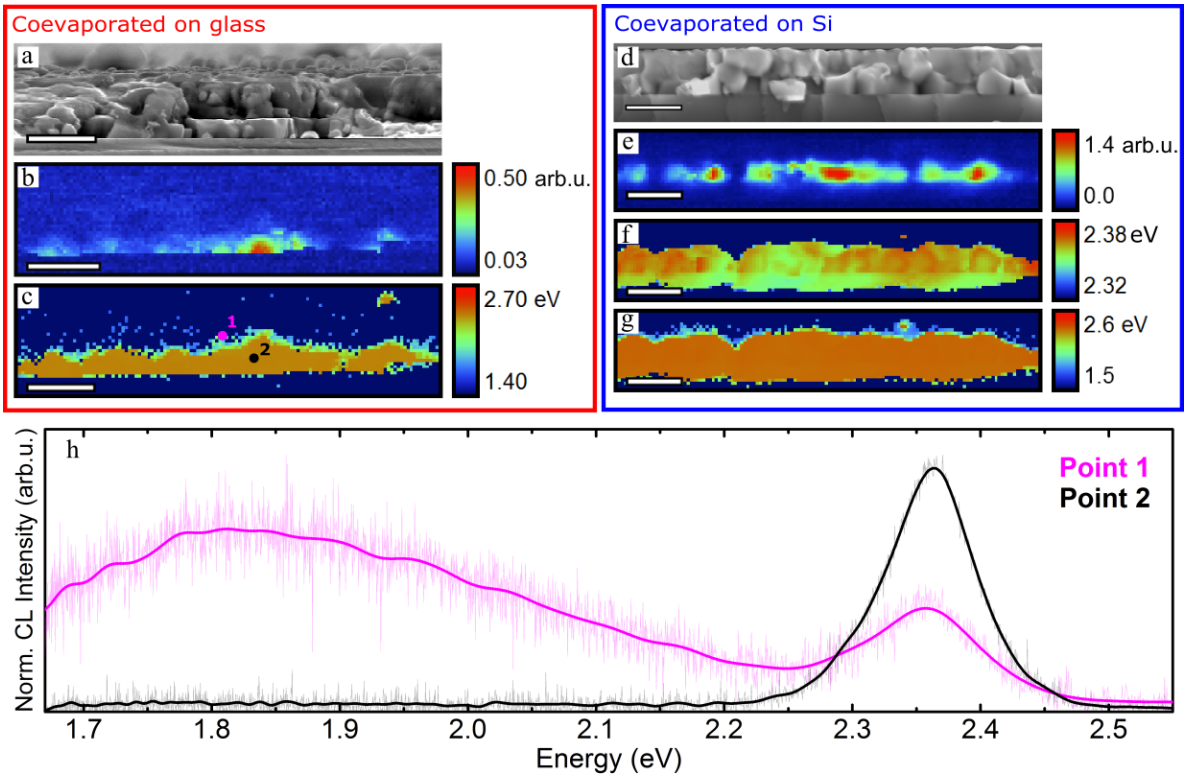

Figure 4.14: CL emission maps of a cross section of the Cs–Pb–Br films coevaporated on glass (a–c) and Si (d–11g): (a and d) SEM images, (b and e) corresponding CL intensity, and (c and f) CL peak energy position maps. Both films exhibit a highly emissive —green region of the spectrum— bottom layer. Low-intensity (red) luminescence characterizes the surface layer, as shown in the (h) normalized CL spectra of points 1 and 2 in (c). (g) Representation of the same map as in (f) in a different energy scale. This map also shows the red-luminescent surface layer, where as the map in (g) shows the thickness and variation of the green-luminescent bottom layer. All scale bars are 1 µm. Figure taken from Caicedo-Dávila et al. [109]

CL intensity extracted from the cross section, plotted in Figures 4.15c and d, together with the EDX line scans. Assuming the $CsPbBr_3$ composition for the bottom layer — since it exhibits the characteristic green emission and it has a notable correlation with the luminescence — the composition of the surface layer was estimated as that of the $CsPb_2Br_5$ phase. Additionally, the elemental concentrations estimated from EDX (also in Table 4.7) agree with this phase distribution as well.

This finding was confirmed by atom-probe tomography (APT) measurements kindly performed by Dr. Oana Cojocaru-Mirédin, at RWTH-Aachen. The APT measurements were performed on the CE2 film, by preparing the specimen using focused ion beam (FIB) milling as described in reference [139], taking care of minimizing the damage by using a low energy — 2 keV — Ga beam in the final milling stage. The measurement was performed by a CAMECA LEAP 4000X Si instrument with UV laser pulses of 355 nm wavelength, 10 ps pulse length and 2 pJ pulse energy, at a temperature of 50 K.

The APT results, shown in Figure 4.16, reveal three distinctive regions with different elemental concentrations for Cs, Pb and Br, as reported in Table 4.8. The composition of the Br-rich surface — region (i) — approaches to that of the $CsPb_2Br_5$, in good agreement with the EDX analysis of the surface of the film. The composition of region (ii) is in excellent agreement with that of the $CsPbBr_3$ phase. Finally, the composition of the Cs-rich region

Table 4.7: Average EDX net counts measured on the different layers of the CE1 and CE2 films. The elemental concentration in at% of each layer are written in bold font and parentheses. The corresponding ratios between layers L1 and L2 are also given

Layer	Cs-L counts	Pb-M counts	Br-L counts
Glass substrate (CE1)			
L1. Bottom	4352 **(16)**	25 336 **(22)**	54 295 **(62)**
L2. Surface	3097 **(11)**	29 855 **(21)**	57 111 **(68)**
L1/L2 ratio	1.0 **(0.9)**	0.8 **(1.0)**	1.4 **(1.4)**
Si substrate (CE2)			
L1. Bottom	1983 **(16)**	12 314 **(22)**	27 137 **(62)**
L2. Surface	1523 **(11)**	15 108 **(21)**	28 147 **(68)**
L1/L2 ratio	1.0 **(0.9)**	0.8 **(1.0)**	1.3 **(1.4)**

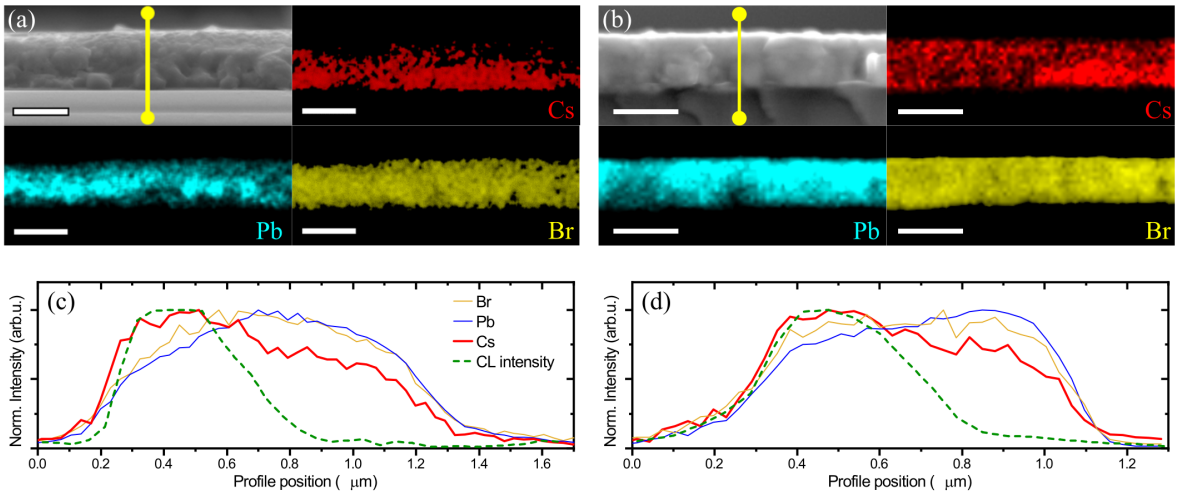

Figure 4.15: EDX elemental maps of a cross section of the Cs–Pb–Br films coevaporated on (a) glass and on (b) Si substrates. Each subfigure shows the SEM image of the cross section (showing the path used to obtain the EDX line scans in c and d), and the corresponding composition maps with the distribution of Cs, Pb and Br. The line scans show that the bottom layer exhibits a higher Cs content than the surface layer, while Pb exhibits an opposite trend. This can be associated with decrease in Cs and increase in Pb in the $CsPb_2Br_5$ phase. A line scan of the CL intensity is also plotted, which follows the behavior of the Cs content. All scale bars are 1 µm. Figure adapted from Caicedo-Dávila et al. [109]

does not agree with any of the known ternary phases in the Cs-Pb-Br material system, which might indicate the existence of a meta-stable phase, or be a consequence of beam damage induced during the sample preparation.

The result of this quantitative elemental analysis and the 2.35 eV emission detected in a similar region using CL, confirms that this phase is indeed the $CsPbBr_3$ perovskite, and that the absence of the Bragg peak at $2\theta = (21.55 \pm 0.09)°$ is an indication of a strong texturing in the coevaporated films.

4.3.4 On the particularities of the coevaporated films

Figure 4.13i shows the accumulated CL spectra measured at the surfaces of the CE1 and CE2 films. As mentioned above, upon examination of the CL spectra and comparison with the PL spectra in Figure 4.3 some differences can be noted, that are worth discussing in detail.

Table 4.8: Elemental concentrations (at%) in the regions along the CE2 film, as identified by APT measurements

Region	Cs (at.%)	Pb (at.%)	Br (at.%)
i) Br-rich surface	15	20	65
ii) Middle: $CsPbBr_3$	20	22	58
iii) Cs-rich	28	34	38

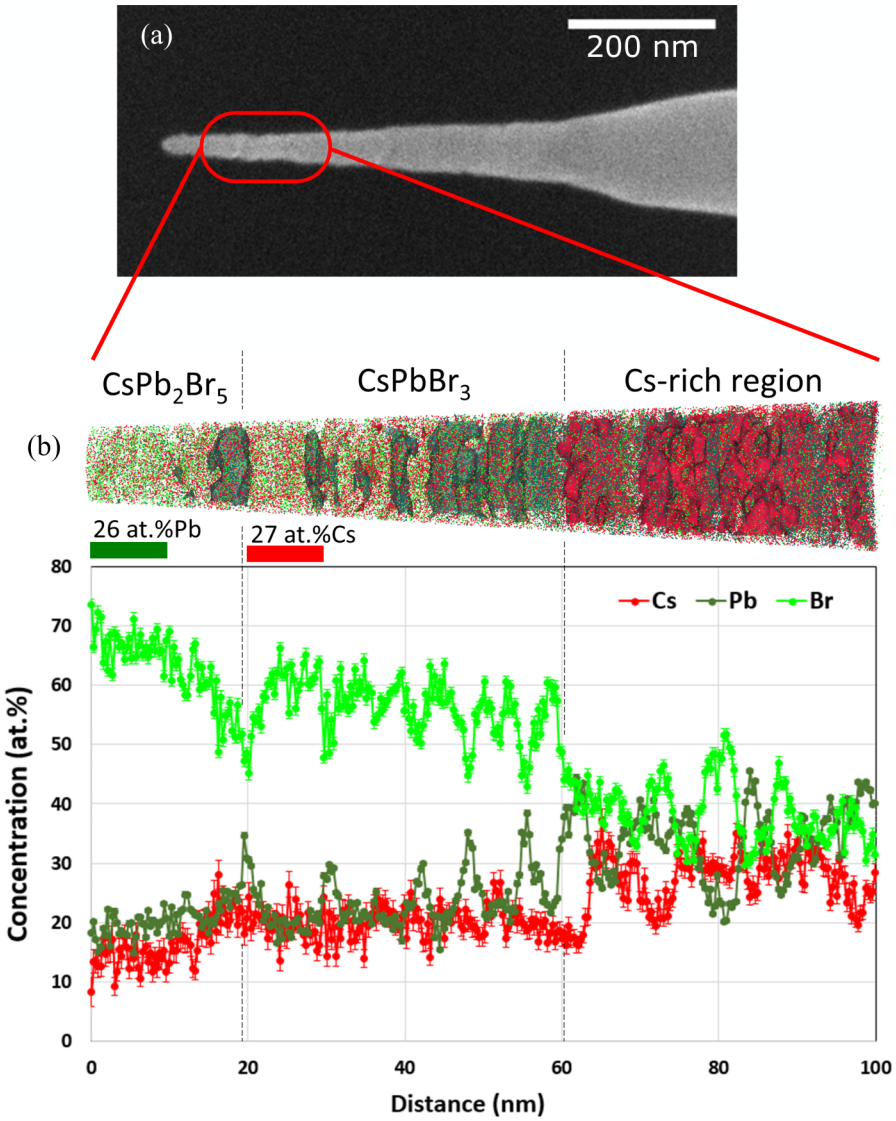

Figure 4.16: (a) SEM image of the tip milled out of the coevaporated film on Si (CE2) for APT analysis. (b) APT 3D elemental map together with the 1D concentration profiles for Br (light green), Pb (dark green), and Cs (red) of the sample shown in (a). Besides the expected $CsPbBr_3$ phase, this APT measurement reveals the presence of a Br-rich surface which approaches the composition of $CsPb_2Br_5$ phase and of a Cs-rich region deep inside the sample. The latter one could not be correlated to any of the ternary phases of the Cs–Pb–Br system. Figure adapted from Caicedo-Dávila et al. [109]

1. **A low-energy band** centered at $\sim 1.7\,\text{eV}$ appears in the CL spectra of the surface of both coevaporated films. This new peak can be explained considering the differences between laser and electron beam in PL and CL, and how they interact with the surface of the film. Since the phases are layered with the $CsPb_2Br_5$ — which is an indirect semiconductor with a band-gap energy of $\sim 3.1\,\text{eV}$[19] — on the surface of the film, the laser with a 409 nm wavelength is unable to excite the material on the surface of the film, and the PL spectra is measured from the $CsPb_2Br_5/CsPbBr_3$ interface. This results in a single sharp emission peak, as the one in Figure 4.3. On the other hand, the high-energy electron beam can excite the $CsPb_2Br_5$ on the surface. The low energy emission stems from this layer, as confirmed by the cross section analysis presented in Figure 4.14. This broad emission is characteristic of defects in this phase and will be discussed in detail in Chapter 5.

2. **The energy position of the green emission** peak in the CL spectra is different in the coevaporated films. This difference is larger than the thermal energy at room temperature, and since the films were deposited simultaneously and measured under the same experimental conditions, this difference might not be negligible. It can be explained considering the interaction between the electron beam and the sample: The interaction volume is defined by the penetration depth in Equation 3.4, and for the CE1 and CE2 films, it was estimated — using the density of the $CsPb_2Br_5$ phase on the surface, $\rho = 11.48\,\text{g/cm}^3$ [140] — to be $R_e \approx 195\,\text{nm}$. This means that, when measuring the surface of the film, the electron beam excites only the $CsPb_2Br_5$ phase in grain interiors, but it can reach deeper inside the film on the grain boundaries and in small grain areas, exciting the $CsPb_2Br_5/CsPbBr_3$ interface below the surface.

   Since the $CsPbBr_3$ layer in the CE2 film is thicker than that in CE1, as shown in Figure 4.14, the difference in the energy position of the CL spectra can be explained as follows: the CL signal in CE1 stems from the $CsPb_2Br_5/CsPbBr_3$. Due to the tensile strain at the interface, the electronic and optical gap of $CsPbBr_3$ increases, owing to the anti-bonding nature of the valence band maximum in $CsPbX_3$ compounds (X being Br, I or Cl).[67, 141] This results in a blue shift of the optical transition and is consistent with observations reported by Sebastian et al. [142] for temperature-induced strain.

   The penetration depth also clarifies the correlation between the CL maps and the SEM images acquired with the in-lens detector, and the correlation between intensity and peak position: the green luminescence of $CsPbBr_3$, centered at 2.35 eV, emits with higher intensity and it is more efficiently excited when the electron beam reaches the $CsPb_2Br_5/CsPbBr_3$ interface.

3. **The width of the emission peak** associated to the $CsPbBr_3$ phase is considerably larger in the CL than in the PL spectra. This broadening of the emission peak can be explained — following the argument in numeral 2 — as the result of ensemble average of the emission at the interface, where different depths — with different levels of strain — are excited. The result is the Gaussian broadening of the emission spectrum.

   The broadening effect was confirmed when we measured the CL spectra at two different points of the cross section, as in Figure 4.14h: the FWMH for point 2 ($CsPbBr_3$

bottom layer) is 92 meV, much smaller than that measured on the surface (130 meV) and comparable to the one measured with PL (82 meV).

The difference in the thickness of the $CsPbBr_3$ layer in CE1 and CE2 can be explained by the difference in thermal conductivity of glass and Si. This has an influence in the conversion dynamics at the post-evaporation step, described in Section 4.2.1.1. This phenomenon was investigating by annealing the sample after deposition. Figure 4.17 shows the CL of the CE1 and CE2 films as-deposited and after post-synthesis annealing at 100 °C for two hours. The thickness of the $CsPbBr_3$ layer increases with annealing mostly in the CE2 film, deposited on Si, which exhibits a thermal conductivity $\kappa = 1.3\,\mathrm{W/(cm\,°C)}$ [143],much larger than that of glass with $\kappa = 0.008\,\mathrm{W/(cm\,°C)}$[144]. The suggested phase transformation will be discussed in detail in Chapter 5.

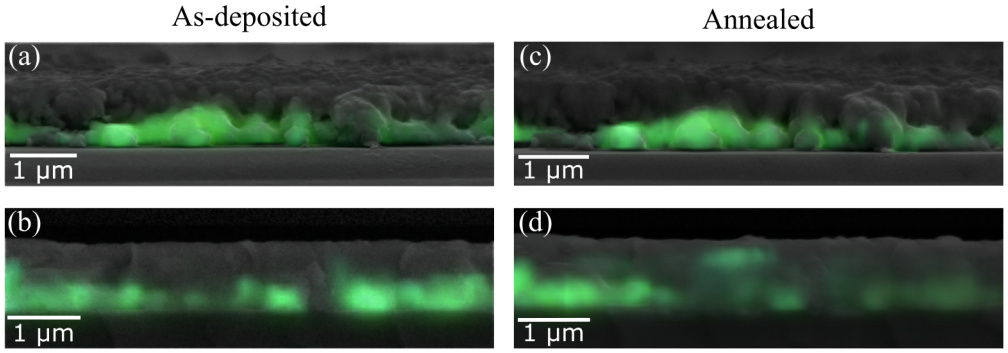

Figure 4.17: Overlay of the CL intensity map and the SEM image of the Cs–Pb–Br films coevaporated on (a) glass (CE1) and on (b) Si (CE2). The images of the samples after annealing at 100 °C are presented in (c) and (d). The thickness of the $CsPbBr_3$ bottom layer increases considerably for the film deposited on Si, while no appreciable change is observed in the film on glass.

4.4 Summary and discussion

In summary, the composition, structure and optoelectronic properties of Cs–Pb–Br thin films deposited using different recipes was investigated. XRD analysis showed that all of the films deposited by different deposition methods exhibit ternary phases, additional to the intended $CsPbBr_3$. PL spectroscopy showed that from the phases present in the film, only the $CsPbBr_3$ is optically active in the probed spectral range (visible), with a sharp band-to-band transition at 2.35 eV for all the films studied. Microscopic, correlative CL and EDX analysis showed that the spatial distribution seems to depend not only on the deposition recipe, but also on the substrate material. While the solution-based films do not exhibit a preferential orientation for the phase distribution, the phases in the coevaporated films distribute in a layered fashion, but their volume fraction depends on the substrate material. The findings are summarized in Figure 4.18.

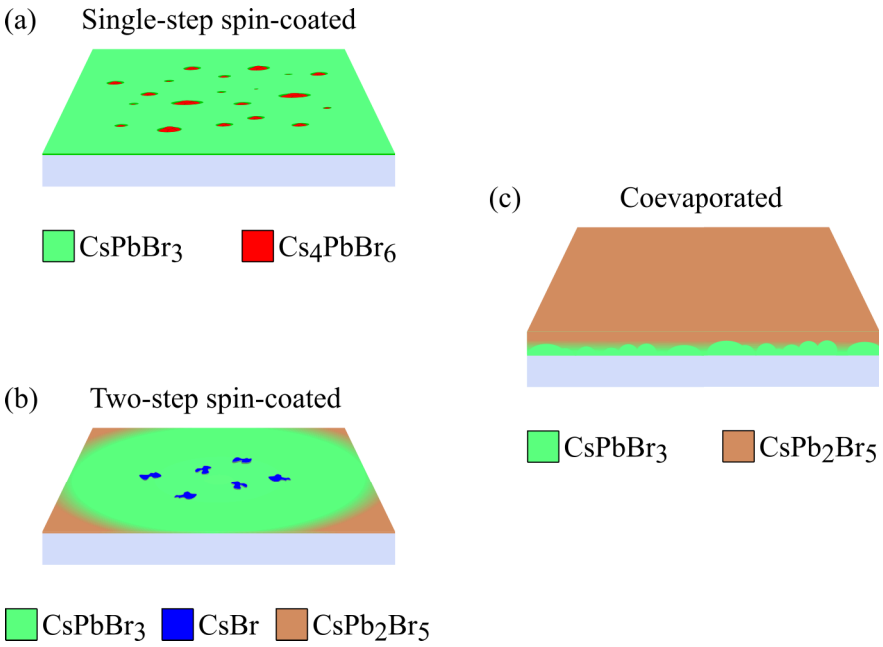

Figure 4.18: Summary schematic of the phase distribution in the various films analyzed in the present Chapter: (a) Single-step, solution-processed film, spin-coated on glass (SC1), (b) two-step, solution-processed film, spin-coated on glass (SC2), and (c) coevaporated film on glass (CE1). The latter is representative also of the phase distribution of the film coevaporated on Si. Each phase is represented with a different color and the size of the secondary phase domains are not to scale.

The different phases coexist due to their similar formation enthalpies, and the narrow stability area of the $CsPbBr_3$ perovskite phase, as shown by DFT calculations. The calculations presented here are in reasonable agreement with those reported by Jung et al. [145], which confirm the coexistence of $CsPbBr_3$ and Cs_4PbBr_6 because the narrow stability field of Cs_4PbBr_6 in chemical potential space. The luminescence of this phase has been a matter of debate. Some authors have published highly green luminescent Cs_4PbBr_6[63, 64, 66, 69, 70] and attributed the emission to recombination via intrinsic deep defect levelsline [68, 69, 71, 146], while others reported the large band gap energy of Cs_4PbBr_6 and assigned the green emission to hybridization with $CsPbBr_3$ [30, 52–55]. The correlative analysis presented here, which includes structural, optical, and compositional analysis provides enough evidence to conclude that the Cs_4PbBr_6 phase is non-luminescent. Furthermore, recent reports on correlative microscopy [147] — similar to the analysis described in detail in Chapter 6 — demonstrate that the green emission in Cs_4PbBr_6 stems from embedded $CsPbBr_3$ nanocrystals.

Finally, post-deposition annealing experiments suggest that phase transformation occurs upon temperature treatment of the coevaporated films. The details of this phase transformation and the influence of the different phases on the luminescence of mixed $CsPb_2Br_5/CsPbBr_3$ films are described in detail in Chapter 5.

5

Influence of phase transformation on the luminescence of mixed-phase films

Chapter 4 described the phase distribution of Cs–Pb–Br thin films synthesized using different deposition methods. It was also found that annealing can induce phase transformation in the films, increasing the thickness of the perovskite layer. In the present Chapter the details of this phase transformation process, and its influence on the optoelectronic properties and green luminescence of mixed-phase films will be studied in detail. For this purpose, the thin film coevaporated on Si (CE2) will be used, since as shown in Figure 4.17, the thermal conductivity of the substrate facilitates the phase transformation.

First, the results of structural, compositional, optical and microscopic characterization for the thin film as-deposited are summarized (detailed in Chapter 4). Second, the results of steady-state and time resolved photoluminescence (PL) are presented, and the estimated photoluminescence quantum yield (PLQY) and minority carrier lifetimes of the film as-deposited and after annealing at elevated temperature —up to 310 °C— are given. Third, the structural changes induced by the phase transformation process are monitored using in-situ X-ray diffraction (XRD). Finally, the microscopic origins that lead to the changes in the optical properties are investigated, and the results are compared with others available in the literature.

5.1 Effect of post-deposition annealing in the luminescence

5.1.1 Characterization of the film as-deposited

As discussed in Section 4.2.2.1, the coevaporated film contains both $CsPbB_3$ and $CsPb_2Br_5$. Both phases exhibit strong preferential orientation (texture) at room temperature: The former on the $\langle 110 \rangle$ (orthorhombic) direction, and the latter on the $\langle 001 \rangle$ (tetragonal) direction. The

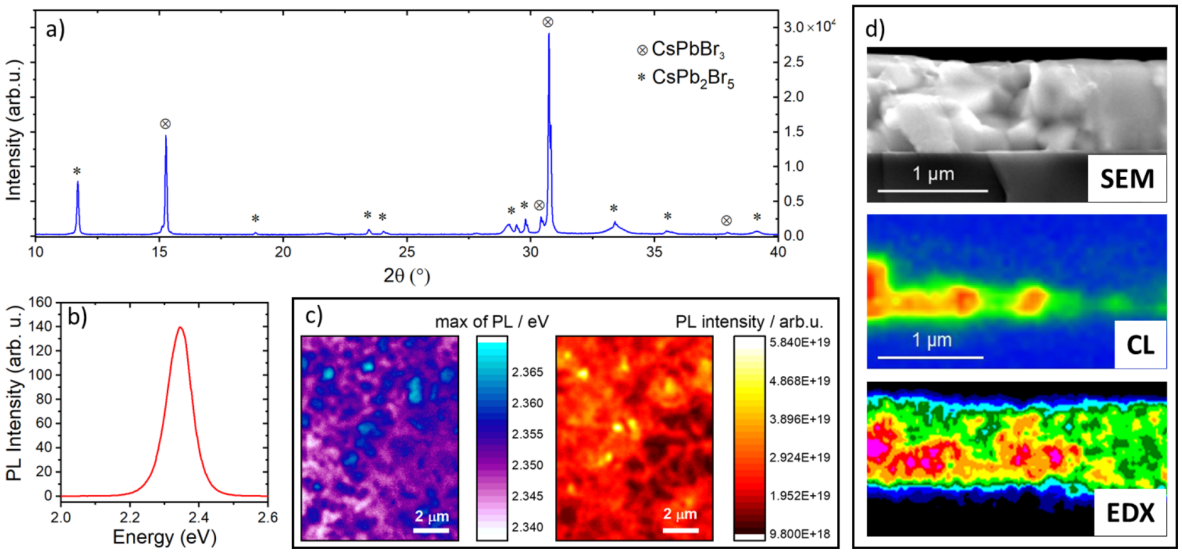

Figure 5.1: Summary of the characterization of the coevaporated mixed-phase $CsPbBr_3/CsPb_2Br_5$ film, as deposited: (a) XRD pattern, indexed using PDF 01-072-7929[130] for $CsPbBr_3$ and PDF 00-025-0211[57] for $CsPb_2Br_5$; (b) steady-state PL spectrum; (c) PL peak position and intensity maps of the film; (d) microscopic characterization of the film's cross section, including SEM image, CL and Cs elemental map on the same position. Figure reproduced with permission from Caicedo-Dávila et al. J. Phys. Chem. C **2020** 124, 36, 19514 - 19521. Copyright 2020 American Chemical Society [110].

PL spectrum exhibits a single, sharp (82 meV) peak at 2.35 eV, characteristic of the $CsPbBr_3$ phase. The phases are layered — as revealed by our microscopic investigation — with the green-luminescent, Cs-rich $CsPbBr_3$ at the bottom of the film, and the nonluminescent, Pb-rich $CsPb_2Br_5$ on the surface of the film. These results of the film as-deposited are summarized in Figure 5.1.

In addition to the characterization described in Chapter 4, absolute PL and hyperspectral images were acquired using a custom microscope setup in a wide field configuration. The surface of the film was excited with a 405 nm LED at an excitation fluence of $1.2 \times 10^{21}\,\mathrm{m^{-2}\,s^{-1}}$, equivalent to ~ 2 sun conditions, for a material with a band gap of 2.3 eV. The PL emission was collected through a tunable liquid crystal filter with a CCD camera, allowing wavelength selectivity. The intensity and peak position maps obtained from the hyperspectral images are shown in Figure 5.1c. Notice the uneven distribution of the luminescence intensity and PL peak energy position, similar to those obtained with CL, in Figure 4.13. The differences are explained by the inability of the 405 nm light to excite the $CsPb_2Br_5$ surface, as discussed in Section 4.3.4. This setup, calibrated to the absolute number of photons, allows to estimate the PLQY by integrating the PL spectrum and dividing by the excitation fluence. The estimated external quantum efficiency for the film as deposited was $Q_e^{PL} = 0.03\%$. Thanks are due to Dr. José A. Márquez for the absolute PL maps and PLQY measurements.

5.1.2 Optical properties after annealing

The film was then annealed at elevated temperature — 310 °C, 583 K — in N_2 for 2 h and the optical properties measured again. The external quantum efficiency is reduced below the detection limit — $\sim 0.001\%$ — of the absolute PL setup after annealing, a reduction of over one order of magnitude. The steady state PL spectra of the film before and after annealing are

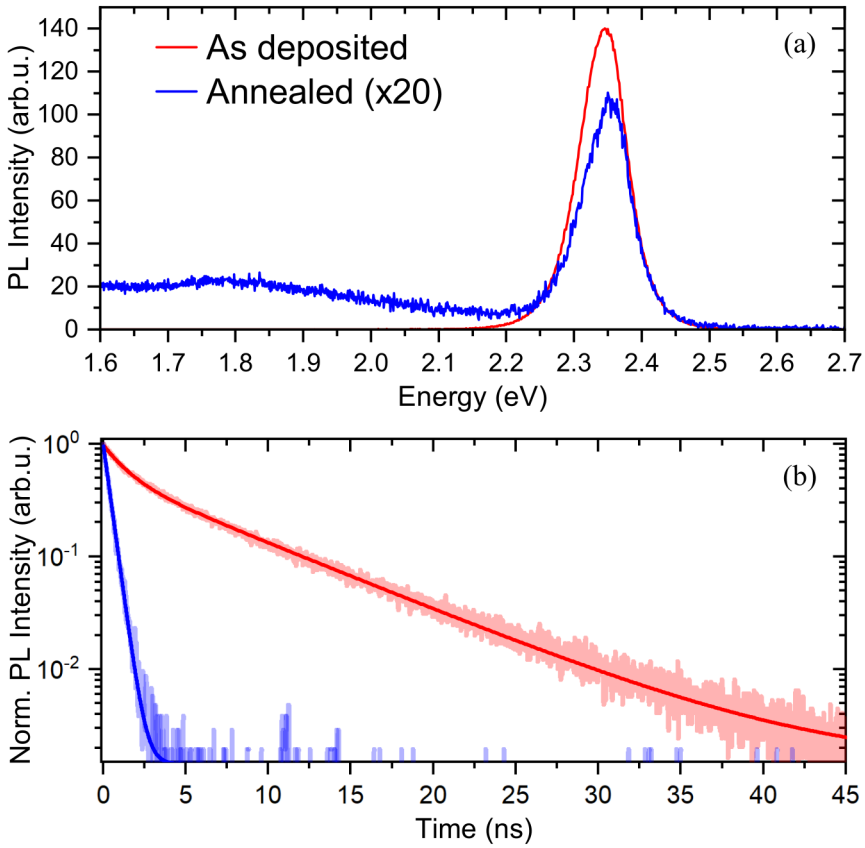

Figure 5.2: Optical properties of the mixed-phase Cs–Pb–Br film as-deposited (red) and after elevated temperature annealing: (a) PL spectra, and (b) TRPL measurement and fitted exponential decay. Annealing reduces the intensity of the 2.35 eV PL peak, characteristic of the $CsPbBr_3$ over 20 times (spectrum of the annealed film multiplied by 20 to improve visibitity). The lifetime drops about one order of magnitude after annealing. Figure adapted from Caicedo-Dávila et al. [110]

shown in Figure 5.2a. The PL intensity decreases over a factor of 20 and a low-energy band appears in the spectrum at 1.8 eV, similar to the accumulated CL spectrum on the surface of the film, in Figure 4.13. The time-resolved PL (TRPL), shown in Figure 5.2b, was measured using a 405 nm pulsed laser with a repetition rate of 1 MHz, at a power density of 0.08 W/cm^2. The signal of the laser excitation was removed using a 450 nm low-pass filter. Upon annealing, the minority carrier lifetime decreases 1 order of magnitude. The TRPL of the sample as deposited was fitted to a bi-exponential decay with a fast lifetime of $\tau = 1$ ns and a slow component of $\tau = 7$ ns, in good agreement with lifetimes of bulk $CsPbBr_3$ reported by Xu et al. [85]. The TRPL of the film after annealing could be fitted to a mono-exponential decay with a lifetime of $\tau = 0.4$ ns dominating the carrier dynamics.

5.2 In-situ monitoring of annealing-induced changes

5.2.1 In-situ XRD experiments

In order to understand the annealing-induced changes to the optical properties and how are they related to the phase transformation, the structrural changes in the film were monitored while annealing, using in-situ XRD. Six diffractograms were acquired (approximate acquisition time of a diffractogram was 20 min) per temperature step, at 8 different temperatures from 313 to 583 K.

The measurements were carried out in a Bruker D8 powder diffractometer, equipped with a high-temperature, ambient controlled chamber, in Bragg-Brentano configuration. A Cu-Kα radiation source ($\lambda = 0.154\,06$ nm) was used. The 2θ ranged from 10 to 60°, with a step size of 0.016° and an integration time per angle step of 96 s. The sample was heated in N_2 atmosphere (1130 mbar) and thermal expansion of the measuring stage was compensated. Figure 5.3 shows the last diffractogram measured at each temperature step (the sixth diffractogram) for all the different temperatures measured in the experiment. The first noticeable feature is a considerable increase in the intensity of some of the Bragg peaks, while others remain unaffected. Additionally, the change in peak intensity is accompanied by changes in their shape, as well as their 2θ position.

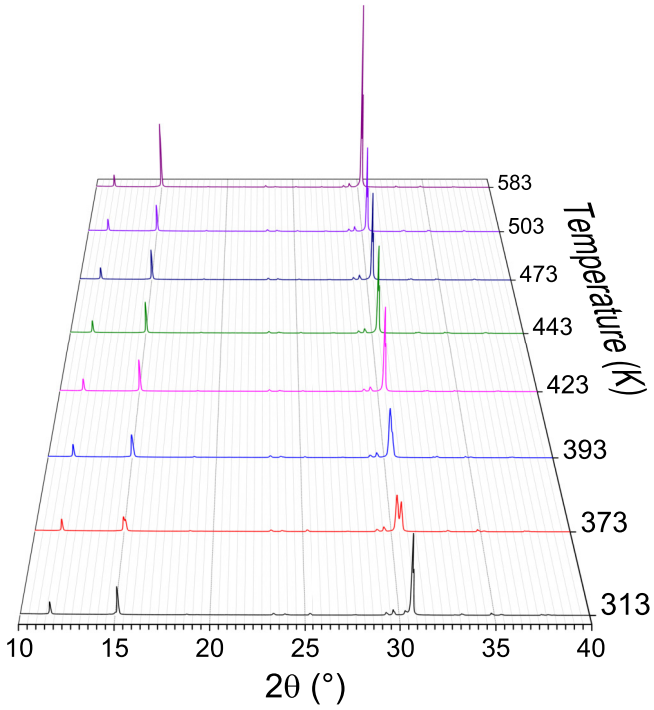

Figure 5.3: A series of diffractograms of the Cs–Pb–Br film at different temperatures, obtained by in-situ XRD, measured while annealing in N_2 atmosphere. Figure adapted from [110].

In order to understand better the phenomena during the annealing process, the peaks associated with the different phases were identified and contour maps constructed, which facilitate the evaluation of the changes in the Bragg peaks. Figure 5.4 shows these contour maps associated with four reflections of $CsPb_2Br_5$ and $CsPbBr_3$. First, notice that all of the reflections shift to lower angles — however, the shift for the $CsPb_2Br_5$ is considerably larger. This behavior is characteristic of thermal expansion of the crystal [89]. Second, the shapes of all of the Bragg reflections associated with the $CsPb_2Br_5$ crystal remain unchanged, as well their intensities. This suggests that the Pb-rich phase only expands with temperature, but no structural changes, crystallinity, or volume fraction changes are at hand.

In contrast, the shape and intensity of the Bragg reflections associated with $CsPbBr_3$ change considerably. For instance, the 004 and 220 reflections (at 30.4° and 30.7° at 313 K) of the *Pbnm* $CsPbBr_3$ transform into the 002 and 200 reflections of the $P4/mbm$ phase (at 30.30° and 30.49°) at 373 K. Then, at temperatures above 400 K both reflections merge into

the 200 one of the $Pm\bar{3}m$ $CsPbBr_3$ (at 30.43°). Finally, at temperatures above 400 K, the 200 reflection shifts to lower angles due to thermal expansion. Also, above 400 K the peak intensity increases sharply, which might suggest a better crystallinity or increased volume fraction, as it will be described later in this Chapter. The other reflections exhibit the same behavior. On Figure 5.4 the associated *hkl* for each reflection and the temperature regions of different crystal structures are provided on the contour maps for clarity and legibility.

To confirm the different $CsPbBr_3$ crystal structures, the lattice parameters at the different temperatures were estimated using the Le Bail method [149]. Figure 5.5 shows the results of the refinement of patterns at different temperatures, with different crystal structures of the $CsPbBr_3$. The lattice parameters estimated for each temperature are summarized in Table 5.1,

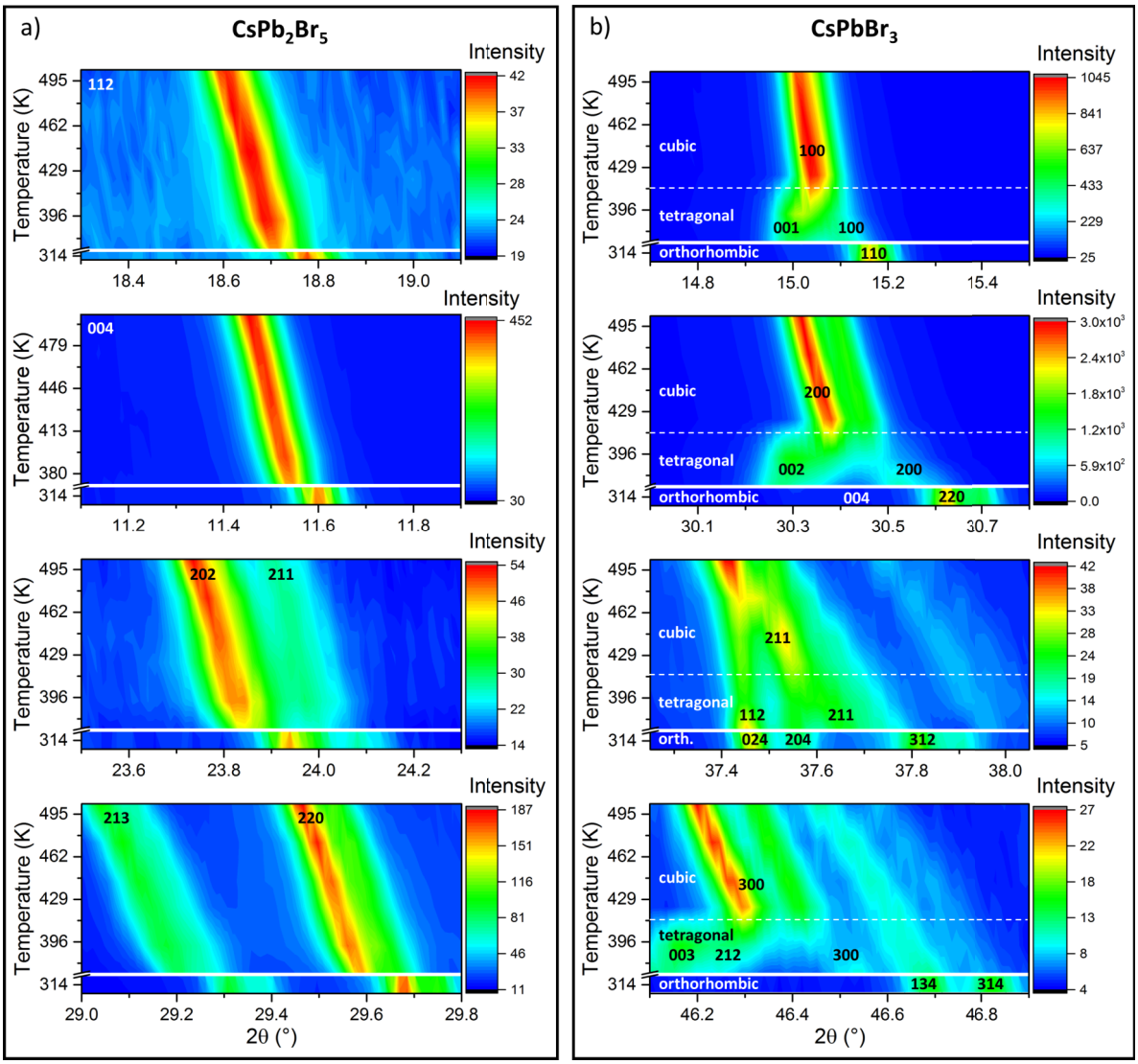

Figure 5.4: Contour maps showing the evolution with temperature of various diffraction peaks of (a) $CsPb_2Br_5$ and (b) $CsPbBr_3$. The Bragg reflections are identified in the Figure as well as the domains of orthorhombic [130], tetragonal [148], and cubic [130] phases of $CsPbBr_3$. The $CsPbBr_3$ peaks shape and intensity change as a function of temperature, indicating the orthorhombic–tetragonal–cubic phase transition and the increase in the $CsPbBr_3$ volume fraction. The $CsPb_2Br_5$ peaks only shift with temperature, but their changes in shape and intensity are negligible, indicating that only thermal expansion occurs. Figure reproduced with permission from Caicedo-Dávila et al. J. Phys. Chem. C **2020** 124, 36, 19514 - 19521. Copyright 2020 American Chemical Society [110].

and they agree well with the values reported for the different phases by Rodová, Brožek, and Nitsch [130] and Moller [148]. The structural phase transitions and transition temperatures also agree well with previous reports [24, 130], confirming this effect of the temperature on $CsPbBr_3$.

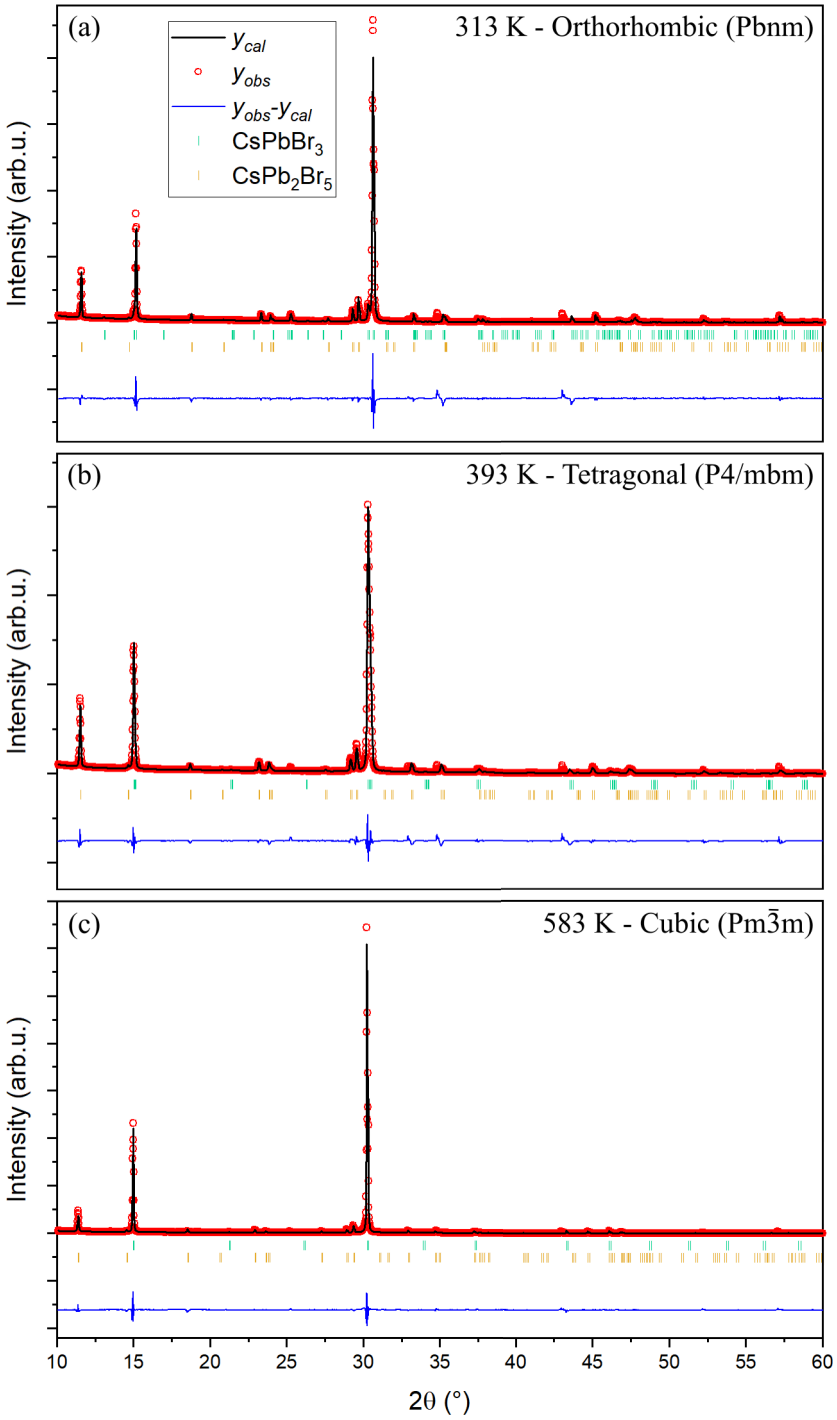

Figure 5.5: Illustrative results of Le Bail refinement at three different temperatures for each of the structural phases of $CsPbBr_3$: (a) orthorhombic, (b) tetragonal and (c) cubic. y_{obs}, y_{cal} as defined in Equation 3.2. Figure reproduced with permission from Caicedo-Dávila et al. J. Phys. Chem. C **2020** 124, 36, 19514 - 19521. Copyright 2020 American Chemical Society [110].

It is interesting to note that the strong ⟨110⟩ texture that the $CsPbBr_3$ exhibits at room temperature (in the orthorhombic crystal system) is not affected by temperature. The texture

Table 5.1: Lattice parameters of $CsPbBr_3$ estimated using Le Bail refinement for each temperature step of the in-situ XRD experiment. The different crystal structures are also given. These lattice parameters agree well with the ones reported in the literature Rodová, Brožek, and Nitsch [130] and Moller [148].

Temperature (K)	a (Å)	b (Å)	c (Å)
	Orthorhombic $Pbnm$ **(62)**		
313	8.240 ± 0.004	8.264 ± 0.004	11.780 ± 0.005
	Tetragonal $P4/mbm$ **(99)** — $a = b$		
373	5.858 ± 0.002	—	5.903 ± 0.003
393	5.866 ± 0.002	—	5.895 ± 0.002
	Cubic $Pm\bar{3}m$ **(221)** — $a = b = c$		
423	5.879 ± 0.002	—	—
443	5.881 ± 0.003	—	—
473	5.885 ± 0.002	—	—
503	5.890 ± 0.002	—	—
583	5.905 ± 0.001	—	—

remains when the crystal changes to the cubic structure to a strong $\langle 100 \rangle$. The $CsPb_2Br_5$ exhibits a similar behavior without structural transitions.

5.2.2 Integral intensity and breadth analyses

Owing to the strong texturing of the film, estimating the volume fraction of the phases accurately from refinement is not possible. However, since the film keeps its texture throughout the whole temperature range, a trend of the changes in the volume fraction can be estimated in a semi-quantitatively analysis, using the integral intensities of the diffraction peaks assigned to the different phases. First, each peak was fitted to a pseudo-Voigt function, described by:

$$f(x) = A\left(\mu\frac{2}{\pi}\frac{H}{4(x-x_0)^2+H^2} + (1-\mu)\frac{\sqrt{4\ln 2}}{\sqrt{\pi}H}e^{-\frac{4\ln 2}{H^2}(x-x_0)^2}\right), \tag{5.1}$$

where A is the area under the peak, H is the full width at half maximum (FWHM), μ is the fraction — between 0 and 1 — that determines how Cauchy (or Laurentzian) is the shape of the peak, x is the independent variable, which in the case of a diffraction pattern is 2θ, and x_0 is the center of the peak, i.e. the diffraction peak position.

After fitting each peak, the accumulated integral intensities can be estimated as the sum of the peak areas:

$$I(ph_i) = \sum_i \int f_i(x)dx = \sum_i A_i, \tag{5.2}$$

where the integral intensity of a particular phase, $I(ph_i)$, is the sum of the areas A_i of all the peaks assigned to that particular phase. The integration of the fitted functions $f_i(x)$ is easy because of the unity integral of the Cauchy and Gaussian parts of the function in Equation 5.1.

Using Equation 5.2, the integral intensities of both phases, $I(CsPbBr_3)$ and $I(CsPb_2Br_5)$ can be calculated, and the ratios between them, which were plotted as a function of temperature in Figure 5.8b. Clearly, $I(CsPbBr_3)$ increases with respect to $I(CsPb_2Br_5)$ as temperature increases. This suggests that the volume fraction of $CsPbBr_3$ in the film increases, and that the crystallinity of the $CsPbBr_3$ domains is enhanced at elevated temperatures.

In order to try to separate the volume fraction and domain size effects, we also evaluated the changes in the coherently diffracting domain using an integral breath method[89, 150], described in the following.

The profile of a diffraction peak obtained in an XRD experiment is a convolution of an instrumental and physical (domain size and strain) profiles[89]. Removing the instrumental part is essential for XRD analysis. Since the determination of the entire profile, and the deconvolution of an instrumental profile is impractical — and impossible in our experiments — simplified methods that depend on the measurement of profile widths (full width at half maximum, H; or integral breadth, β, defined as the ratio between the integrated intensity of the peak profile and the peak height) were used to remove the instrumental contribution. It is then possible to obtain the instrumental-corrected ("pure") profile width by assuming an analytical form for the profile of each diffraction peak. In the present work, a parabolic approximation correction was used [89, 150], which assumes that the instrumental broadening is described by a Gaussian function, and the "pure" profile by a Cauchy function. Then, the integral breadth of the measured peak can be defined as:

$$\beta = \beta_0 \left(1 - \frac{\beta_i^2}{\beta_0^2}\right), \tag{5.3}$$

where β is the "pure" breadth, β_0 and β_i are the measured and instrumental breadths of the same Bragg peak. A measurement of the NIST-SRM 660c LaB_6 standard was used as a reference material to obtain the instrumental breadth. The peaks of the diffractogram were fitted using, again, pseudo-Voigt functions (Equation 5.1) and the obtained Hs were used to fit the Caglioti's formula [151]:

$$H = (U \tan^2\theta + V \tan\theta + W)^{\frac{1}{2}}, \tag{5.4}$$

where U, V and W are fitting parameters. Using these parameters and Equation 5.4 the instrumental widths H_i at the position of the measured peaks were estimated. Since the instrumental broadening is considered Gaussian, the instrumental integral breadth, assuming a Gaussian shape is:

$$\beta_i = \frac{H}{2}\sqrt{\frac{\pi}{\ln 2}} \tag{5.5}$$

Then, using the experimental breadths, $\beta_0 = A/f(2\theta_0)$ (with $2\theta_0$ the peak center), the β_i estimated from Equation 5.5 and Equation 5.3, the "pure" integral breadth for domain size analysis was calculated.

Now, in order to separate the broadening effects owing to the changes in the domain size and strain, three methods were compared.

- **The Cauchy-Gaussian method** assumes that the Strain is approximated by a Gaussian profile, and the domain size by a Cauchy profile. The Equation describing the relationship between strain and domain size is[150]:

$$\frac{\beta^2}{\tan^2\theta_0} = \frac{K\lambda}{L}\left(\frac{\beta}{\tan\theta_0 \sin_0}\right) + 16e^2, \tag{5.6}$$

  where β is the instrumental broadening-corrected integral breadth (as described by Equation 5.3), β_0 is half the angle of the peak maximum position, L is the domain size, e is the "maximum strain", λ is the X-ray wavelength, and K is a constant that for practical purposes can be set to one[150].

- **The Gaussian-Gaussian method** assumes that both broadenings can be approximated by Gaussian profiles, and the equation describing the relation between strain and domain size is:

$$\beta^2 \cos^2\theta_0 = \frac{\lambda}{L} + 16e^2 \sin^2\theta_0 \tag{5.7}$$

- **The Williamson-Hall (WH) method**[152] assumes both strain and size broadening can be approximated as Cauchy profiles. The resulting equation is:

$$\beta \cos\theta_0 = \frac{\lambda}{L} + 4e \sin\theta_0 \tag{5.8}$$

Equations 5.6 to 5.8 can be fitted to line functions, from which the domain size L can be determined. Figure 5.6 shows the scatter plots for separation of domain size and strain using the three methods described above. The data points were extracted from evaluation of Equations 5.6 to 5.8, using the breadths calculated using Equation5.3 and the fitting procedure previously described. The set of Bragg peaks assigned to $CsPbBr_3$ and $CsPb_2Br_5$ were evaluated independently. The data points calculated using Gaussian-Gaussian and WH methods are substantially scattered and do not allow fitting a line, especially for low temperatures. The points calculated with the Cauchy-Gaussian method are less scattered and allow fitting of the line profile (Figure 5.6a).

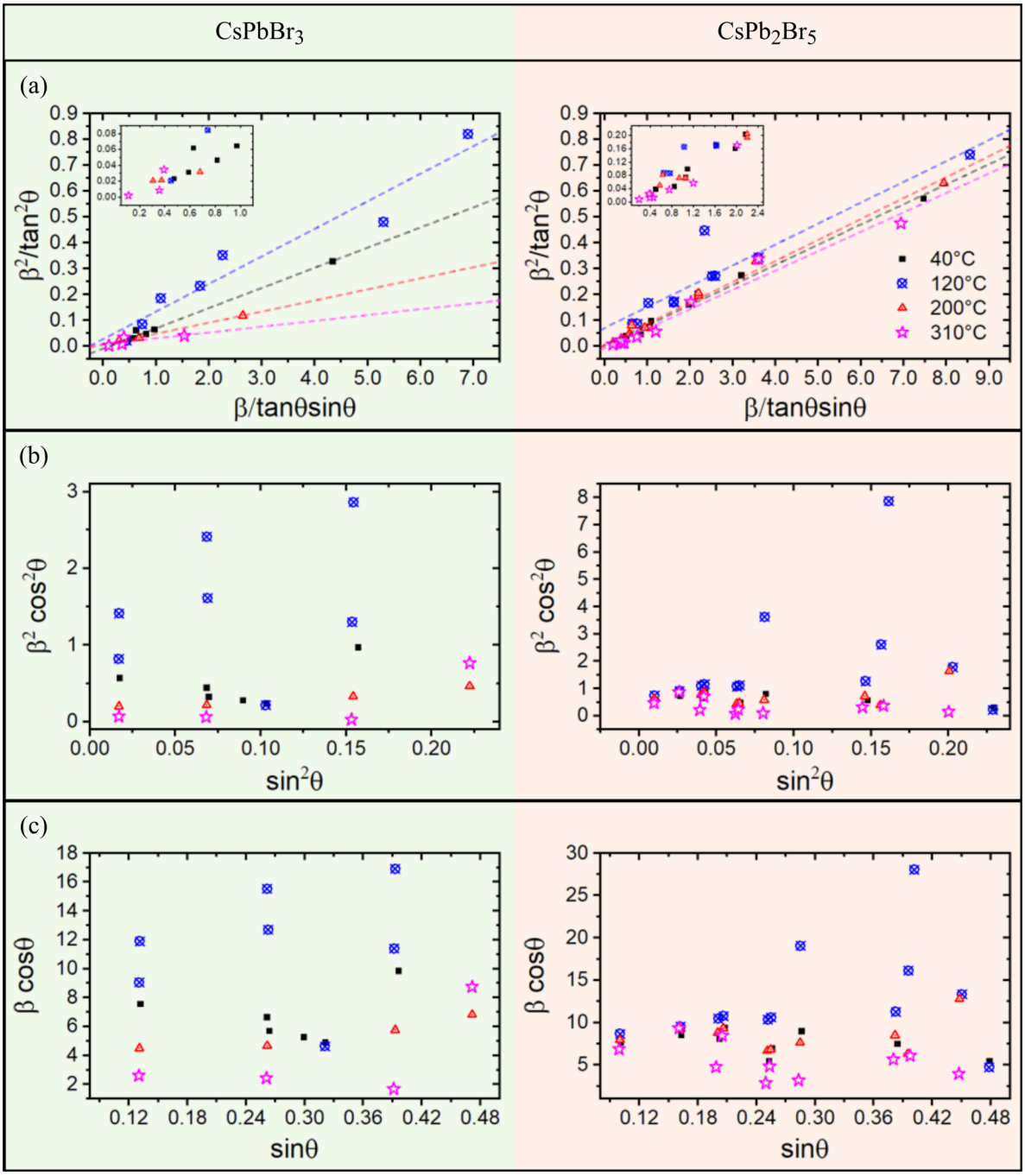

Figure 5.6: Integral breadth evaluation at different temperatures using (a) Cauchy-Gaussian (Equation 5.6), (b) Gaussian-Gaussian (Equation 5.7), and (c) Williamson-Hall (Cauchy-Cauchy, Equation 5.8) approximations for the $CsPbBr_3$ (green background) and $CsPb_2Br_5$ (orange background) phases in the mixed-phase film. The linear fits calculated for the Cauchy-Gaussian approximation are also plotted. Figure reproduced with permission from Caicedo-Dávila et al. J. Phys. Chem. C **2020** 124, 36, 19514 - 19521. Copyright 2020 American Chemical Society [110].

The slope (λ/L) obtained from the fit at each temperature was used to estimate L. Since the film exhibits strong texturing, the estimation of L is not quantitatively accurate. However, since the same set of Bragg peaks were used to construct the integral breadth plots, the trend with temperature holds. In Figure 5.8d the —coherently diffracting— domain size, L, normalized to the maximum measured is plotted as a function of temperature. Clearly, the size of the $CsPb_2Br_5$ domains does not change significantly with temperature. This is in contrast

to the size of the $CsPbBr_3$ domains, which increases with temperature and monotonically after a temperature of 400 K, i.e., when the crystal structure transitions to cubic.

Finally, L was also estimated from the commonly used Scherrer's Equation:

$$L = \frac{0.9\lambda}{\beta \cos\theta_0} \tag{5.9}$$

The domain size (as per Equation 5.9) as a function of temperature is plotted in Figure 5.7. It exhibits a similar trend as the ones estimated using the more sophisticated integral breadth analysis: The size for $CsPb_2Br_5$ varies slightly from 17 to 50 nm, while that of $CsPbBr_3$ increases considerably with temperature from 22 to 200 nm.

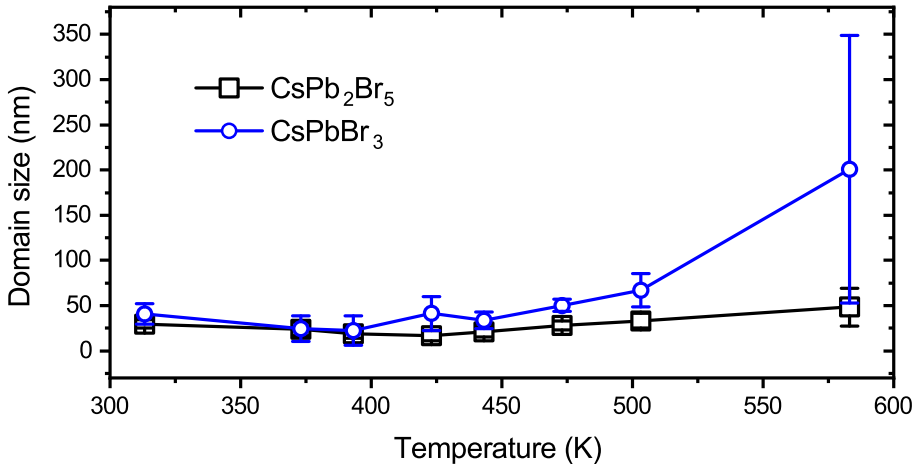

Figure 5.7: Domain size as a function of temperature, estimated using Scherrer's Equation 5.9 for $CsPbBr_3$ and $CsPb_2Br_5$ in the mixed-phase film. Figure reproduced with permission from Caicedo-Dávila et al. J. Phys. Chem. C **2020** 124, 36, 19514 - 19521. Copyright 2020 American Chemical Society [110].

It is important to stress here that the sizes calculated with Equation 5.9 are only a ROUGH ESTIMATION and are only given for comparative purposes. This approximation neglects the peak broadening due to strain, and for very high temperatures the Cauchy portion of the Bragg peak profile only differs marginally from the instrumental Cauchy profile, thus, domain sizes are above the resolution limit of the diffractometer, which restricts the detectable domain size to about ≤ 120 nm. This is clearly visible in the large error bars at higher temperatures in Figure 5.7.

An important feature to notice is that, although both $I(CsPbBr_3)/I(CsPb_2Br_5)$ and L increase with temperature, their behavior between 400 and 500 K differs considerably. While the domain size increases monotonically over this range of temperature, $I(CsPbBr_3)/I(CsPb_2Br_5)$ does not change considerably and exhibits a sudden increase only when the temperature is elevated to 583 K. This indicates that until the temperature reaches 583 K, the volume fraction of $CsPbBr_3$ — with respect to that of the $CsPb_2Br_5$ — does not increase, but only the crystallinity is enhanced with temperature.

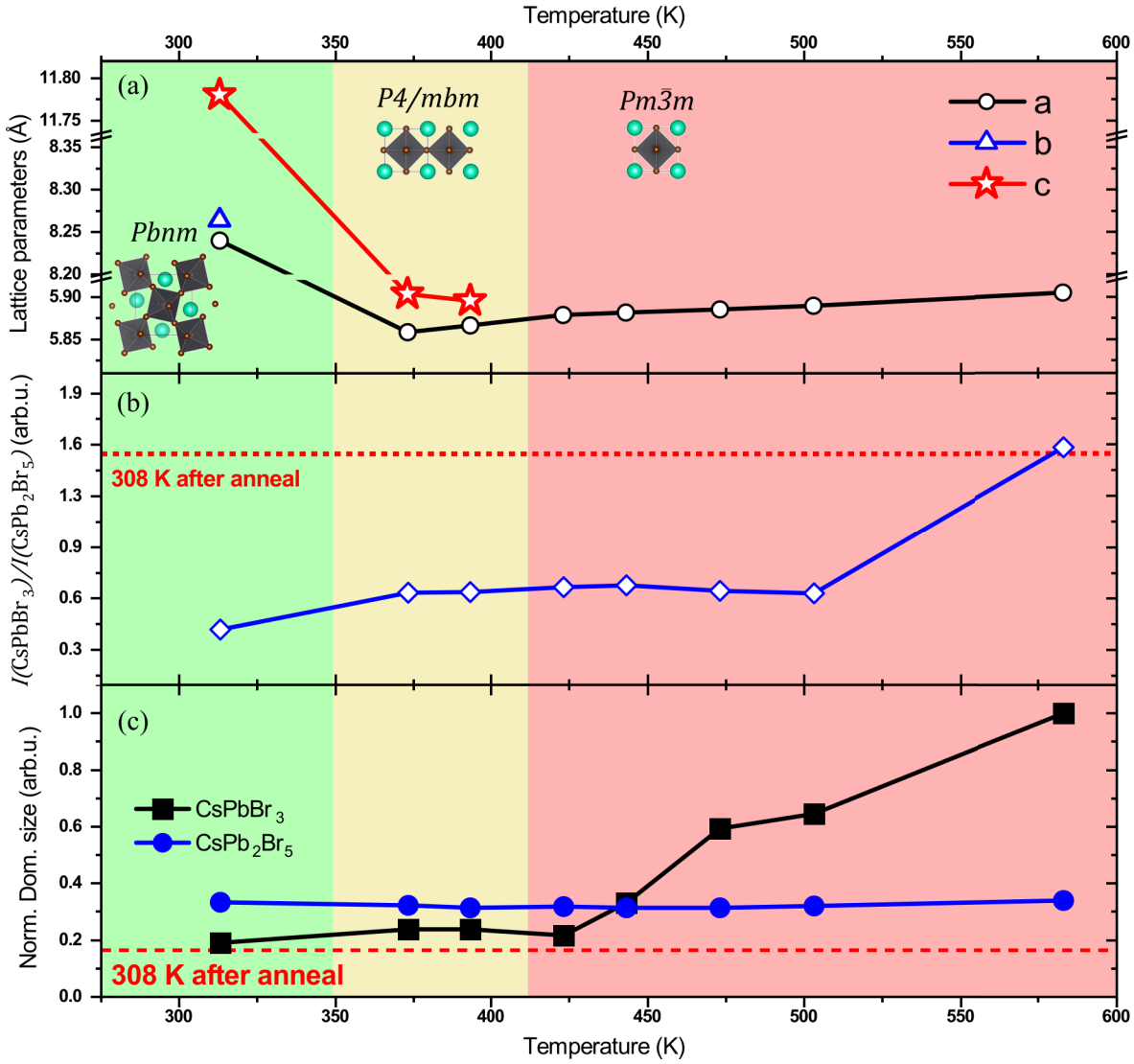

Figure 5.8: Results of the evaluation of the in-situ XRD: (a)) Lattice parameters as a function of the temperature obtained using Le Bail refinement. The crystal structures of the orthorhombic (*Pbnm*), tetragonal (*P*4/*mbm*) and cubic (*Pm*$\bar{3}$*m*) phases of $CsPbBr_3$ are also shown. (b) $I(CsPbBr_3)/I(CsPb_2Br_5)$ ratio of integral intensities and (c) domain size of the perovskite $CsPbBr_3$ (black) and the Pb-rich $CsPb_2Br_5$ (blue) in the mixed-phase film as a function of temperature. The dotted red line shows the value of $I(CsPbBr_3)/I(CsPb_2Br_5)$ measured at 308 K after the film was annealed (see Figure 5.9). The areas shaded in green, yellow and red are the temperature ranges for the *Pbnm*, *P*4/*mbm* and *Pm*$\bar{3}$*m*.

5.2.3 Studying the reversibility of the changes

Separate XRD experiments were performed to study how reversible are the changes in the structure and phases induced by the elevated temperature annealing. The film was annealed at 583 K and the diffractogram at elevated temperature was measured. After that, the sample was left cool down to 308 K and the post-annealing diffractogram was measured again. The results are summarized in Figure 5.9b, while Figure 5.9a shows the evolution of the peaks while the temperature is increased. Notice how the peak intensity does not reduce back to the initial value after it was annealed.

A similar analysis as those described in Section 5.2.2 was carried out, and it was found that the domain size, estimated from integral breadths, is reversible, the $I(CsPbBr_3)/I(CsPb_2Br_5)$

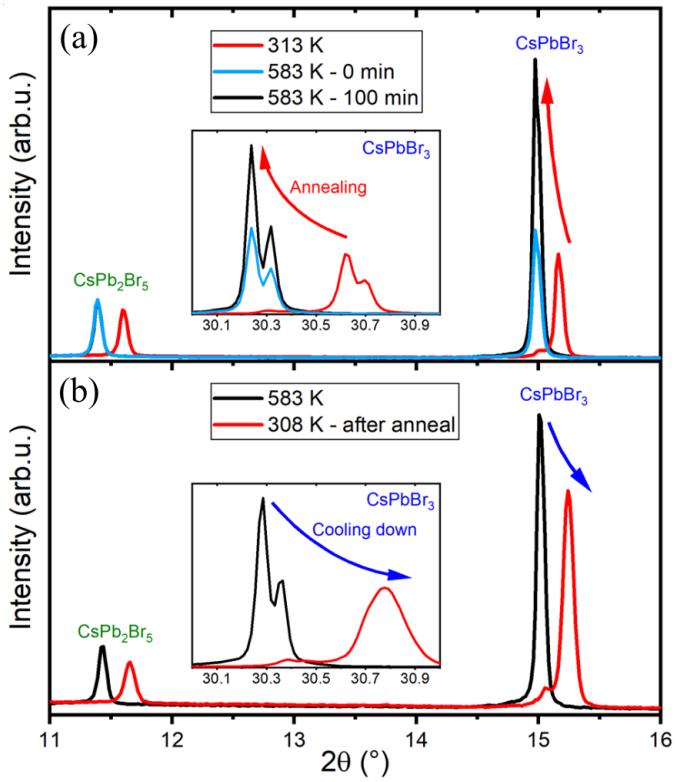

Figure 5.9: Changes in the intensity of the main Bragg reflexes of $CsPb_2Br_5$ and $CsPbBr_3$ (also in the inset) measured during (a) 583 K annealing and (b) at 308 K upon cool-down after annealing. Note that after annealing, the intensity for the 004 reflection of $CsPb_2Br_5$ is reduced, while the ones for $CsPbBr_3$ effectively increase, indicating a non-reversible increase of the volume fraction of $CsPbBr_3$. Figure reproduced with permission from Caicedo-Dávila et al. J. Phys. Chem. C **2020** 124, 36, 19514 - 19521. Copyright 2020 American Chemical Society [110].

is not, and even after cooling down, it remains very close to the final value at 583 K (see horizontal dashed lines in Figure 5.8). This indicates that the increase in $CsPbBr_3$ volume fraction induced by temperature is irreversible. The apparent reversibility of the estimated domain size requires a more delicate analysis. Since the $CsPbBr_3$ goes through crystal phase transition with temperature to a more symmetric (cubic) phase, which is not stable at room temperature, two explanations are possible:

- A reconstructive phase transition to tetragonal ($P4/mbm$) and then orthorhombic ($Pbnm$) could induce a reduction of the coherently diffracting domains. This would explain why the crystallinity reduces back.
- It is also possible that the peak broadening and intensity reduction upon cooling down is due only to symmetry reduction: The peaks of $Pm\bar{3}m$ at elevated temperature split into those of $P4/mbm$ and $Pbnm$. If the experimental setup used and the analysis are unable to decouple the broadening, the domain size might not be captured accurately.

5.2.4 Temperature-induced phase transformation

Another interesting result from these in-situ experiments that was mentioned in Section 5.2.3 is the fact that the XRD patterns at 583 K also change with time. This is particular for this temperature step and it does not happen at any of the other temperatures, which suggests

that this temperature is triggering a particular slow change in the film. While annealing at 583 K, the intensities of the Bragg peaks associated to the $CsPbBr_3$ phase increase with time, while the peaks associated to the $CsPb_2Br_5$ phase slightly decrease, as shown by the 004 ($CsPb_2Br_5$) and 200 ($CsPbBr_3$) reflections, plotted as contour maps as a function of time in Figure 5.10. For all the peaks, there is no additional change in peak position nor in peak shape, which suggest that neither thermal expansion nor structural changes are taking place. The six patterns measured at 583 K were also evaluated using the same methods described in Section 5.2.2 and it was found once more, that the domain size, as estimated from integral breadth evaluation increases for $CsPbBr_3$, but remains almost unchanged for $CsPb_2Br_5$ (Figure 5.10d).

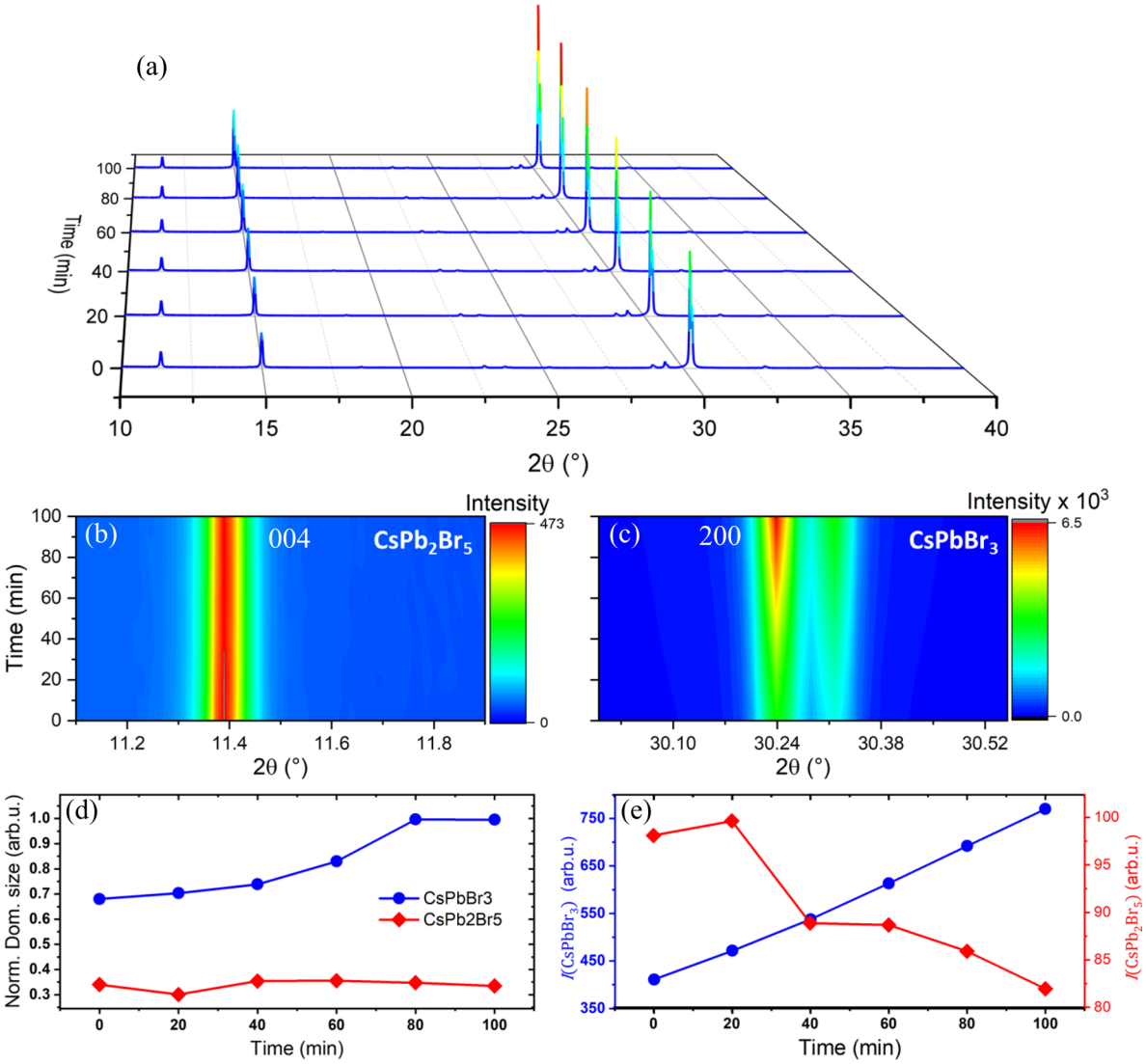

Figure 5.10: (a) In-situ XRD patterns as a function of time, measured on the mixed-phase film while annealing at 583 K. The intensity in the patterns is color-coded to improve visibility. Contour maps showing the time evolution of (b) the 002 peak of $CsPb_2Br_5$ —which intensity slightly decreases with time— and (c) the 200 (cubic) peak of $CsPbBr_3$ —which intensity increases. The time evolution of (b) the domain size, and (c) integral intensities of $CsPbBr_3$ ($I(CsPbBr_3)$ in blue) and $CsPb_2Br_5$ ($I(CsPb_2Br_5)$ in red). Figure reproduced with permission from Caicedo-Dávila et al. J. Phys. Chem. C **2020** 124, 36, 19514 - 19521. Copyright 2020 American Chemical Society [110].

In contrast, as shown in Figure 5.10e, the integral intensity of the peaks associated to $CsPbBr_3$ increases with time during the 583 K annealing, while that associated to $CsPb_2Br_5$ decreases. $I(CsPbBr_3)$ and $I(CsPb_2Br_5)$ were plotted separately in the Figure to show the inverse behaviors appropriately.

These results indicate that at 583 K there is a slow increase in domain size and volume fraction of the perovskite phase, $CsPbBr_3$, and at the same time, there is a decrease in the volume fraction of the Pb-rich phase $CsPb_2Br_5$. This leads to the conclusion that, as already suggested by Tenailleau et al. [24], the $CsPb_2Br_5$ transforms into $CsPbBr_3$. Furthermore, the experimental data presented here suggest that this transformation occurs only at elevated temperatures and is a slow process (minutes timescale).

If the Pb-rich phase is indeed transforming into the perovskite, the reaction

$$CsPb_2Br_5 \longrightarrow CsPbBr_3 + PbBr_2$$

has to be balanced by the excess of $PbBr_2$ somewhere in the film. The in-situ XRD measurements do not provide any evidence of $PbBr_2$ in the film. However, the $CsPb_2Br_5$ volume fraction reduction is very small, which might imply that the excess $PbBr_2$ is also small. Ex-situ GIXRD measurements were performed in order to detect possible phases in small volume fractions present in the film after annealing. The diffractogram in Figure 5.11a exhibits some extra Bragg peaks that can be associated to the 230, 140, 321, 222, 132 and 341 reflections of $PbBr_2$. Additionally, EDX maps measured on the cross section of the film after annealing revealed that not only the Cs content in the bottom layer increases considerably after annealing, but also there is a considerable increase of Pb and Br towards the surface of the film (see the elemental maps in Figure 5.11). Owing to the resolution of the EDX experiment (a few 10 nm) and the small volume fraction of the $PbBr_2$ phase, a quantitative composition cannot be estimated. However, the fraction of Pb and Br net counts, normalized to the total counts ([Cs] + [Pb] + [Br]) as a function of the cross-sectional position, as in Figure 5.11c, is a good indication of the changes in the composition. This plot shows the relative amount of $PbBr_2$ content at different depths along the cross section. Both, the EDX and the GIXRD results, confirm the presence of $PbBr_2$ as a result of the annealing-induced reaction.

5.3 Microscopic origins of annealing-induced changes

It was found that the annealing-induced phase transformation yields a film with a larger $CsPbBr_3$ volume fraction. However, as discussed in Section 5.1.2, this same film exhibits a considerable decrease in the PLQY and in the intensity of the 2.35 eV emission peak. This finding is explained by a shorter lifetime after annealing, which in turn can be explained by a higher defect concentration. However, the origin of a low-energy band in the PL spectrum after annealing (Figure 5.2a) is still unclear. Figure 5.12 summarizes the results of the microscopic characterization of the cross section of the film as deposited and after annealing at 583 K. As discussed in Section 4.3.4, the CL spectrum of the film as deposited exhibits emission peaks at two energies: at the 2.35 eV, characteristic of the perovskite, and a broad band at $\sim$ 1.8 eV, which is attributed to transitions between defect levels. Cross-sectional CL confirmed that the 2.35 eV emission stems from the bottom layer of the film, and that when this layer was excited, no low-energy signal was measured. On the other hand, the 1.8 eV

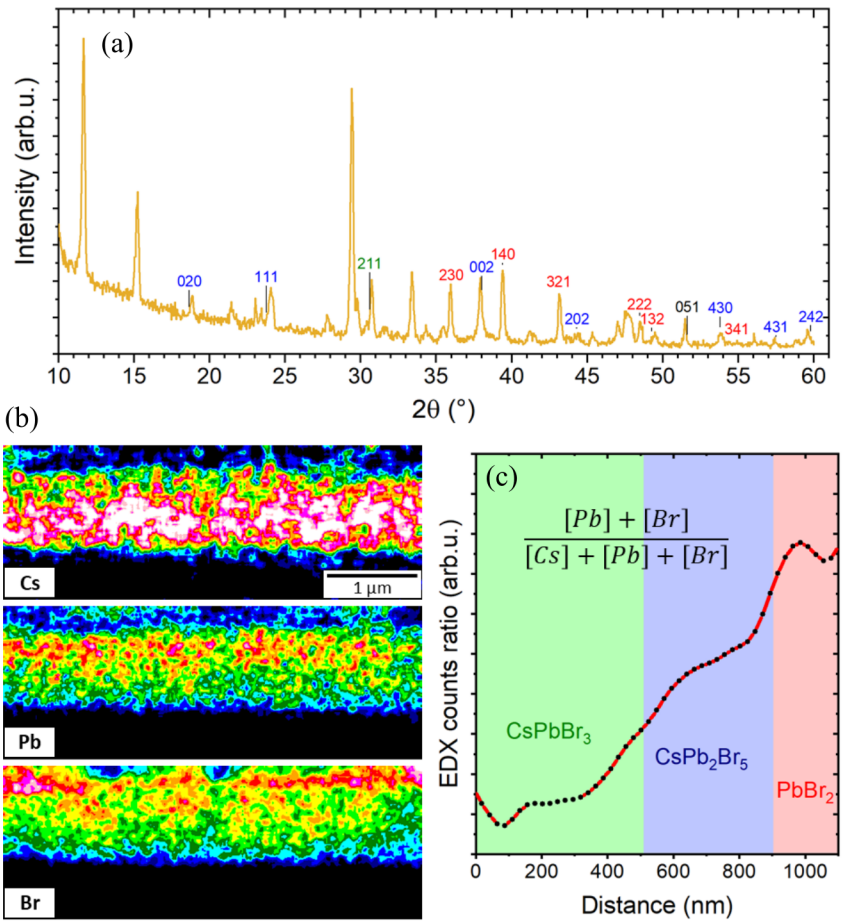

Figure 5.11: (a) GIXRD pattern of the mixed film, acquired after annealing. The reflections identified as $PbBr_2$ are shown in the plot. Reflections in blue coincide with reflections of $CsPb_2Br_5$, and those in green coincides with a $CsPbBr_3$ Bragg peak. The reflections in red are new ones, not observed in Bragg-Brentano configuration. (b) Cross-sectional EDX composition maps of Cs, Pb and Br showing the enhanced signal of Pb and Br towards the surface. (c) $([Pb]+[Br])/([Cs]+[Pb]+[Br])$ EDX counts ratio, showing the increased concentration of $PbBr_2$ towards the surface of the film. The position of the different phases are shown in colored areas. Figure reproduced with permission from Caicedo-Dávila et al. J. Phys. Chem. C **2020** 124, 36, 19514 - 19521. Copyright 2020 American Chemical Society [110].

signal was dominant when the surface layer was excited (see Figure 4.14). A map of dominant emission was constructed by superimposing the CL emission maps acquired using a slight variation of the setup described in Section 4.3. In this setup, the light was focused outside the microscope through a band-pass filter (bandwidth 50 nm) into a PMT (Thorlabs, PMT1001). This setup allows rapid acquisition, reducing the electron dose and the damage to the sample, at the expense of spectral resolution. The filters used to measure each emission were 550 nm ($\sim$ 2.26 eV) and 700 nm ($\sim$ 1.77 eV).

The CL emission maps, together with EDX Cs elemental maps and CL spectra of the different layers acquired on the cross section of the film as-deposited and after annealing are shown in Figures 5.12a and b. After annealing, the thickness of the $CsPbBr_3$ layer increases, which agrees well with the results of the in-situ XRD experiments. The emission distribution on the cross section does not change after annealing, i.e., the low energy emission band is still visible only when exciting the $CsPb_2Br_5$ top layer, and the green emission is measured when exciting the $CsPbBr_3$ and the $CsPb_2Br_5/CsPbBr_3$ interface. An important difference

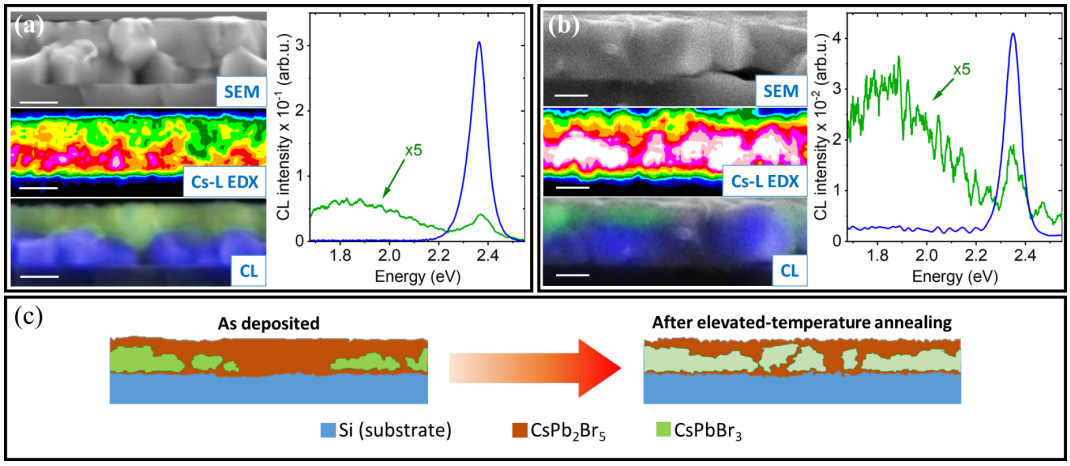

Figure 5.12: SEM images, Cs distribution (EDX), and luminescence (CL) maps on the cross section of the mixed-phase film (a) as deposited, and (b) after annealing. The Cs distribution —coupled to the correlated green luminescence— is representative of the different phases: $CsPbBr_3$ exhibits higher Cs content. After annealing, the thickness of the Cs-rich layer increases. (c) Schematic representation of the phase distribution and the change with the temperature treatment. All scale bars are 500 nm. Figure reproduced with permission from Caicedo-Dávila et al. J. Phys. Chem. C **2020** 124, 36, 19514 - 19521. Copyright 2020 American Chemical Society [110].

between the CL of the film as-deposited and after annealing is the intensity of the 1.8 eV band, relative to that of the 2.35 eV. After annealing, this intensity increases considerably. The overall CL intensity decreases by a factor of about 6. These results suggest that after annealing recombination via deep defects, which might be partially associated to the 1.8 eV emission, quenches the green luminescence and reduces the PLQY of the film, regardless of the larger fraction of $CsPbBr_3$.

It is worth discussing the origins of the deep defects responsible for the 1.8 eV band. Nitsch et al. [29] measured two or three well-defined shallow defect states in $CsPbBr_3$ with transition energies 100 to 200 meV below the free exciton transition energy at ∼2.16 to 2.26 eV, in contrast to the 500 meV energy difference reported in the present work for the low-energy band. Furthermore, the 1.8 eV emission was not detected when exciting the $CsPbBr_3$ part of the film in cross-sectional CL experiments. Thus, if there are any deep defects causing recombination in the $CsPbBr_3$, they do not have an associated radiative transition or lie beyond the measurement range. Therefore, the low energy band cannot be assigned to defects inside $CsPbBr_3$.

In contrast, the origin of the 1.8 eV emission located at the surface, indicates that the $CsPb_2Br_5$ has a high defect concentration, whose radiative transition can be measured. Additionally, recent DFT calculations of various point defects $CsPb_2Br_5$ by Yin et al. [68] show that the defect levels lie in deep inside the band gap. The difference in position of some these defect levels — e.g., Pb vacancies and Pb-Br antisites — is ∼ 1.9 eV, which is in reasonable agreement with the observations reported here. This leads to the conclusion that thermal expansion and phase transformation increase the defect concentration not only in the $CsPb_2Br_5$, but also at the interface to the $CsPbBr_3$. If the defect concentration is increased at the $CsPb_2Br_5/CsPbBr_3$ interface, photogenerated carriers can diffuse and recombine via such defects (schematically shown in Figure 5.13). This can explain the 1.8 eV band in the PL spectra after annealing, and is partially responsible for the quenching of the green luminescence.

5.4 Summary and discussion

In summary in this Chapter the temperature-induced phase transformation $CsPb_2Br_5 \longrightarrow CsPbBr_3 + PbBr_2$ was investigated by means of in-situ XRD on coevaporated Cs–Pb–Br films. This process has been investigated by Tenailleau et al. [24] for nanoparticles and thin films. Later, Maity and Pradhan [25] also reported the change of the optical absorption upon phase transformation. However, in either of those publications the influence of the phase transformation on the luminescence yield was established. Therefore, a PL and correlative microscopy investigation of the film as deposited and after annealing is presented here, in order to understand the effect of post-deposition annealing and phase transformation on the luminescence of mixed $CsPbBr_3/CsPb_2Br_5$ films

In-situ XRD shows that annealing up to 500 K improves the crystallinity of the $CsPbBr_3$ part of the film with no detectable phase transformation. However, annealing at a higher temperature of 583 K, irreversibly increases the volume fraction of $CsPbBr_3$ by transforming $CsPb_2Br_5$ to $CsPbBr_3 + PbBr_2$. The film with larger perovskite volume fraction exhibits a lower green luminescence; a broad, low-energy band appears at ~ 1.8 eV, and the minority carrier lifetime decreases over an order of magnitude; all of which suggest an increased number of trap states that quench the $CsPbBr_3$ green luminescence. This was confirmed by correlative microscopic analysis, which suggests that after annealing, the green PL quenching is caused partially by deep defect recombination, associated with the observed 1.8 eV. We associate this band to defect emission when the $CsPb_2Br_5$ part of the film is excited. The proposed model for recombination of the film as-deposited and after annealing is shown in Figure 5.13.

It has been suggested that $CsPb_2Br_5$ can passivate defects at the surface of $CsPbBr_3$ films reducing nonradiative recombination [39, 82, 84]. The results presented here cannot confirm this hypothesis, and on the contrary, the microscopic evidence shows that $CsPb_2Br_5$ might quench the green luminescence of $CsPbBr_3$ when the mixed-phase film is subjected to recrystallization and phase transformation caused by elevated temperature annealing.

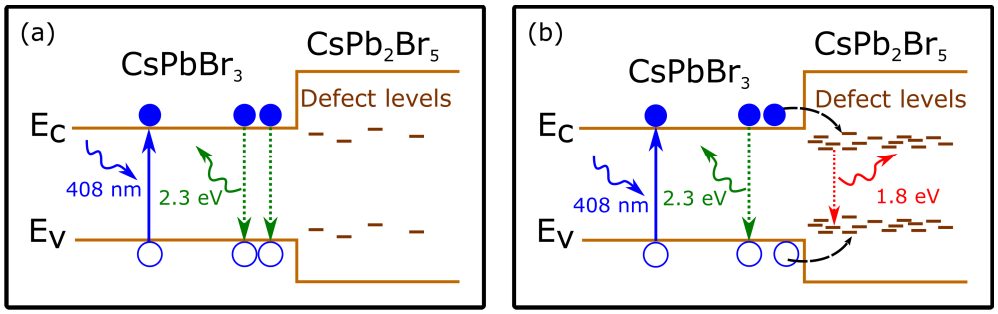

Figure 5.13: Schematic of the proposed recombination processes that cause the different emission bands in the $CsPbBr_3/CsPb_2Br_5$ coevaporated film (a) as-deposited and (b) after annealing. The optical excitation using a 408 nm laser is shown as a full-line arrow, while radiative transitions that contribute to emission are shown as dotted-line arrows. Non-radiative processes are shown in dashed, black arrows. In the film as-deposited, the relatively low density of radiative defects at the $CsPb_2Br_5/CsPbBr_3$ interface results in undetectable low-energy emission. Thermal expansion and phase transformation induced by annealing increase the defect density, increasing the low-energy band in the PL spectrum and partially quenching the green emission.

6

Embbeded perovskite and confinement effects in mixed-phase Cs-Pb-Br materials

Chapter 5 described the details of the $CsPb_2Br_5 \longrightarrow CsPbBr_3$ phase transformation and its influence on the photoluminescence of the mixed phase film. In the present Chapter, the results of the investigation of the luminescence on a different type of mixed-phase material are given. In the first Section 6.1, the synthesis of $CsPbBr_3$ and $CsPb_2Br_5$ powders, as well as a Cs_4PbBr_6 single crystal is described. Section 6.2 describes the characterization by means of photoluminescence (PL) and cathodoluminescence (CL) of the bulk $CsPbBr_3$ powder. The different identified recombination mechanisms are described and established as basis for the analysis of the mixed-phase films. In Section 6.3, the luminescence of the $CsPb_2Br_5$ and Cs_4PbBr_6 is studied, and CL reveals that the origin of the green luminescence of the wide-gap materials stems from very localized $CsPbBr_3$ emitters within the solid matrix. Differences in the luminescence intensities are described and explained as a result of the confinement effects. However, differences in emission energy cannot be easily explained. Thus, in Section 6.4 a theoretical model for the emission of confined $CsPbBr_3$ is used to describe the unexplained results and to address some of the open questions about the emission of $CsPbBr_3$ nanocrystals embedded into Cs_4PbBr_6 or $CsPb_2Br_5$.

6.1 Synthesis of the Cs–Pb–Br ternary phases

$CsPbBr_3$ was synthesized from an equimolar mixture of CsBr (99.99 % from Ossila) and $PbBr_2$ (98 %, extra pure, from Arcos Organics) in dimethylformamide (DMF, 99.8 %, Roth) and left to stir overnight at 60 °C followed by evaporation of the solvent at 85 °C and annealing at 140 °C for 1 h. The resulting material is a fine, bright-orange powder (see Figure 6.1b). For the synthesis of $CsPb_2Br_5$ a 1:3 ($CsBr:PbBr_2$) molar ratio was used, followed by the same

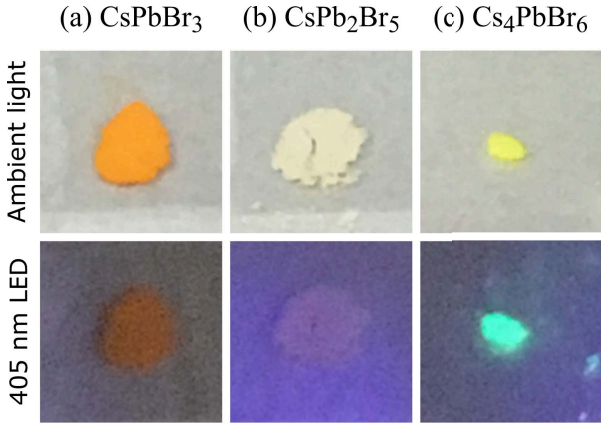

Figure 6.1: Photographs of the $CsPbBr_3$, $CsPb_2Br_5$ and Cs_4PbBr_6 under ambient light and 405 nm LED illumination. Notice the strong green emission of the Cs_4PbBr_6. For the other two phases the emission is not visible.

synthesis procedure as for $CsPbBr_3$. The resulting material is a white powder (see Figure 6.1b)

Cs_4PbBr_6 was synthesized using the anti-solvent method, adapted from the one reported by Cha et al. [66]. A mixture of 0.2554 g (0.2 M) of CsBr (99.99 % from Ossila) and 0.1079 g (0.05 M) $PbBr_2$ (98 %, extra pure, from Arcos Organics) in dimethyl sulfoxid ($\geq$ 99.99 %, Rotisolv, Roth) was dissolved under ultrasonication (T $<$ 40 °C) until no precipitation was observed. The solution was filtered (0.2 µm pore-size syringe filter) and transferred into a 50 ml glass vial and sealed with the cap, which was perforated by a needle to ensure diffusion of the solvent through a small hole. The vials were place into a 250 ml solvent vial with screw cap under dichloromethane ($\geq$ 99.99 %, Rotisolv, Roth) atmosphere. Within few days, yellow crystal seeds were removed from the vials, washed with DMF and dichloromethane (DCM) solution. The crystals are highly green luminescent under blue illumination (see Figure 6.1c). The samples were stored under N_2 to avoid potential degradation by oxygen and humidity.

Special thanks are due to Dr. Frederike Lehmann for the synthesis of the samples of the different ternary phases.

6.2 Luminescence of the $CsPbBr_3$ bulk

6.2.1 PL spectroscopy

The $CsPbBr_3$ powders were characterized by temperature- and intensity-dependent PL spectroscopy, in order to identify the different radiative transitions. Thanks are due to Dr. Sergei Levcenco for performing the PL measurements. At low temperatures (13 to 141 K), a broad band centered at 2.07 eV was measured (see Figure 6.2a). This band vanishes as the temperature increases, suggesting it can be attributed to radiative recombination at deep defects [93]. The band at higher energy was fitted using three Gaussian functions ($R^2 > 0.98$) for the whole temperature range. This allows to decompose the contributions to the PL spectrum, using a model similar to that proposed by Nikl et al. [153] for $CsPbCl_3$. The highest energy subband (2.34 eV at 13 K) can be assigned to the free exciton recombination, the middle subband (2.33 eV at 13 K) to the bound exciton, and the lowest energy subband (2.32 eV at

13 K) to a radiative transition via shallow defect levels. This assignment was considered, in contrast to that proposed by Nitsch et al. [29], since the peak positions of the highest and middle subbands increase with temperature, as expected from excitonic transitions, when the band gap increases and the lattice expands, similar to what was discussed in Section 4.3.4 [67, 141] (see Figure 6.2b). On the other hand, the position of the lowest subband oscillates around 2.3 eV, but it does not increase monotonically with the temperature. At low temperatures ($\sim$ 13 K), the free exciton transition generates a sharp peak that dominates the maximum of the spectrum. At higher temperatures ($>$ 220 K), the peak of the spectrum is dominated by the bound exciton.

Figure 6.2c shows the integrated intensity of the complete spectrum and the contributions of each subband as a function of the temperature. The largest contribution to the luminescence comes from the bound exciton. A similar phenomenon was observed by Nikl et al. [153] for $CsPbCl_3$, which was assigned to energy transfer from the free to the bound excitons at temperatures in the range 20 to 50 K. It is possible that a similar process occurs in $CsPbBr_3$, but we were unable to detect it. At higher temperatures all the subbands are quenched, but the middle and lowest energy subbands are the ones that contribute the most to the room temperature PL spectrum (see inset in Figure 6.2c).

It is possible to fit the PL integrated intensities of Figure 6.2c using an Arrhenius equation. A single-term Arrhenius equation is conventionally used to estimate the exciton binding energy from temperature-dependent PL [68, 76, 146]. However, care is advised, since the contribution of traps must also be taken into account. Here, the PL intensity was fitted to a two-term Arrhenius equation, using the range from 60 K onwards, since it has been shown that for lower temperatures, the estimated activation energies are not representative of true energy levels difference [154]. Fitting the data using a three-term Arrhenius equation ends up with two of the three estimated activation energies being equal. The fitted activation energies were $E_1 \approx 33 \pm 4$ meV and $E_2 \approx 180 \pm 30$ meV. The phenomenological fitting to the Arrhenius function does not allow for assigning the quenching mechanism directly. However, as pointed out by Wolf and Lee [155], it is reasonable to assign E_1 to the exciton binding energy, and E_2 to defects because of the high activation energy. The corresponding coefficients, $A_1 \approx 60$ and $A_2 \approx 10000$ suggest that the quenching is dominated by defects.

The dominant quenching mechanism can be studied, as described in Section 3.2.2, by means of intensity-dependent PL spectroscopy. The PL spectrum of the $CsPbBr_3$ powder was measured using different excitation power at 13 K, as shown in Figure 6.3a. The integrated PL intensity was plotted on a log-log scale, and the slope of the linear fit was estimated. This slope is equivalent to the exponent m in equation 3.3. The value of $m \approx 2$ suggests again that nonradiative recombination is dominant in the bulk $CsPbBr_3$.

6.2.2 CL spectroscopy on $CsPbBr_3$ powder

From the assignment made to the different subbands in PL, it is interesting to note that at room temperature, a shallow defect band is still detectable. Nikl et al. [153] assigned these defect states at the more defected surface of the $CsPbCl_3$ material using one- and two-photon excitation. Another way to determine the depth at which the luminescence originates in a very localized manner is using acceleration-voltage- (or beam-energy-) dependent CL spectroscopy.

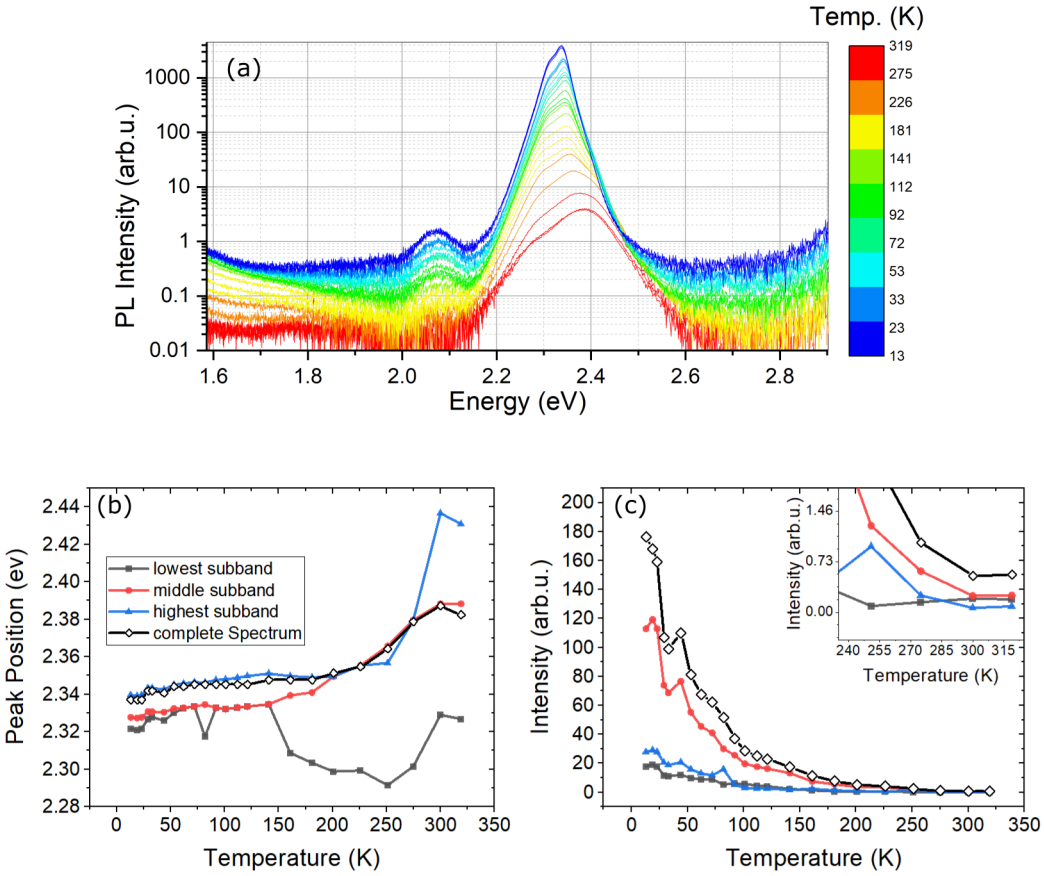

Figure 6.2: (a) Temperature dependent PL spectra of the $CsPbBr_3$ powder. As the temperature is increased, the intensity of the green luminescence between 2.3 and 2.4 eV decreases. At temperatures below 140 K a defect peak at 2.07 eV is identified. (b) Energy position of the peak of the spectrum, and each subband. (c) integrated PL intensity as a function of the temperature. The integrated intensities and peak positions are depicted using white diamonds for the whole spectrum, while those corresponding to the deconvoluted the highest, middle and lowest energy subbands are depicted with blue triangles, red circles and black squares, respectively

As described by equation 3.4, the penetration depth of the impinging electron beam depends on the density of the material and the beam energy, which in turn is determined by the acceleration voltage. Therefore, it is possible to study the contributions of each recombination path at room temperature by measuring the CL spectrum of a flat surface (to avoid artifacts due to an irregular interaction volume) using different acceleration voltages, deconvoluting the resulting spectrum and analyzing the contributions of each recombination path, as assigned in section 6.2.1.

A flat region (see Figures 6.4a and b) was measured using various acceleration voltages in the range of 3.5 to 15 kV. The measured PL spectra were fitted using two Gaussian functions, as shown in Figure 6.4c. The integrated intensities for the low- and high- energy subbands — $I_{2.3}$ and $I_{2.4}$ — were calculated as the area under each Gaussian peak. The spectra exhibit different intensities of $I_{2.3}$ and $I_{2.4}$ at different acceleration voltages (see Figure 6.4c). Since the emission intensity also depends on the acceleration voltage (as per Equation A.1), it is more appropriate to use the ratio between intensities of the subbands, $I_{2.3}/I_{2.4}$ as a metric of the contribution of the low-energy subband, i.e., the contribution due to defect emission.

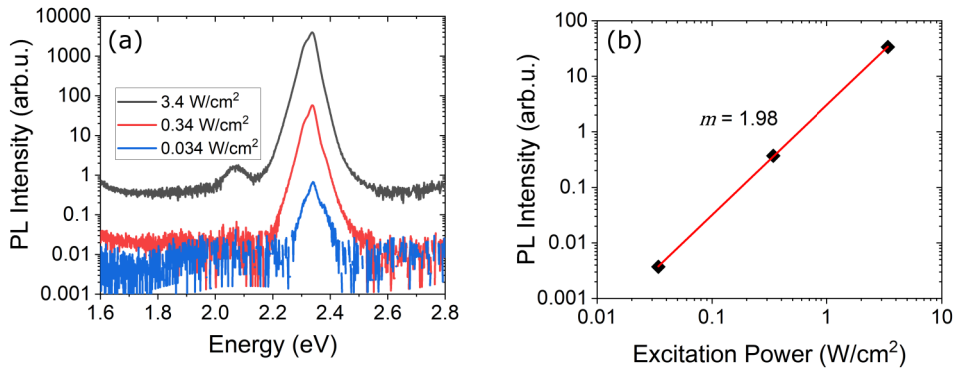

Figure 6.3: (a) Intensity dependent spectra of the $CsPbBr_3$ powder at 13 K. (b) Log-log curve of the PL intensity (integrated from the peaks fitted from spectra in b) as a function of the excitation power. The slope is $m = 1.98 \approx 2$.

Figure 6.4d shows the intensities ratio as a function of the penetration depth calculated using equation 3.4 and the density of $CsPbBr_3$, 4.75 g/cm^3 [156]. It is very interesting to note that only for the lowest acceleration voltage, 3.5 kV — which corresponds with a penetration depth of 75 nm — the ratio is larger than 1, i.e., the contribution of defect mediated transitions is larger than that of the exciton recombination. This confirms that the radiative shallow defect levels are more concentrated towards the surface of the material. This is an important difference from the bulk material in extended $CsPbBr_3$ — such as in the powder studied in this chapter — and the bulk material in thin films, considered in Chapters 4 and 5. For all the other larger acceleration voltages, the ratio lies in the range from 0.6 to 0.7. This results show the difference between the extended bulk material and the thin-film bulk, in which the shallow defect transition was not detected.

6.3 Luminescence of Cs_4PbBr_6 and $CsPb_2Br_5$

6.3.1 PL spectroscopy

Figure 6.5a shows the PL spectra of the Cs_4PbBr_6 and $CsPb_2Br_5$ ternary phases — synthesized as described in Section 6.1 — and the spectrum of $CsPbBr_3$ as reference. The green luminescence in both $CsPb_2Br_5$ and Cs_4PbBr_6 is enhanced, in spite of the fact that both phases exhibit a large band gap energies [19, 30, 52–56, 58]. In the case of $CsPb_2Br_5$, the PL intensity increases almost 1 order of magnitude, while fin the case of Cs_4PbBr_6, the PL intensity increases about 3 orders of magnitude with respect to the PL intensity of the bulk $CsPbBr_3$.

To understand the underlying recombination mechanisms, intensity-dependent PL was measured, in an experiment similar to that performed for the bulk $CsPbBr_3$ (see Figure 6.5b). The fit of the exponent of equation 3.3 yields $m = 1.52$ for the $CsPb_2Br_5$ and $m = 1.19$ for the Cs_4PbBr_6. The direct interpretation of these coefficients is that nonradiative, defect-assisted recombination — dominant in the bulk $CsPbBr_3$ — is quenched, and the role of exciton recombination is enhanced. This quenching is specially strong for the Cs_4PbBr_6, since the m exponent is closer to 1. For $CsPb_2Br_5$ defect-mediated recombination is still important and no contribution dominates over the other. This interpretation is also supported by the

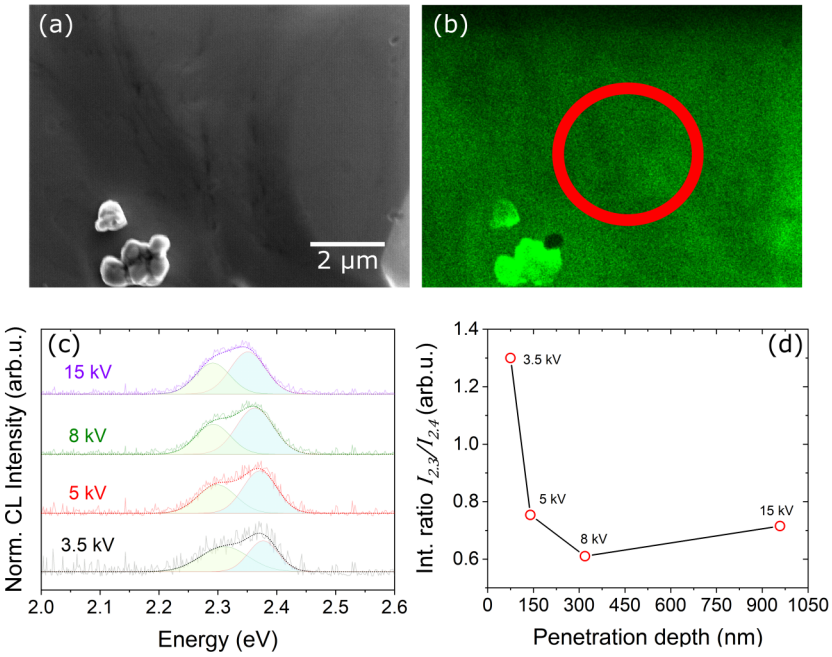

Figure 6.4: (a) SEM image of a flat surface of a grain of $CsPbBr_3$ powder and (b) corresponding CL intensity map: the red circle shows the area from which the CL spectra are extracted. (c) Normalized CL spectra measured using various acceleration voltages, and fitted Gaussian functions for the low- (green-shaded, $I_{2.3}$) and high-energy (blue-shaded, $I_{2.4}$) subbands. (d) Ratio between integrated intensities of the low- and high-energy subbands of the CL spectra. This shows the contribution to the overall spectrum from the shallow defect emission. Note that it is only > 1 for the lowest acceleration voltage with a penetration depth of $\sim 70\,\text{nm}$

measured band around 1.8 eV, which is similar to the band assigned to defects in the mixed phase $CsPbBr_3/CsPb_2Br_5$ film studied in Chapter 5. Similar observations have also been reported by Lee et al. [96] — based in a model proposed by Schmidt, Lischka, and Zulehner [95] — for CdTe with different doping levels, in which the highly-doped n-type CdTe exhibited dominant exciton recombination, while bulk CdTe exhibited mostly defect assisted nonradiative recombination.

But perhaps the most interesting feature of the spectra in Figure 6.5a is the position of the PL peaks. A 50 meV blue shift was measured for the PL peak of Cs_4PbBr_6 with respect to that of $CsPbBr_3$, which is in good agreement with what has been reported in the literature [51]. Assuming that the green luminescence originates in $CsPbBr_3$ embedded nanocrystals, as described in section 2.2 (a direct observation of the inclusions will be detailed in Section 6.3.2), it is possible to use Brus equation (3.6) [111] to estimate the size of the inclusions, considering the values for the effective masses ($m_e^* = 0.15$ and $m_h^* = 0.14$ [157]), and the values for PL peak (2.45 eV for Cs_4PbBr_6 and 2.40 eV for $CsPbBr_3$), the estimated size of the nanocrystal is 10 nm. In the case of $CsPb_2Br_5$, the measured red shift of approximately 40 meV, cannot be correctly described by quantum confinement effects and a particle size cannot be estimated. Thus, a microscopic analysis of the materials can help understand better the origin of the green luminescence.

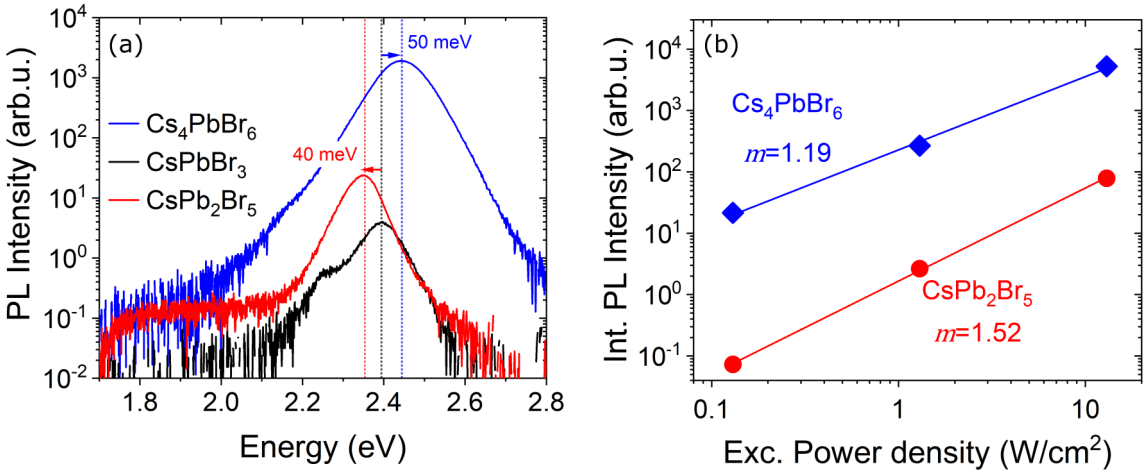

Figure 6.5: (a) PL spectra of the ternary phases of the Cs–Pb–Br system. Notice that the spectrum of the $CsPb_2Br_5$ exhibits a shallow low-energy band, positioned around 1.8 eV. The exciton peaks of the $CsPb_2Br_5$ and Cs_4PbBr_6 phases exhibit a red- and blue shift with respect to the exciton peak of the bulk $CsPbBr_3$. Also, the intensity of the $CsPb_2Br_5$ is one order of magnitude larger that that of the $CsPbBr_3$, and the intensity of Cs_4PbBr_6 is three orders of magnitude larger. (b) Log-log plot of the integrated PL intensity as a function of the excitation power for the $CsPb_2Br_5$ and Cs_4PbBr_6 ternary phases. The slopes from a linear fit are given for each phase (see the text for discussion)

6.3.2 Microscopic investigation of Cs_4PbBr_6 and $CsPb_2Br_5$

6.3.2.1 Cs_4PbBr_6 single crystal

Figure 6.6 shows the initial microscopic characterization of the Cs_4PbBr_6 crystals. Subfigure (a) shows an overview SEM image, and the corresponding panchromatic and 500 nm-filtered CL intensity maps are shown in subfigures (b) and (c). The almost identical CL maps suggest that the crystal exhibits only green luminescence, in the probed spectral range (1.95 to 3.4 eV). Additional CL maps measured using 650 and 700 nm exhibit no detectable signal above the noise level.

The CL map reveals highly luminescent clusters distributed all over the crystal. A magnified SEM image and 500 nm map shows that there is no correlation between the topography of the surface and the luminescent clusters. The CL maps described above were measured at an acceleration voltage of 5 kV and a beam current of 50 pA.

Complementary to the CL maps (see Figure 6.6f), EDX elemental maps were also measured on a region where two luminescent clusters were detected. The clusters exhibit Pb enhancement while Cs and Br are depleted, as shown in the line scans in Figure 6.6g. In order to improve the spatial resolution, the EDX maps were measured at an acceleration voltage of 5 kV. The X-ray fluorescence was measured using a windowless Oxford Instruments Ultim Extreme X-ray detector, which exhibits enhanced sensitivity to low-energy X-ray lines and allows to measure under low voltage conditions. The Cs-M, Pb-M and Br-L X-ray characteristic lines were used for element identification. However, one major drawback of these measurement conditions is that it hinders the quantification of the results. Owing to the low acceleration voltage, the measured Pb-M lines do not allow for appropriate quantification of the composition. Additionally, the Cs-M line lies closely to the O-K line, which complicates the deconvolution

of the elements. Thus, Figure 6.6g shows the normalized line scans and a quantitative change of the composition.

At a first glance, the CL and EDX results suggest that the $CsPbBr_3$ inclusions in Cs_4PbBr_6 are hundreds of nm in size. However, it is important to note that, as described in Section 3.3.3.1, CL emission depends on carrier diffusion and the acceleration voltage. In high injection conditions, the role of the carrier diffusion is not dominant, while that of the acceleration voltage is. Therefore, to improve the resolution of the measured PL maps, it is important to measure with a lower acceleration voltage. Figure 6.7 shows the SEM image, and CL maps using 3.5 and 5 kV acceleration voltage. Measuring at 3.5 kV reveals that each of the luminescent spots exhibits cluster-like features. This suggests that the luminescent spots are not a single emitter, but a cluster of $CsPbBr_3$ nanocrystals, which can explain the broad PL emission in Figure 6.5a, as a broadening caused by the ensemble average of the emission of nanocrystals with various sizes. Estimating the size of individual nanocrystals from the CL experiments presented here is not possible, since considering the density of Cs_4PbBr_6, 4.29 g/cm^3 [158], and equation 3.4, the best achievable resolution — in order to have measurable CL signal — is around 80 nm. However, the PL spectra of individual clusters has a maximum in the range from 2.44 to 2.47 eV, which agrees well with the PL results of Figure 6.5a, and with results from the literature on a similar material, synthesized by mechanical grinding [147].

6.3.2.2 $CsPb_2Br_5$ powder

Figure 6.8a shows an overview image of the $CsPb_2Br_5$ powder, and Figure 6.8b the corresponding CL intensity map, filtered at 550 nm. In contrast to the Cs_4PbBr_6, the $CsPb_2Br_5$ powder sample exhibits only a few luminescent spots. Some of the luminescent regions are $CsPbBr_3$ residues from the synthesis process. However, some very bright luminescent spots exhibit no correlation with the topography. Figures 6.8d and e depict a large magnification SEM image and the corresponding CL intensity map. In the CL map a very high luminescent spot was detected, which is uncorrelated to the topography of the surface. This spot exhibits a luminescence 3 times higher than the green-emitting regions around it, and the CL peak distribution maps in Figures 6.8f and h, confirm that it emits at an energy higher than that of the surrounding emitters. The CL spectra of the the high-luminescent spot (1), of a non luminescent region of the matrix (2) and a region with low green luminescence (3) are shown in Figure 6.8g. Region (1) emits at a higher energy ($\sim$ 20 meV higher) than the surrounding emitting areas, represented by the spectrum of region (3). Region (2) is not luminescent but exhibits a broad band at lower energies, in agreement with the PL spectrum in Figure 6.5a, and the band associated with $CsPb_2Br_5$ defects discussed in Chapter 5. This low-energy defect band is almost evenly distributed over the matrix $CsPb_2Br_5$, as shown in the peak position map in Figure 6.8f.

The highly luminescent spots, which exhibit a slight blue shift with respect to the large $CsPbBr_3$ domains, are consistent with confined $CsPbBr_3$. However, the measured blue shift is so small, that according to the Brus equation 3.6 the size of the inclusion is $\sim$ 20 nm which is way above the exciton Bohr diameter reported for $CsPbBr_3$ of $\sim$ 7 nm [157]. These inconsistencies will be addressed from a theoretical perspective in Section 6.4, where the effects of potential and dielectric confinement will be discussed.

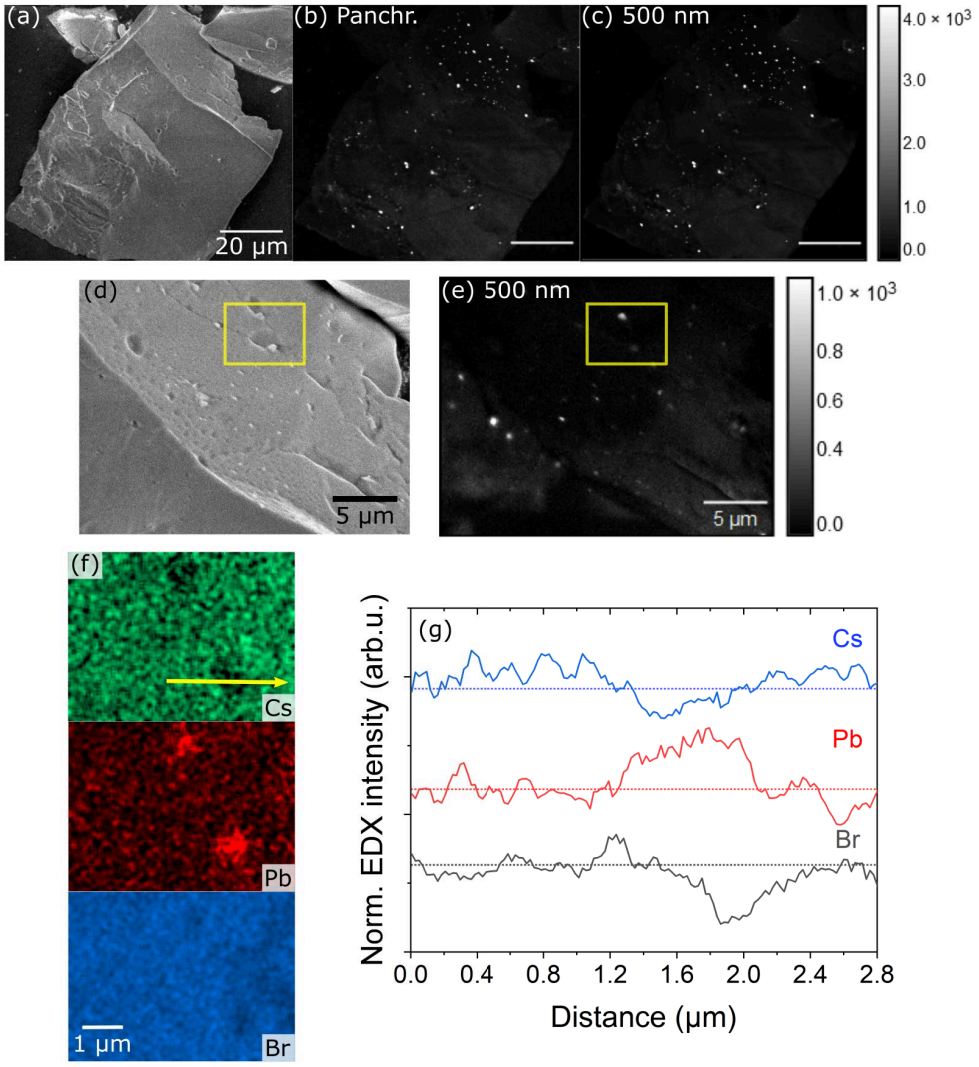

Figure 6.6: (a) SEM image of a Cs_4PbBr_6 crystal piece and the corresponding (b) panchromatic and (c) 500 nm band-pass filtered CL intensity maps. The green luminescence (sharp around 500 nm) stems mostly from clusters embedded in the crystal. (d) Magnified SEM image and the corresponding (e) 500 nm CL intensity map. (f) EDX maps and (g) normalized line-scans — along the yellow line — of a magnified region, shown in the yellow square in (d) and (e). There is a clear enrichment of Pb and depletion of Cs and Br correlated with the high green luminescent clusters, which suggests that the luminescence stems from $CsPbBr_3$ inclusions

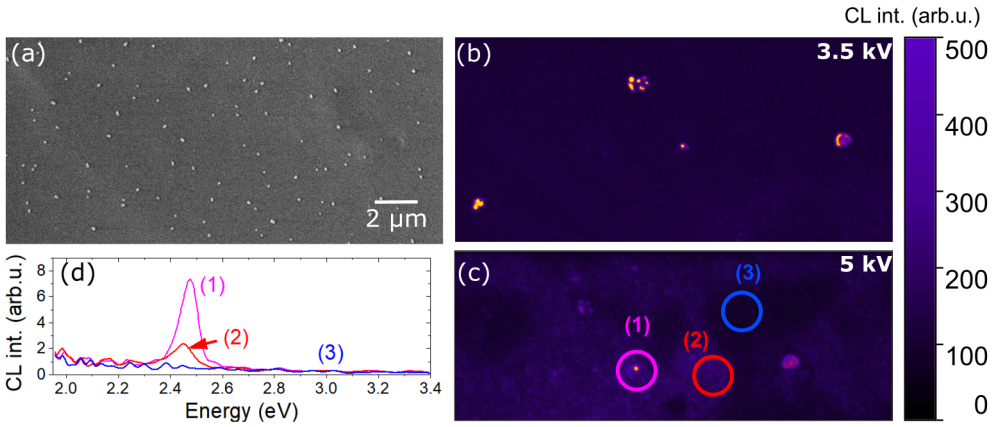

Figure 6.7: (a) SEM image of a flat surface of the Cs_4PbBr_6 crystal and corresponding 500 nm CL intensity maps measured using an acceleration voltage of (b) 3.5 kV and (c) 5 kV. The individual inclusions can be identified when measuring using a lower acceleration voltage. (d) CL spectra of different areas marked on the CL map in (c). A high intensity CL peak at 2.45 eV was measured at the inclusions — spectrum (1) — while no peak was measured on the matrix crystal — spectrum (3). A low intensity peak was measured at a matrix site, only with 5 kV acceleration voltage, which suggests that it is excited from a deeper inclusion.

6.4 Modeling the effects of dielectric mismatch in mixed-phase materials

In order to understand the effect of confinement of $CsPbBr_3$ in both Cs_4PbBr_6 and $CsPb_2Br_5$ on the measured luminescence, it is important to consider an appropriate theoretical model. This section explains two different models that describe the optical properties, considering the effect of quantum and dielectric confinement in mixed-phase Cs–Pb–Br materials.

6.4.1 Emission energy as a function of nanocrystal size

The simplest model to describe the effects of nanocrystal size and in a simple way the electron-hole correlation is the Brus equation (3.6). In order to analyze the limitations of this model, Figure 6.9 shows the dependence of the shift in the emission energy with the size and the effective dielectric constant for a $CsPbBr_3$ nanocrystal confined in an infinite potential. The calculated exciton binding energy increases with decreasing effective dielectric constant, because of the penetration of the electric force lines between electron and hole in the surrounding medium with a smaller dielectric constant. As shown in Figure 6.9a, in the strong confinement regime — consider a Bohr diameter for $CsPbBr_3$ of ~ 7 nm [157] — the effect of the wave function confinement in the infinite potential well, dominates the changes in the emission energy, yielding an overall blue shift of the emission. However, for moderate and weak confinement regimes, dielectric confinement can compensate and even overcome the quantum confinement effects, reducing the observed blue shift, or even inducing a red shift of the emission peak.

The model behind the Brus equation 3.6 includes some important assumptions: the dielectric effects are considered only as a correction of the quantum confinement effects. This model also does not consider the possible changes to the dielectric confinement with the size of the nanocrystal, and the exciton binding energy is assumed to be only a function of the

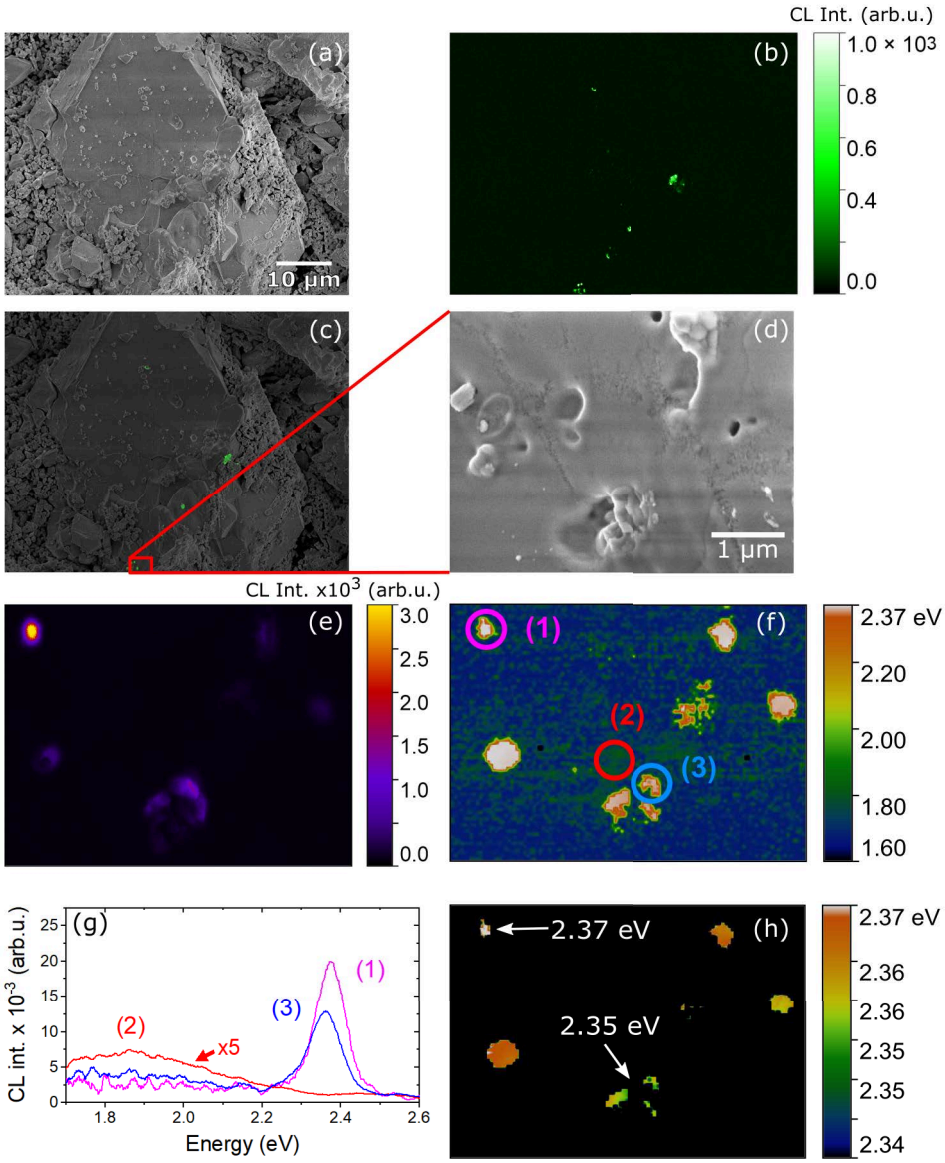

Figure 6.8: (a) Overview SEM image of the $CsPb_2Br_5$ powder and the corresponding (b) 550 nm CL intensity map. (c) CL map overlayed on the SEM image showing the area selected for analysis at higher magnification. (d) Magnified SEM image and the corresponding (e) 550 nm CL intensity map, where an inclusion was identified. (f) CL peak position map shows the distribution of the luminescence: the areas the in magenta red and blue circles are used to extract the CL spectra shown in (h), corresponding to the $CsPbBr_3$ nanoinclusion in the $CsPb_2Br_5$ matrix, a non-luminescent matrix region and a small $CsPbBr_3$ domain. The CL peak position map in (i) shows the differences of emission energy among different green-luminescent regions.

dielectric constant and not the nanocrystal size. The latter assumption is wrong, since the overlap between the confined electron and hole wave functions can increase their Coulomb interaction, increasing the exciton binding energy as a result. The model also assumes that the nanocrystals are confined with an infinite potential, which is not the case for $CsPbBr_3$ nanocrystals embedded in a solid matrix, such as Cs_4PbBr_6 or $CsPb_2Br_5$. Additionally, this simple model only gives information about the emission energy, but the correlated exciton wave function is not accessible. Therefore, in the next Section 6.4.2 a model that solves the problem of the correlated electron-hole pair is described and used to model the $Cs_4PbBr_6/CsPbBr_3/Cs_4PbBr_6$ and $CsPb_2Br_5/CsPbBr_3/CsPb_2Br_5$ systems.

6.4.2 Modeling excitons in a fully correlated confined system

The Hamiltonian describing an electron-hole pair system, including Coulomb interaction and dielectric effects, can be written — within the effective mass approximation — as [159–163]:

$$H(\mathbf{r}_e, \mathbf{r}_h) = H^{(e)}(\mathbf{r}_e) + H^{(h)}(\mathbf{r}_h) + V_c(\mathbf{r}_e, \mathbf{r}_h) \tag{6.1}$$

where $H^{(i)}$ is the single particle Hamiltonian for electron ($i = e$) and hole ($i = h$), and V_c is the generalized Coulomb interaction. The single-particle Hamiltonian is defined as:

$$H^{(i)}(\mathbf{r}_i) = -\nabla_i \frac{\hbar^2}{2m_i^*} \nabla_i + V_i^{pot}(\mathbf{r}_i) + V_i^{self}(\mathbf{r}_i) \tag{6.2}$$

where the first term is the kinetic energy operator for the particle with effective mass m_i^*, V_i^{pot} is the confining potential for particle i, which arises from band discontinuity at the interface between the materials, and V_i^{self} is the self-interaction potential for particle i, caused by the dielectric mismatch at the interface.

Solving the two-particle Schrödinger Equation (3.8b) using the Hamiltonian of Equation 6.1, can be achieved by at least two different methods: i) using the variational principle, in which, the parameters of an analytical wave function, are optimized to minimize E_{exc}; and ii) by using full configuration interaction, by diagonalizing H in a linear subspace of the Hilbert

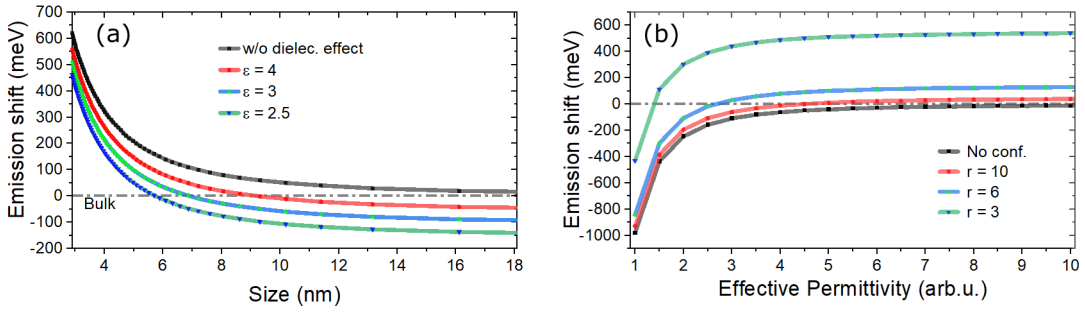

Figure 6.9: Emission energy shift of $CsPbBr_3$ in a dielectric environment calculated with the model described by the Brus Equation 3.6: (a) Size dependence without considering dielectric effects and with different effective dielectric constants. The model can predict red shifts in the emission energy for low and moderate confinement $r < 7\,\text{nm}$. This effect increases as the dielectric constant decreases. (b) Dependence on the effective dielectric constant considering no confinement and different nanocrystal sizes. For small nanocrystals, the blue shift caused by the strong confinement of the wave function still dominates the emission energy. The bulk emission energy is shown as a horizontal line as a reference

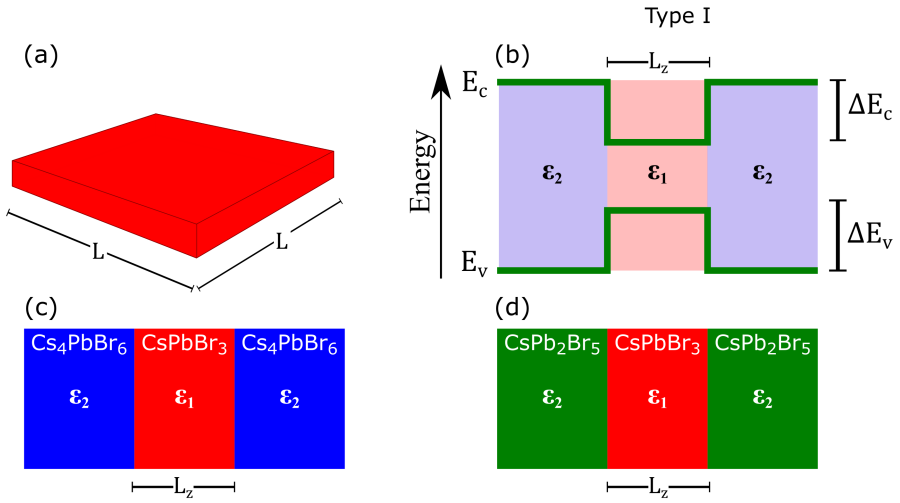

Figure 6.10: (a) Geometry of the nanoplatelet used to simulate the $CsPbBr_3$ embedded in a dielectric matrix. The dimensions L in the plane perpendicular to the confined direction, z, was kept fixed at 30 nm. (b) Band diagram showing the alignment of the conduction and valence bands (E_c and E_v) in the type I confinement considered in the final model, where ΔE_c and $\Delta E_c > 0$. L_z is the well width, and $\varepsilon_1 > \varepsilon_2$ are the dielectric constants of the different phases that constitute the modelled sytems: (c) $Cs_4PbBr_6/CsPbBr_3Cs_4PbBr_6$ and (d) $CsPb_2Br_5/CsPbBr_3/CsPb_2Br_5$

space, composed by a set of basis functions. The reader is referred to Chapter 4 of the book by Bányai and Koch [113] for further details in these methods.

In the present thesis, a variational method is used to solve equation 3.8b. More precisely, the semi-analytical fully correlated wave function with a single variational parameter and a Slater-type correlation factor is used, as proposed by Planelles [162] and as implemented by Rajadell, Climente, and Planelles [163]:

$$\Psi(\mathbf{r}_e, \mathbf{r}_h) = N\Phi_e(\mathbf{r}_e)\Phi_h(\mathbf{r}_h)e^{-a\sqrt{\|\mathbf{r}_{\parallel,e}-\mathbf{r}_{\parallel,h}\|^2}} \tag{6.3}$$

where N is the normalization constant Φ_i is the single-particle wave function of particle i, and the exponential term is the in-plane Slater-type correlation factor, where a is the variational parameter and $\mathbf{r}_{\parallel,i}$ is the in-plane position of electron or hole.

The model used in the present thesis has some limitations that are worth discussing before describing it in detail. First, a two-dimensional (2D) nanoplatelet is described, in which only the z direction is confined, while the perpendicular plane — (x, y) — is not ($L = 30$ nm, see Figure 6.10). The effects of the dielectric mismatch and of the potential confinement caused by the band offset are considered only in the z axis. Therefore, the model is an effective one-dimensional (1D) confined system.

The effects of quantum and dielectric confinements in the nanoplatelet are less pronounced than in a real nanocrystal confined in all directions. However, the model provides an easy-to-solve computational tool to investigate the effects of dielectric constant and band mismatch in mixed-phase Cs–Pb–Br systems. The self-interaction potential in the z direction is obtained using the method of image charges in a one-dimensional (1D) quantum well [118, 159, 163]:

$$V_i^{self}(z_i) = \sum_{n=\pm1,\pm2,\ldots} \frac{q_n e^2}{2\varepsilon 1\left[z_i - (-1)^n z_i + nL_z\right]} \tag{6.4}$$

where $q_n = \left(\frac{\varepsilon_1-\varepsilon_2}{\varepsilon_1+\varepsilon_2}\right)^{|n|}$, ε_1 is the dielectric constant in the well region (confined $CsPbBr_3$), ε_2 is the dielectric constant outside the well (barrier region, Cs_4PbBr_6 or $CsPb_2Br_5$), z_i is the electron (hole) z coordinate, and L_z is the with of the well. The single-particle confining potential can be described by a piece-wise function in one dimension:

$$V_i^{pot}(z_i) = \begin{cases} V_i & \text{if } \mid z_i \mid \geq \frac{L_z}{2} \\ 0 & \text{if } \mid z_i \mid < \frac{L_z}{2} \end{cases} \tag{6.5}$$

The Coulomb interaction term is obtained in a similar manner as the self-polarization potential, by calculating the interaction of the electron (hole) with the image charges induced by the hole (electron) [159]. Only the interaction term for carriers within the well is considered and can be described by [163]:

$$V_c(z_e, z_h) = \sum_{n=-\infty}^{\infty} \frac{q_n e^2}{\varepsilon_1 \sqrt{\|\mathbf{r}_{\parallel,e} - \mathbf{r}_{\parallel,h}\|^2 + \left[z_e - (-1)^n z_h + nL_z\right]^2}} \tag{6.6}$$

Finally, the variational parameter α is found by minimizing:

$$\begin{aligned} E_{exc} &= \langle\Psi|H|\Psi\rangle \\ &= \langle\Psi|H^{(e)}|\Psi\rangle + \langle\Psi|H^{(h)}|\Psi\rangle + \langle\Psi|V_c|\Psi\rangle \end{aligned} \tag{6.7}$$

where the first two terms are the single-particle contributions and the third term is the Coulomb correlation contribution. The first two terms can be expressed as:

$$\langle\Psi|H^{(i)}|\Psi\rangle = \langle\Psi|\widehat{T}^{(i)}|\Psi\rangle + \langle\Psi|V_i^{pot}|\Psi\rangle + \langle\Psi|V_i^{self}|\Psi\rangle \tag{6.8}$$

Kumagai and Takagahara [159] showed that the self-interaction only changes the confining potential slightly, and the eigenstates of the electron and hole contributions of equation 6.7 can be approximated using the eigenstates of the uncorrelated single-particle eigenstates. Thus, the potential contributions in equation 6.8 can be calculated as:

$$\langle\Psi|V_i^{self}|\Psi\rangle = \langle\Phi_i|V_i^{pot}|\Phi_i\rangle + \langle\Phi_i|V_i^{self}|\Phi_i\rangle \tag{6.9}$$

Also, the kinetic part can be calculated easily, because the Slater-type correlation factor has an additive closed form of the kinetic energy and can be expressed as [162]:

$$\langle\Psi|\widehat{T}^{(i)}|\Psi\rangle = \frac{k_x^2}{2\mu^*} + \frac{k_y^2}{2\mu^*} + \frac{a^2}{2\mu^*} + \langle\Phi_i|\widehat{T}^{(i)}|\Phi_i\rangle \tag{6.10}$$

where $k_{x/y} = \pi/L_{x/y}$ and $L_{x/y}$ are the in-plane dimensions of the nanoplatelet. Finally, the single-particle eigenfunctions can be calculated numerically using the finite differences method, as the solution to the single-particle, 1D Schrödinger equation:

$$\widehat{T}^{(i)}\,|\Phi_i\rangle + V_i^{pot}\,|\Phi_i\rangle = E_0^{(i)}\,|\Phi_i\rangle \tag{6.11}$$

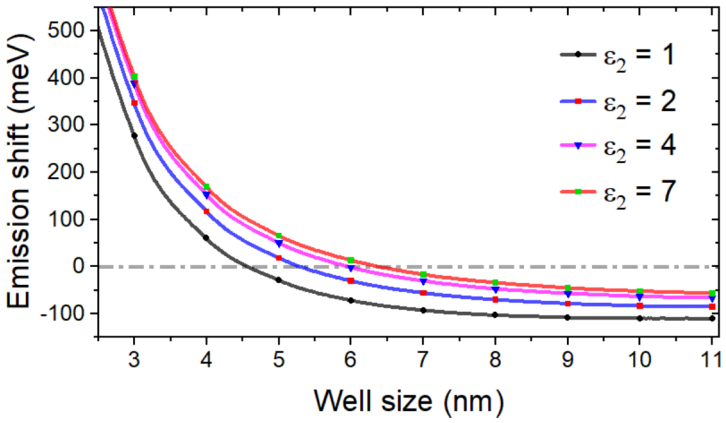

Figure 6.11: Calculated emission energy shift as a function of the well size (L_z) for an exciton in a $CsPbBr_3$ nanocrystal, modeled as an infinite potential well. The curves were calculated considering different dielectric constants for the surroundings (ε_2). The dielectric constant of $CsPbBr_3$ is assumed as $\varepsilon_1 = 5.0$. The dashed horizontal line shows the zero shift in emission energy (from the bad-gap energy transition).

The Coulomb interaction term (last term in Equation 6.7) is calculated by reducing a fourfold integral to a twofold one in a procedure that is detailed in the paper by Planelles [162]. The Mathematica code used in the calculation of the following results is largely based on the code developed by Rajadell, Climente, and Planelles [163], in which the method previously described is implemented.

6.4.3 Emission of $CsPbBr_3$ confined in an infinite potential

The first model system investigated here assumes that the $CsPbBr_3$ is confined with infinite potential barriers. This model does not include the effect of band mismatch, and serves as a direct comparison with the model by Equation 3.6, but it includes electron-hole correlation, carrier self-interaction, and dielectric mismatch in the calculation of the emission energy. Figure 6.11 shows the calculated shift in the emission energy as a function of the width of the potential well for different values of the dielectric constant of the surrounding matrix (ε_2). The values for the effective masses and dielectric constant of $CsPbBr_3$ used for these calculations are taken from those provided by Protesescu et al. [157]: $m_e^* = 0.15$, $m_h^* = 0.14$ and $\varepsilon_1 = 4.96$.

The trends of the shift in the emission energy with the size of the well are similar to those calculated using the Brus model (Figure 6.9a). However, it is important to point out one key difference: the Brus model considers the binding energy as independent of the confinement. Therefore, the curves in Figure 6.9a are just shifted up or down depending on the effective dielectric constant. In the model proposed in the present Section, the confinement of the electron and hole wave functions in the well increases their overlap. The Coulomb interaction and by extension the exciton binding energy increase with the confinement. Therefore, the exciton binding energy is a function of the well size (see Figure D.1). This is important, since the binding energy also determines the emission energy shift (see Equations 3.9 and 3.10) These results suggest that the effect of dielectric confinement is stronger for smaller nanocrystals, in agreement with the literature [159, 163–166].

6.4.4 Emission of $CsPbBr_3$ confined in a finite potential

A final and more complete model was considered, in which the $CsPbBr_3$ nanocrystal is embedded in finite potential barriers, given by the band-gap mismatch between $CsPbBr_3$ and the embedding secondary phase (either Cs_4PbBr_6 or $CsPb_2Br_5$). The carrier confinement is less effective within the finite barriers, since the wave function extends to the barrier regions. This reduces the effective dielectric constant of the system [159], which favors dielectric confinement, but at the same time it reduces the electron-hole overlap, which hinders the Coulomb interaction. Therefore, the end result on the shift of the emission energy is unclear at a first glance. Here, the shift is calculated using a set of parameters: (i) the well and barrier dielectric constants ε_1 and ε_2, and the well and barrier band gaps E_{g1} and E_{g2}. The calculations are simplified by considering a core-shell structure [163] in the z direction with shell thickness of 4 nm, where the dielectric constant of the surrounding medium is changed The model also considers the same effective mass for the core and the shell, with the same values as in Section 6.4.3. Although this model is not identical to the real material, it allows including the effect of the finite potential barriers, and understanding the exciton emission of $CsPbBr_3$ embedded in the other ternary phases at a reduced computational cost.

6.4.4.1 Ab-initio calculation of dielectric constants

Protesescu et al. [157] reported values for the effective masses and the dielectric constant of $CsPbBr_3$. However, there is no work in the literature reporting such values for all the three phases ($CsPbBr_3$, Cs_4PbBr_6, and $CsPb_2Br_5$), neither measured under the same experimental conditions nor calculated at the same level of theory. Therefore, here the electronic structure of all the three phases was calculated using density functional theorty (DFT), and the dielectric constants were calculated, using density functional perturbation theory (DFPT).

The calculation were performed using the Vienna Ab-initio Simulation Package (VASP)[121]. using the Perdew-Burke-Ernzerhof (PBE) form of the generalized gradient approximation to describe the exchange-correlation interactions [122], and including spin-orbit coupling (SOC). Dispersion interactions were included within the Tkatchenko-Scheffler scheme[123] using an iterative Hirshfeld partitioning of the charge-density [124, 125]. Core electrons are described by the projector augmented waves method[126, 127]. The orthorhombic structure of $CsPbBr_3$ [130] was used for the electronic structure calculations. A plain wave basis sets with cutoff of 700 eV was used and k-space integration was carried out on a $6 \times 6 \times 6$ grid. For Cs_4PbBr_6, the atomic structure reported by Velázquez et al. [50] was used as a starting point. A cutoff of 500 eV and a $4 \times 4 \times 3$ k-space grid were used. The structure of $CsPb_2Br_5$ reported by Cola and Riccardi [57] was used as a starting point; a cutoff of 700 eV and a $3 \times 3 \times 2$ k-space grid were used. The geometries were optimized using conjugate gradient optimization until the largest force was below 0.01 eV/Å. The high-frequency dielectric constant is calculated using DFPT as implemented by Gajdoš et al. [167] in the VASP package. Convergence was tested for all the parameters in the calculations.

Figure 6.12 summarizes the values calculated for the dielectric constants of all of the Cs–Pb–Br ternary phases. An interesting feature of the dielectric tensors of the $CsPbBr_3$ and $CsPb_2Br_5$ is their anisotropy. This is specially strong in the $CsPb_2Br_5$ and can be explained by the geometry of the crystal (the interested reader is referred to the discussion in Appendix

C.2). In the calculations presented in the following Section, a dielectric constant of $\varepsilon_1 = 4.2$ (average of ε in all the directions, since the variation is small) for the confined $CsPbBr_3$, $\varepsilon_2 = 3.1$ for Cs_4PbBr_6 and $\varepsilon_2 = 3.8$ for $CsPb_2Br_5$ were assumed. The lowest ε of the dielectric tensor of $CsPb_2Br_5$ is chosen, since as already shown and discussed in Section 6.4.3, the effect of the dielectric mismatch on the exciton emission is strongest when $\varepsilon_1 > \varepsilon_2$. Naturally, the anisotropy of $CsPb_2Br_5$ will reduce the dielectric confinement in two directions, and the implications will be discussed.

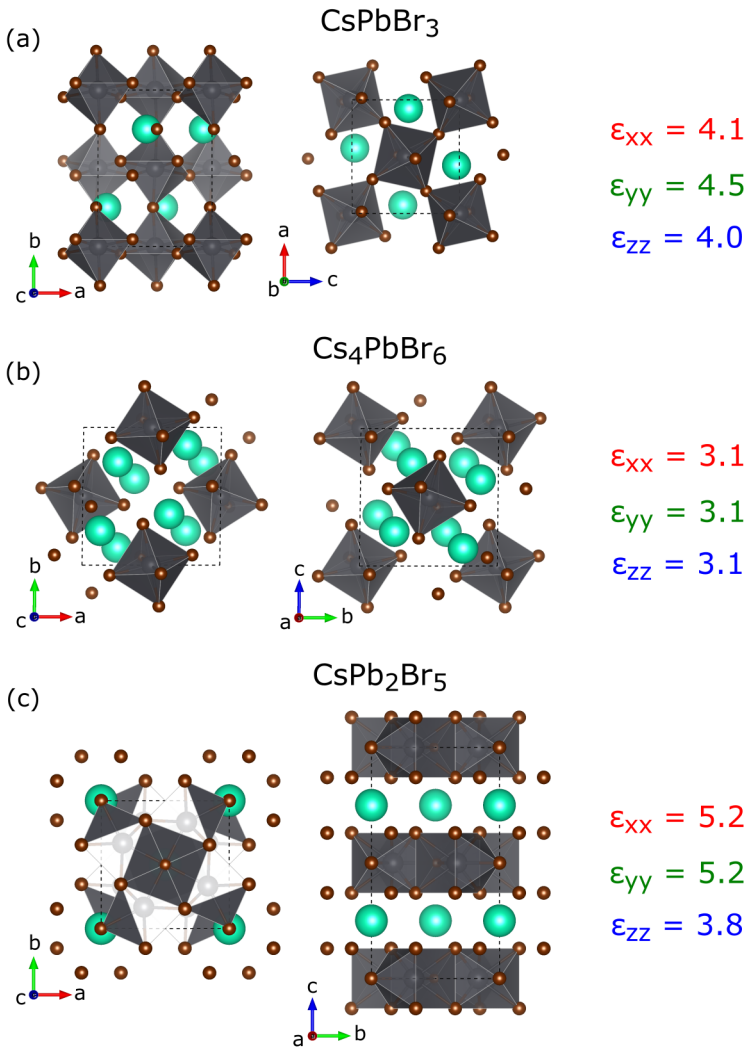

Figure 6.12: Crystal structures of (a) $CsPbBr_3$, (b) Cs_4PbBr_6, and (c) $CsPb_2Br_5$ oriented along relevant different lattice directions and diagonal elements of the dielectric tensor, in which the components are color-coded with the lattice direction. The geometry of the crystal determines the magnitude of the dielectric constant: disjoint polyhedra reduce orbital coupling and the polarizability, resulting in a lower dielectric constant

6.4.4.2 Band mismatch effects on the exciton emission

First, a $Cs_4PbBr_6/CsPbBr_3/Cs_4PbBr_6$ system is considered (Figure 6.10c). The difference in the band-gap energies between the phases (considering the values reported in Refs. [5, 11, 29, 30, 38, 52–55, 61]) is $\Delta E_g \simeq 1.7\,\text{eV}$. This difference is fixed, and by varying the band alignment, it is possible to model different types of confinement. Kang and Biswas [46] reported a type I band alignment for the $CsPbBr_3/Cs_4PbBr_6$ interface. Therefore, this type of alignment will

be the focus of the present Section. A type I system (Figure 6.10b) was modeled by setting the conduction and valence band offsets — ΔE_c and ΔE_v — equal: $\Delta E_c = \Delta E_v = \Delta E_g/2$. A more detailed discussion of the influence of the band alignment on the exciton emission can be found in Appendix D.2.

A net blue shift was calculated for well sizes below $\sim 4.3\,\text{nm}$ (Figure 6.13). For well sizes above that value, the electron-hole interaction energy overcomes the blue shift induced by the quantum confinement of the carriers, and the result is a net red shift of the emission energy, with respect to the band gap. This red shift is lower than the exciton binding energy of $CsPbBr_3$ bulk [85, 142, 155, 157] for well sizes of less than $\sim 6.5\,\text{nm}$, which is comparable with the reported exciton Bohr radius [157]. Larger well sizes induce a stronger red shift, owing to the weak quantum confinement and dominant dielectric confinement, which is a long-range interaction [159, 164]

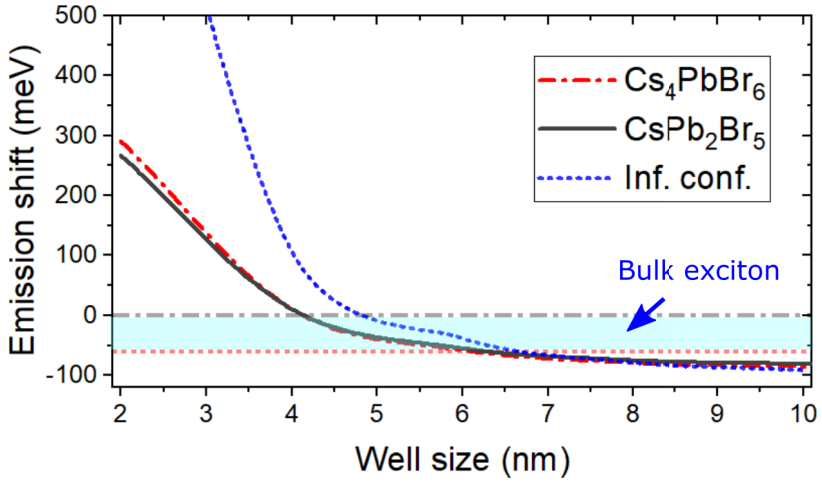

Figure 6.13: Calculated emission energy shift as a function of well size for $Cs_4PbBr_6/CsPbBr_3/Cs_4PbBr_6$ and $CsPb_2Br_5/CsPbBr_3/CsPb_2Br_5$ systems (only barrier material labeled). In the strong confinement regime a net blue shift was calculated, and for weak confinement, there is a net red shift owing to the dielectric confinement. The shaded region shows possible values of the exciton binding energy (see text for discussion) in $CsPbBr_3$ bulk. For weak confinement, with well size above the Bohr radius ($\sim$7 nm), the net red shift can be larger than the exciton binding energy, and thus, detectable by PL experiments. The emission shift considering a $CsPbBr_3$ nanocrystal confined in an infinite potential is also plotted for comparison

The results of a similar calculation for the $CsPb_2Br_5/CsPbBr_3/CsPb_2Br_5$ system (Figure 6.10d) is also shown in Figure 6.13. In this case, $\Delta E_g \simeq 1.4\,\text{eV}$, considering the reported band-gap energies of the phases [19, 56, 58]. The system behaves similarly to the $Cs_4PbBr_6/CsPbBr_3/Cs_4PbBr_6$. However, owing to the smaller ΔE_g and larger dielectric constant, the effects of quantum and dielectric confinement are smaller. The largest difference in emission shift was found for the strong confinement regime, while for weak confinement, the red shift is almost unchanged. This means that, assuming a type I band alignment for the $CsPbBr_3/CsPb_2Br_5$ interface, the effect of dielectric confinement is similar for $CsPbBr_3$ nanocrystals embedded in either Cs_4PbBr_6 or $CsPb_2Br_5$. The differences in emission shift (see Figure 6.5) are then explained by different confinement regimes. In Figure 6.13 the emission shift of the $CsPb_2Br_5/CsPbBr_3/CsPb_2Br_5$ system with infinite potential barriers is shown for comparison. Note that the model with infinite potential barriers, even considering the dielectric mismatch effects in a fully correlated way, leads to overestimation of the blue shift

for $CsPbBr_3$ nanocrystals embedded in a solid matrix of $CsPb_2Br_5$ (similar results are found for Cs_4PbBr_6).

Finally, in order to understand the effects of confinement in the luminescence quantum yield, the electron-hole overlap, which is proportional to the oscillator strength [166, 168, 169] was calculated as:

$$S_{eh}^2 = | \langle \Phi_e(\mathbf{r}_e) | \Phi_h(\mathbf{r}_h) \rangle |^2 \tag{6.12}$$

Figure 6.14 shows the calculated S_{eh}^2 as a function of the well size for the $Cs_4PbBr_6/CsPbBr_3/Cs_4PbBr_6$ and $CsPb_2Br_5/CsPbBr_3/CsPb_2Br_5$ systems. The effective electron and hole confinement results in high wave function overlap, and by extension a large oscillator strength and enhanced luminescence. The overlap depends strongly on the well width, and for large values it is similar to the overlap estimated considering an infinite potential well (also shown in Figure 6.14). For strong confinement, the difference in S_{eh}^2 between systems with Cs_4PbBr_6 or $CsPb_2Br_5$ barriers is small. This means that the differences in PL intensity can be only explained by differences in the size of the embedded $CsPbBr_3$ nanocrystal. The emission shift was also satisfactory explained by the nanocrystal size, which suggests that the $CsPbBr_3$ nanocrystals embedded in $CsPb_2Br_5$ are larger than those in Cs_4PbBr_6.

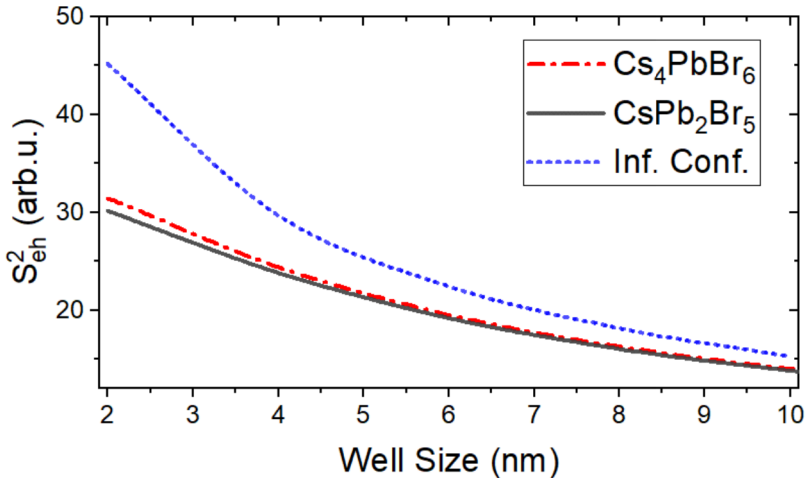

Figure 6.14: Calcuated electron-hole overlap as a function of well size for $Cs_4PbBr_6/CsPbBr_3/Cs_4PbBr_6$ and $CsPb_2Br_5/CsPbBr_3/CsPb_2Br_5$ systems (only barrier material labeled). The difference between the Cs_4PbBr_6 and $CsPb_2Br_5$ systems is negligible. The overlap of the model with infinite potential barriers is also plotted for comparison

6.5 Summary and discussion

This Chapter studied composite Cs–Pb–Br materials from an experimental and theoretical perspective, addressing three open issues undeer debate, i.e., the origin of the green luminescence in allegedly pure Cs_4PbBr_6 or $CsPb_2Br_5$, the enhanced luminescence mechanism in such materials, and under the assumption of confined $CsPbBr_3$ inclusions, what does the the emission shift tells about the confined nanocrystals.

First, the different recombination pathways of bulk $CsPbBr_3$ in powder form were studied by means of temperature- and intensity-dependent PL spectroscopy. Various PL bands were

identified corresponding to band-to-band recombination, excitonic transitions, shallow and deep defect-level-mediated recombination. The latter is only detectable at low temperatures $< 90\,\mathrm{K}$ and it is positioned $\sim 200\,\mathrm{meV}$ below the free exciton transition, in good agreement with the values reported by Nitsch et al. [29]. The excitonic and shallow defect levels transitions were also measured at room temperature. Intensity-dependent PL revealed that the trap-mediated, nonradiative recombination dominates in $CsPbBr_3$ bulk, in agreement with the enhanced luminescence at low temperature. Furthermore, acceleration-voltage dependent CL revealed that the radiative, shallow-trap recombination is dominant at the surface of the material. This suggests that defects with shallow levels are more concentrated towards the surface of the $CsPbBr_3$.

Secondly, the intensity-dependent PL analyses of green-luminescent Cs_4PbBr_6 and $CsPb_2Br_5$ revealed the more excitonic nature of the recombination in these materials. The green PL intensity of $CsPb_2Br_5$ increases one order of magnitude with respect to the intensity of the bulk $CsPbBr_3$, and that of Cs_4PbBr_6 three orders of magnitude. The emission peaks exhibit a net red and blue shift with respect to bulk $CsPbBr_3$ for $CsPb_2Br_5$ and Cs_4PbBr_6, respectively. CL maps and spectra, together with EDX elemental maps revealed that the origin of the green luminescence is $CsPbBr_3$ nanocrystals embedded in the Cs_4PbBr_6 and $CsPb_2Br_5$. This results are in very good agreement with those recently presented by Riesen et al. [147] who used a similar microscopy approach. Additionally, CL spectra on the $CsPb_2Br_5$ confirmed the presence of a defect-associated band at $\sim 1.8\,\mathrm{eV}$, that was reported for the mixed-phase thin films in Chapter 5 [109].

Finally, $Cs_4PbBr_6/CsPbBr_3/Cs_4PbBr_6$ and $CsPb_2Br_5/CsPbBr_3/CsPb_2Br_5$ systems were modeled by various methods with different levels of complexity. The Brus model [111] with a hydrogenic Wannier-Mott exciton [147, 170, 171] has been recently used by Cho and Yun [171] to estimate the size of the nanocrystal inclusions in $Cs_4PbBr_6/CsPbBr_3$ systems. They estimated diameters from 5.6 to 6.2 nm, which were larger, compared with their TEM-measured mean diameter of 4.2 nm. They attributed the discrepancy between the values to the non-spherical nature of the embedded crystals, but it is important to point out that within their model, they considered the effective dielectric constant ε to be that of the surrounding Cs_4PbBr_6. Also, this model does not consider the electron-hole correlation, and the self-interaction. However, by considering the dielectric environment with a Wannier-Mott exciton model already offers a better approximation to the size of the nanocrystals than the simple confinement model, which would predict sizes from 5.9 to 6.6 nm.

A more sophisticated EMA model [163] was implemented which considers quantum and dielectric confinement of $CsPbBr_3$ nanocrystals in a infinite potential barrier, considering fully correlated exciton wave function. The model explained how the lower dielectric constant of the embedding material increases the exciton binding energy in the $CsPbBr_3$ nanocrystals, which reduces the blue shift expected from the quantum confinement effect. The calculation of a fully correlated system shows that the dielectric confinement depends on the size of the nanocrystal, in contrast with the Brus model, which considers it independent. A final model that considers finite potential barriers was studied. It was found that the dielectric confinement increase the exciton binding energy and for large enough nanocrystals, it can

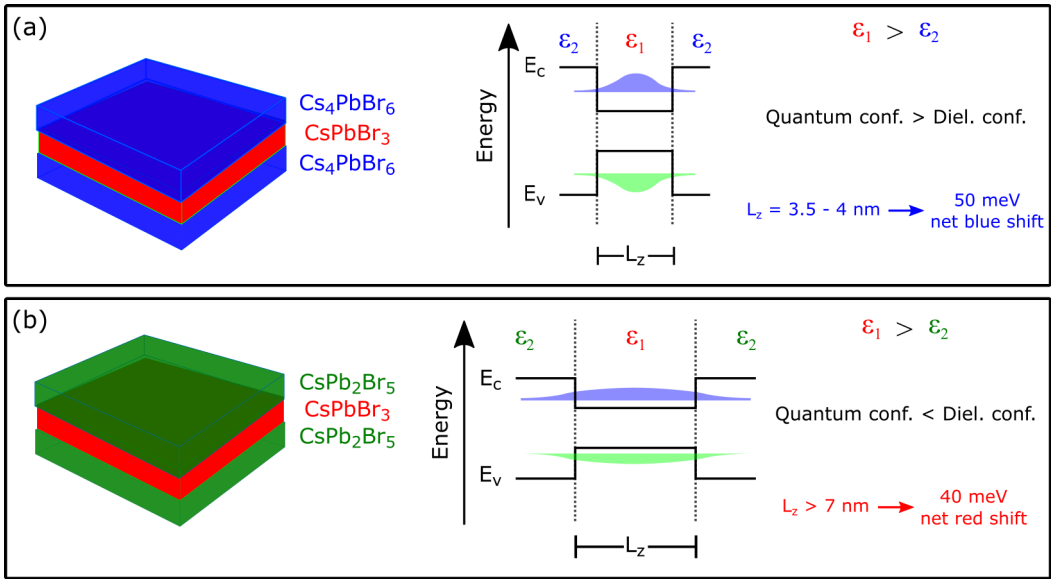

Figure 6.15: Summary of the results of the optical characterization and the model of the (a) $Cs_4PbBr_6/CsPbBr_3/Cs_4PbBr_6$ and (b) $CsPb_2Br_5/CsPbBr_3/CsPb_2Br_5$ confined systems. Both systems exhibit dielectric confinement with $\varepsilon_1 > \varepsilon_2$. The system in (a) exhibits a large quantum confinement and a net blue shift. However, the system in (b) exhibits weak quantum confinement ($L_z > 7\,\text{nm}$), which reduces the electron-hole overlap and by extension the oscillator strength. In the weak confinement regime, the dielectric confinement exceeds the quantum confinement, which results in a net red shift

overcome the quantum-confinement-induced blue shift, which results in a net red shift of the exciton emission. The results are summarized in Figure 6.15.

The calculations presented here showed that the simple Brus equation overestimates the size of the nanocrystals in the case of composite solid materials, owing to the effects of the finite potential barriers and dielectric confinement. This suggests that for the $CsPbBr_3/Cs_4PbBr_6$ material, the most likely scenario is to have strongly confined nanocrystals, regardless of the limited blue shift reported for this material [51]. Although Kang and Biswas [46] reported a type I band alignment at the $CsPbBr_3Cs_4PbBr_6$ interface, based on DFT calculations (PBE0 hybrid functional with 25 % exact exchange), there has not been any reports of the experimental band alignment in this composite system. An experimental determination of the ionization potential and electron affinity might help to confirm (or reject) the type I alignment.

In $CsPbBr_3/CsPb_2Br_5$ reported by Cho and Yun [171], the $CsPbBr_3$ nanocrystals in $CsPb_2Br_5$ are $\sim 15\,\text{nm}$ in average, and in general larger than those for similarly synthesized $CsPbBr_3/Cs_4PbBr_6$ systems. Therefore, a plausible explanation for the effective red shift observed in the composite reported here is the larger size of the nanocrystals, which can be expected from the close formation enthalpies of the $CsPbBr_3$ and $CsPb_2Br_5$ phases — as discussed in Chapter 4 [109]. Since no data has been reported regarding the band alignment at the $CsPbBr_3/CsPb_2Br_5$ interface, the results presented here are under the assumption of type I confined nanocrystals. Experimental or theoretical determination of the band alignment is still necessary to complete the model.

The model presented in the present Chapter can be largely improved. In one hand, for instance, including the influence of spin-orbit coupling, which can lead to changes in the electron and hole states due to the band splittings of the degenerate band states [113]. Sercel

et al. [172] have shown the importance of spin-orbit coupling effect in the exciton fine structure of $CsPbBr_3$ nanocrystals. On the other hand, the effects of non-parabolicity of the band edges [173], the mass confinement by considering the effective masses of Cs_4PbBr_6 and $CsPb_2Br_5$ in the calculation, and a three dimensional model that considers the anisotropy of the effective masses and dielectric mismatch can also provide additional information on the optical properties of the Cs–Pb–Br composites considered here.

7

Conclusions and Outlook

In the present work, the composition as well as optical and structural properties of the ternary phases in the Cs–Pb–Br material system — $CsPbBr_3$, Cs_4PbBr_6 and $CsPb_2Br_5$ — were studied by means of a combination of diffraction and spectroscopy techniques. Theoretical calculations were performed in order to help understanding the experimental results and explain the effect of quantum and dielectric confinement in mixed-phase materials.

The various ternary phases coexist in thin films grown by different deposition methods, which agrees well with the DFT calculations that resulted in very similar formation enthalpies of the ternary phases. The phase distribution was investigated with a spatial resolution of down to 50 nm by correlating the elemental and luminescence distribution maps of the surfaces and the cross section of the films. It was found that the absorption of visible light in these mixed-phase films is dominated by the absorption of the low-band-gap $CsPbBr_3$, but that the emission can exhibit contributions of the other phases in case the excitation energy is sufficiently large. Low-energy emission bands and blue shifts in the luminescence spectra were explained by deep defect recombination and interface strain.

Phase transition and its influence on the luminescence yield were also investigated in coevaporated $CsPbBr_3/CsPb_2Br_5$ thin films. Owing to their very similar formation enthalpies, $CsPb_2Br_5$ can be transformed into $CsPbBr_3 + PbBr_2$ by annealing at elevated temperatures. Using in-situ XRD, it was found that the transformation $CsPb_2Br_5 \longrightarrow CsPbBr_3 + PbBr_2$ only takes place when annealing above 580 K, and that annealing at lower temperatures only leads to crystal structure transitions and increase of the domain size in $CsPbBr_3$, together with thermal expansion of $CsPb_2Br_5$. PL analyses revealed that after annealing, the broad low-energy transition — localized within $CsPb_2Br_5$ and at its interface with $CsPbBr_3$ — is enhanced and the green emission is quenched. These results lead to the conclusion that defects of the $PbBr_2$-rich phase at the $CsPb_2Br_5/CsPbBr_3$ interface are detrimental to the PLQY of the film, which is in contrast to a passivation mechanism proposed by other authors.

The origin and properties of the green luminescence in presumably pure Cs_4PbBr_6 and $CsPb_2Br_5$ was also investigated. Green luminescent bulk Cs_4PbBr_6 and $CsPb_2Br_5$ were characterized, and evidence for $CsPbBr_3$ nanocrystals embedded in the solid matrix was found. The green PL intensity in these composite materials is higher by one to three orders of

magnitude than in the $CsPbBr_3$ bulk, featuring a blue shift in the case of Cs_4PbBr_6 and a red shift for $CsPb_2Br_5$. These experimental results were explained by means of an effective mass approximation model of the confined system.

It was found that the widely used Brus equation with a Wannier-Mott exciton model, underestimates considerably the size of nanocrystals embedded in a solid matrix with lower dielectric constant. A model that takes into account the finite potential and full electron-hole correlation was introduced for $Cs_4PbBr_6/CsPbBr_3/Cs_4PbBr_6$ and $CsPb_2Br_5/CsPbBr_3/CsPb_2Br_5$ quantum well structures. The model showed that dielectric confinement increases the exciton binding energy, which results in an emission red shift, which for sufficiently large nanocrystals can overcome the quantum-confinement-induced blue shift. The model also explained the bright, green emission and modest, blue shift of Cs_4PbBr_6 measured experimentally on strongly confined nanocrystals. The red shift and modest enhancement in emission measured for $CsPb_2Br_5$ was explained by larger nanocrystals, which results in the dielectric confinement effect being stronger than the weak quantum confinement. The theoretical and experimental results are in good quantitative agreement, also with experimental results reported by other authors.

In order to gain a deeper understanding of this material system, similar studies should be conducted considering the reverse phase transformation $2\,CsPbBr_3 \longrightarrow CsPb_2Br_5 + CsBr$, which has been reported to occur upon exposure to H_2O. Additionally, the implications of confinement effects can be further investigated by studying composite materials with $CsPbBr_3$ inclusions of controllable size. X-ray photoluminescence spectroscopy (XPS) and ultraviolet photoelectron spectroscopy (UPS) can be used to estimate the bands positions of the different phases and estimate the band alignment of the different phases to feed the theoretical model. Furthermore, the model can be improved by considering three-dimensional finite confinement, as well as infinitely extended potential barriers, in order to resemble the experimental conditions more accurately. This can be implemented by finding a numerically exact solution by means of configurations interaction.

In summary, the present thesis shows how correlative microscopic compositional and luminescence mapping are valuable tools to understand the macroscopic optical properties of $CsPbBr_3$ and related materials. The combination of the optical spectroscopy, structural characterization, microscopic correlative investigations, and theoretical modeling provided insights into the physics of the debated green luminescence of Cs–Pb–Br material sytems, and can be an important basis for the explanation of similar phenomena in other lead-halide perovskites.

References

[1] Dan Tong et al. “Committed emissions from existing energy infrastructure jeopardize 1.5 °C climate target”. In: *Nature* 572.7769 (2019), pp. 373–377. ISSN: 1476-4687. DOI: 10.1038/s41586-019-1364-3.

[2] Philip Sterchele et al. *WEGE ZU EINEM KLIMANEUTRALEN ENERGIESYSTEM: Die deutsche Energiewende im Kontext gesellschaftlicher Verhaltensweisen*. Tech. rep. Freiburg: Fraunhofer-Institut für Solare Energieshsteme ISE, 2020.

[3] Fraunhofer Institut ISE. *Energy Charts*. 2020. URL: https://www.energy-charts.de/.

[4] Mahshid Ahmadi, Ting Wu, and Bin Hu. “A Review on Organic–Inorganic Halide Perovskite Photodetectors: Device Engineering and Fundamental Physics”. In: *Adv. Mater.* 29.41 (2017), pp. 1–24. ISSN: 1521-4095. DOI: 10.1002/adma.201605242.

[5] Jia Liang, Jie Liu, and Zhong Jin. “All-Inorganic Halide Perovskites for Optoelectronics: Progress and Prospects”. In: *Sol. RRL* 1.10 (2017), p. 1770138. ISSN: 2367-198X. DOI: 10.1002/solr.201770138.

[6] Juan-Pablo Correa-Baena et al. “Promises and challenges of perovskite solar cells”. In: *Science (80-.).* 358.6364 (2017), pp. 739–744. ISSN: 0036-8075. DOI: 10.1126/science.aam6323.

[7] David A. Egger et al. “What Remains Unexplained about the Properties of Halide Perovskites?” In: *Adv. Mater.* 30.20 (2018), p. 1800691. DOI: 10.1002/adma.201800691.

[8] Michael Kulbak et al. “Cesium Enhances Long-Term Stability of Lead Bromide Perovskite-Based Solar Cells”. In: *J. Phys. Chem. Lett.* 7.1 (2016), pp. 167–172. ISSN: 1948-7185. DOI: 10.1021/acs.jpclett.5b02597. arXiv: 1511.07781.

[9] Rebecca J. Sutton et al. “Bandgap-Tunable Cesium Lead Halide Perovskites with High Thermal Stability for Efficient Solar Cells”. In: *Adv. Energy Mater.* 6.8 (2016), pp. 1–6. ISSN: 1614-6840. DOI: 10.1002/aenm.201502458. arXiv: arXiv:1408.1149.

[10] Azat F. Akbulatov et al. “Probing the Intrinsic Thermal and Photochemical Stability of Hybrid and Inorganic Lead Halide Perovskites”. In: *J. Phys. Chem. Lett.* 8.6 (2017), pp. 1211–1218. ISSN: 1948-7185. DOI: 10.1021/acs.jpclett.6b03026.

[11] Michael Kulbak, David Cahen, and Gary Hodes. “How Important Is the Organic Part of Lead Halide Perovskite Photovoltaic Cells? Efficient $CsPbBr_3$ Cells”. In: *J. Phys. Chem. Lett.* 6.13 (2015), pp. 2452–2456. ISSN: 1948-7185. DOI: 10.1021/acs.jpclett.5b00968.

[12] Guoqing Tong et al. “Phase transition induced recrystallization and low surface potential barrier leading to 10.91%-efficient $CsPbBr_3$ perovskite solar cells”. In: *Nano Energy* 65 (2019), p. 104015. ISSN: 2211-2855. DOI: 10.1016/j.nanoen.2019.104015.

[13] Natalia Yantara et al. “Inorganic Halide Perovskites for Efficient Light-Emitting Diodes”. In: *J. Phys. Chem. Lett.* 6.21 (2015), pp. 4360–4364. ISSN: 1948-7185. DOI: 10.1021/acs.jpclett.5b02011. eprint: arXiv:1011.1669v3.

[14] Yan Fong Ng et al. “Rapid Crystallization of All-Inorganic $CsPbBr_3$ Perovskite for High-Brightness Light-Emitting Diodes”. In: *ACS Omega* 2.6 (2017), pp. 2757–2764. ISSN: 2470-1343. DOI: 10.1021/acsomega.7b00360.

[15] Kebin Lin et al. “Perovskite light-emitting diodes with external quantum efficiency exceeding 20 per cent”. In: *Nature* 562.7726 (2018), pp. 245–248. ISSN: 1476-4687. DOI: 10.1038/s41586-018-0575-3.

[16] Neda Pourdavoud et al. “Room-Temperature Stimulated Emission and Lasing in Recrystallized Cesium Lead Bromide Perovskite Thin Films”. In: *Adv. Mater.* 31.39 (2019), p. 1903717. ISSN: 0935-9648. DOI: 10.1002/adma.201903717.

[17] Torsten Langer et al. “Origin of the "green gap": Increasing nonradiative recombination in indium-rich GaInN/GaN quantum well structures”. In: *Phys. Status Solidi Curr. Top. Solid State Phys.* 8.7-8 (2011), pp. 2170–2172. ISSN: 1862-6351. DOI: 10.1002/pssc.201001051.

[18] Faiz Rahman. “The shrinking green gap: trends in solid-state green emitters”. In: *Photonics Spectra* 53.1 (2019), pp. 52–59. ISSN: 0731-1230. URL: https://www.photonics.com/Articles/The%7B%5C_%7DShrinking%7B%5C_%7DGreen%7B%5C_%7DGap%7B%5C_%7DTrends%7B%5C_%7Din%7B%5C_%7DSolid-State/a64221.

[19] Ibrahim Dursun et al. “$CsPb_2Br_5$ Single Crystals: Synthesis and Characterization”. In: *ChemSusChem* 10.19 (2017), pp. 3746–3749. ISSN: 1864-5631. DOI: 10.1002/cssc.201701131.

[20] Francisco Palazon et al. “Postsynthesis Transformation of Insulating Cs_4PbBr_6 Nanocrystals into Bright Perovskite $CsPbBr_3$ through Physical and Chemical Extraction of CsBr”. In: *ACS Energy Lett.* 2.10 (Oct. 2017), pp. 2445–2448. ISSN: 2380-8195. DOI: 10.1021/acsenergylett.7b00842.

[21] Francisco Palazon et al. “From $CsPbBr_3$ Nano-Inks to Sintered $CsPbBr_3$-$CsPb_2Br_5$ Films via Thermal Annealing: Implications on Optoelectronic Properties”. In: *J. Phys. Chem. C* 121.21 (2017), pp. 11956–11961. ISSN: 1932-7455. DOI: 10.1021/acs.jpcc.7b03389.

[22] Quinten A. Akkerman et al. “Nearly Monodisperse Insulator Cs_4PbX_6 (X = Cl, Br, I) Nanocrystals, Their Mixed Halide Compositions, and Their Transformation into $CsPbX_3$ Nanocrystals”. In: *Nano Lett.* 17.3 (2017), pp. 1924–1930. ISSN: 1530-6992. DOI: 10.1021/acs.nanolett.6b05262.

[23] Bekir Turedi et al. “Water-Induced Dimensionality Reduction in Metal-Halide Perovskites”. In: *J. Phys. Chem. C* 122.25 (2018), pp. 14128–14134. ISSN: 1932-7455. DOI: 10.1021/acs.jpcc.8b01343.

[24] Christophe Tenailleau et al. “Cell refinement of $CsPbBr_3$ perovskite nanoparticles and thin films”. In: *Nanoscale Adv.* 1.1 (2019), pp. 147–153. DOI: 10.1039/c8na00122g.

[25] G Maity and S K Pradhan. “Composition related structural transition between mechanosynthesized $CsPbBr_3$ and $CsPb_2Br_5$ perovskites and their optical properties”. In: *J. Alloys Compd.* 816 (2020), p. 152612. DOI: 10.1016/j.jallcom.2019.152612.

[26] Subila K. Balakrishnan and Prashant V. Kamat. “Ligand Assisted Transformation of Cubic $CsPbBr_3$ Nanocrystals into Two-Dimensional $CsPb_2Br_5$ Nanosheets”. In: *Chem. Mater.* 30.1 (2018), pp. 74–78. ISSN: 1520-5002. DOI: 10.1021/acs.chemmater.7b04142.

[27] Suneth C. Watthage et al. “Evolution of perovskite solar cells”. In: *Perovskite Photovoltaics Basic to Adv. Concepts Implement.* Elsevier Inc., 2018, pp. 43–88. ISBN: 9780128129159. DOI: 10.1016/B978-0-12-812915-9.00003-4.

[28] Jarvist M Frost and Aron Walsh. “Molecular Motion and Dynamic Crystal Structures of Hybrid Halide Perovskites BT - Organic-Inorganic Halide Perovskite Photovoltaics: From Fundamentals to Device Architectures”. In: ed. by Nam-Gyu Park, Michael Grätzel, and Tsutomu Miyasaka. Cham: Springer International Publishing, 2016, pp. 1–17. ISBN: 978-3-319-35114-8. DOI: 10.1007/978-3-319-35114-8_1.

[29] K. Nitsch et al. “Lead bromide and ternary alkali lead bromide single crystals - Growth and emission properties”. In: *Chem. Phys. Lett.* 258.3-4 (1996), pp. 518–522. ISSN: 0009-2614. DOI: 10.1016/0009-2614(96)00665-3.

[30] M. Nikl et al. “Optical properties of Pb^2+-based aggregated phases in CsBr thin film and single crystal matrices”. In: *Radiat. Eff. Defects Solids* 150.1-4 (1999), pp. 341–345. ISSN: 1042-0150. DOI: 10.1080/10420159908226254.

[31] Akihiro Kojima et al. “Organometal Halide Perovskites as Visible-Light Sensitizers for Photovoltaic Cells”. In: *J. Am. Chem. Soc.* 131.17 (2009), pp. 6050–6051. DOI: 10.1021/ja809598r.

[32] Martin A Green et al. “Solar cell efficiency tables (Version 55)”. In: *Prog. Photovoltaics Res. Appl.* 28.1 (Jan. 2020), pp. 3–15. ISSN: 1062-7995. DOI: 10.1002/pip.3228.

[33] Martin A Green, Anita Ho-Baillie, and Henry J Snaith. “The emergence of perovskite solar cells”. In: *Nat. Photonics* 8.7 (2014), pp. 506–514. ISSN: 1749-4885. DOI: 10.1038/nphoton.2014.134.

[34] Nam-Gyu Park, Michael Grätzel, and Tsutomu Miyasaka. *Organic-Inorganic Halide Perovskite Photovoltaics*. ISBN: 978-3-319-35112-4. DOI: 10.1007/978-3-319-35114-8_4.

[35] Constantinos C. Stoumpos et al. “Crystal Growth of the Perovskite Semiconductor CsPbBr 3 : A New Material for High-Energy Radiation Detection”. In: *Cryst. Growth Des.* 13 (2013), 2722-2727. ISSN: 1528-7483. DOI: dx.doi.org/10.1021/cg400645t. eprint: arXiv:1408.1149.

[36] Makhsud I. Saidaminov et al. “Inorganic Lead Halide Perovskite Single Crystals: Phase-Selective Low-Temperature Growth, Carrier Transport Properties, and Self-Powered Photodetection”. In: *Adv. Opt. Mater.* 5.2 (2017), p. 1600704. ISSN: 2195-1071. DOI: 10.1002/adom.201600704.

[37] Tiebin Yang, Feng Li, and Rongkun Zheng. "Recent Progress on Cesium Lead Halide Perovskites for Photodetection Applications". In: *ACS Appl. Electron. Mater.* 1.8 (2019), pp. 1348–1366. ISSN: 2637-6113. DOI: 10.1021/acsaelm.9b00346.

[38] Jie Lei et al. "Efficient planar $CsPbBr_3$ perovskite solar cells by dual-source vacuum evaporation". In: *Sol. Energy Mater. Sol. Cells* 187.July (2018), pp. 1–8. ISSN: 0927-0248. DOI: 10.1016/j.solmat.2018.07.009.

[39] Xisheng Zhang et al. "All-Ambient Processed Binary $CsPbBr_3$-$CsPb_2Br_5$ Perovskites with Synergistic Enhancement for High-Efficiency Cs-Pb-Br-Based Solar Cells". In: *ACS Appl. Mater. Interfaces* 10.8 (2018), pp. 7145–7154. ISSN: 1944-8252. DOI: 10.1021/acsami.7b18902.

[40] Juan Li et al. "Fabrication of efficient $CsPbBr_3$ perovskite solar cells by single-source thermal evaporation". In: *J. Alloys Compd.* xxxx (2019), p. 152903. ISSN: 0925-8388. DOI: 10.1016/j.jallcom.2019.152903.

[41] Masood Mehrabian et al. "A Highly Stable All-Inorganic $CsPbBr_3$ Perovskite Solar Cell". In: *Eur. J. Inorg. Chem.* 2019.32 (2019), pp. 3699–3703. ISSN: 1099-0682. DOI: 10.1002/ejic.201900562.

[42] Tianxing Xiang et al. "Universal defects elimination for high performance thermally evaporated $CsPbBr_3$ perovskite solar cells". In: *Sol. Energy Mater. Sol. Cells* 206.November (2020), p. 110317. ISSN: 0927-0248. DOI: 10.1016/j.solmat.2019.110317.

[43] Nir Klein-Kedem, David Cahen, and Gary Hodes. "Effects of Light and Electron Beam Irradiation on Halide Perovskites and Their Solar Cells". In: *Acc. Chem. Res.* 49.2 (2016), pp. 347–354. ISSN: 1520-4898. DOI: 10.1021/acs.accounts.5b00469.

[44] Chuanxiao Xiao et al. "Mechanisms of Electron-Beam-Induced Damage in Perovskite Thin Films Revealed by Cathodoluminescence Spectroscopy". In: *J. Phys. Chem. C* 119.48 (2015), pp. 26904–26911. ISSN: 1932-7455. DOI: 10.1021/acs.jpcc.5b09698.

[45] Wei Li et al. "Phase Segregation Enhanced Ion Movement in Efficient Inorganic $CsPbIBr_2$ Solar Cells". In: *Adv. Energy Mater.* 7.20 (2017), pp. 1–8. ISSN: 1614-6840. DOI: 10.1002/aenm.201700946.

[46] Byungkyun Kang and Koushik Biswas. "Exploring Polaronic, Excitonic Structures and Luminescence in Cs_4PbBr_6/$CsPbBr_3$". In: *J. Phys. Chem. Lett.* 9.4 (2018), pp. 830–836. ISSN: 1948-7185. DOI: 10.1021/acs.jpclett.7b03333. eprint: 0005059v1.

[47] Omer Yaffe et al. "Local Polar Fluctuations in Lead Halide Perovskite Crystals". In: *Phys. Rev. Lett.* 118.13 (2017), pp. 1–6. ISSN: 1079-7114. DOI: 10.1103/PhysRevLett.118.136001. eprint: 1604.08107.

[48] Ayala V. Cohen et al. "Breakdown of the static picture of defect energetics in halide perovskites: the case of the Br vacancy in $CsPbBr_3$". In: *J. Phys. Chem. Lett.* 10.16 (2019), pp. 4490–4498. DOI: 10.1021/acs.jpclett.9b01855. eprint: 1810.04462.

[49] Mei Liu et al. "Unveiling Solvent-Related Effect on Phase Transformations in CsBr-$PbBr_2$ System: Coordination and Ratio of Precursors". In: *Chem. Mater.* 30.17 (2018), pp. 5846–5852. ISSN: 1520-5002. DOI: 10.1021/acs.chemmater.8b00537.

[50] Matias Velázquez et al. "Growth and characterization of pure and Pr^3+-doped Cs_4PbBr_6 crystals". In: *J. Cryst. Growth* 310.24 (2008), pp. 5458–5463. ISSN: 0022-0248. DOI: 10.1016/j.jcrysgro.2008.10.003. URL: http://www.sciencedirect.com/science/article/pii/S0022024808010464.

[51] Quinten A. Akkerman, Ahmed L. Abdelhady, and Liberato Manna. "Zero-Dimensional Cesium Lead Halides: History, Properties, and Challenges". In: *J. Phys. Chem. Lett.* 9.9 (2018), pp. 2326–2337. ISSN: 1948-7185. DOI: 10.1021/acs.jpclett.8b00572.

[52] V Babin et al. "Luminescence of Cs_4PbBr_6 Aggregates in As-Grown and in Annealed CsBr : Pb Single Crystals". In: *Phys. Status Solidi B Basic Res.* 205 (2000), pp. 205–214. ISSN: 0370-1972.

[53] Chris De Weerd et al. "Hybridization of Single Nanocrystals of Cs_4PbBr_6 and $CsPbBr_3$". In: *J. Phys. Chem. C* 121.35 (2017), pp. 19490–19496. ISSN: 1932-7455. DOI: 10.1021/acs.jpcc.7b05752.

[54] Li Na Quan et al. "Highly Emissive Green Perovskite Nanocrystals in a Solid State Crystalline Matrix". In: *Adv. Mater.* 29.21 (2017), pp. 1–6. ISSN: 1521-4095. DOI: 10.1002/adma.201605945.

[55] Xiaomei Chen et al. "Centimeter-Sized Cs_4PbBr_6 Crystals with Embedded $CsPbBr_3$ Nanocrystals Showing Superior Photoluminescence: Nonstoichiometry Induced Transformation and Light-Emitting Applications". In: *Adv. Funct. Mater.* 28.16 (2018), pp. 1–7. ISSN: 1616-3028. DOI: 10.1002/adfm.201706567.

[56] Zhaojun Zhang et al. "Growth, characterization and optoelectronic applications of pure-phase large-area CsPb 2 Br 5 flake single crystals". In: *J. Mater. Chem. C* 6.3 (2018), pp. 446–451. ISSN: 2050-7526. DOI: 10.1039/c7tc04834c.

[57] Mario Cola and Riccardo Riccardi. "Binary Systems Formed by Lead Bromide with (Li, Na, K, Rb, Cs and Tl) Br: a DTA and Diffractometric Study". In: *Zeitschrift für Naturforsch. A* 26 (1971), p. 1328. ISSN: 1865-7109. DOI: 10.1515/zna-1971-0812.

[58] Olga Nazarenko et al. "Luminescent and Photoconductive Layered Lead Halide Perovskite Compounds Comprising Mixtures of Cesium and Guanidinium Cations". In: *Inorg. Chem.* 56.19 (2017), pp. 11552–11564. ISSN: 1520-510X. DOI: 10.1021/acs.inorgchem.7b01204.

[59] Quinten A. Akkerman and Liberato Manna. "What Defines a Halide Perovskite?" In: *ACS Energy Lett.* 5.2 (Feb. 2020), pp. 604–610. ISSN: 2380-8195. DOI: 10.1021/acsenergylett.0c00039.

[60] Joachim Breternitz and Susan Schorr. "What Defines a Perovskite?" In: *Adv. Energy Mater.* 8.34 (2018), pp. 1–2. ISSN: 1614-6840. DOI: 10.1002/aenm.201802366.

[61] Quinten A. Akkerman et al. "Solution Synthesis Approach to Colloidal Cesium Lead Halide Perovskite Nanoplatelets with Monolayer-Level Thickness Control". In: *J. Am. Chem. Soc.* 138.3 (2016), pp. 1010–1016. ISSN: 1520-5126. DOI: 10.1021/jacs.5b12124.

[62] Makhsud I. Saidaminov et al. "Pure Cs_4PbBr_6: Highly Luminescent Zero-Dimensional Perovskite Solids". In: *ACS Energy Lett.* 1.4 (2016), pp. 840–845. ISSN: 2380-8195. DOI: 10.1021/acsenergylett.6b00396.

[63] Haihua Zhang et al. “Pure zero-dimensional Cs_4PbBr_6 single crystal rhombohedral microdisks with high luminescence and stability”. In: *Phys. Chem. Chem. Phys.* 19.43 (2017), pp. 29092–29098. ISSN: 1463-9076. DOI: 10.1039/c7cp06097a.

[64] Yuhai Zhang et al. “Zero-Dimensional Cs_4PbBr_6 Perovskite Nanocrystals”. In: *J. Phys. Chem. Lett.* 8.5 (2017), pp. 961–965. ISSN: 1948-7185. DOI: 10.1021/acs.jpclett.7b00105.

[65] Sudipta Seth and Anunay Samanta. “Photoluminescence of Zero-Dimensional Perovskites and Perovskite-Related Materials”. In: *J. Phys. Chem. Lett.* 9.1 (2018), pp. 176–183. ISSN: 1948-7185. DOI: 10.1021/acs.jpclett.7b02931.

[66] Ji-Hyun Hyun Cha et al. “Photoresponse of $CsPbBr_3$ and Cs4$PbBr_6$ Perovskite Single Crystals”. In: *J. Phys. Chem. Lett.* 8.3 (2017), pp. 565–570. ISSN: 1948-7185. DOI: 10.1021/acs.jpclett.6b02763.

[67] Dan Han et al. “Unraveling luminescence mechanisms in zero-dimensional halide perovskites”. In: *J. Mater. Chem. C* 6.24 (2018), pp. 6398–6405. ISSN: 2050-7526. DOI: 10.1039/c8tc01291a.

[68] Jun Yin et al. “Point Defects and Green Emission in Zero-Dimensional Perovskites”. In: *J. Phys. Chem. Lett.* 9.18 (2018), pp. 5490–5495. ISSN: 1948-7185. DOI: 10.1021/acs.jpclett.8b02477.

[69] Sudipta Seth and Anunay Samanta. “Fluorescent Phase-Pure Zero-Dimensional Perovskite-Related Cs_4PbBr_6 Microdisks: Synthesis and Single-Particle Imaging Study”. In: *J. Phys. Chem. Lett.* 8.18 (2017), pp. 4461–4467. ISSN: 1948-7185. DOI: 10.1021/acs.jpclett.7b02100.

[70] Daqin Chen et al. “Large-scale room-temperature synthesis and optical properties of perovskite-related Cs_4PbBr_6 fluorophores”. In: *J. Mater. Chem. C* 4.45 (2016), pp. 10646–10653. ISSN: 2050-7526. DOI: 10.1039/c6tc04036e. URL: http://xlink.rsc.org/?DOI=C6TC04036E.

[71] Michele De Bastiani et al. “Inside Perovskites: Quantum Luminescence from Bulk Cs_4PbBr_6 Single Crystals”. In: *Chem. Mater.* 29.17 (2017), pp. 7108–7113. ISSN: 1520-5002. DOI: 10.1021/acs.chemmater.7b02415.

[72] Emma R. Dohner et al. “Intrinsic white-light emission from layered hybrid perovskites”. In: *J. Am. Chem. Soc.* 136.38 (2014), pp. 13154–13157. ISSN: 1520-5126. DOI: 10.1021/ja507086b.

[73] Zhao Yuan et al. “One-dimensional organic lead halide perovskites with efficient bluish white-light emission”. In: *Nat. Commun.* 8 (2017). ISSN: 2041-1723. DOI: 10.1038/ncomms14051.

[74] Zhiwei Ma et al. “ Whether or Not Emission of Cs_4PbBr_6 Nanocrystals: High-Pressure Experimental Evidence ”. In: *CCS Chem.* 2.2 (2020), pp. 71–80. ISSN: 2096-5745. DOI: 10.31635/ccschem.020.201900086.

[75] Kun Hua Wang et al. “Large-Scale Synthesis of Highly Luminescent Perovskite-Related $CsPb_2Br_5$ Nanoplatelets and Their Fast Anion Exchange”. In: *Angew. Chemie - Int. Ed.* 55.29 (2016), pp. 8328–8332. ISSN: 1521-3773. DOI: 10.1002/anie.201602787.

[76] Haoze Yang et al. "Room-Temperature Engineering of All-Inorganic Perovskite Nanocrsytals with Different Dimensionalities". In: *Chem. Mater.* 29.21 (2017), pp. 8978–8982. ISSN: 1520-5002. DOI: 10.1021/acs.chemmater.7b04161.

[77] Xiaosheng Tang et al. "Perovskite $CsPb_2Br_5$ Microplate Laser with Enhanced Stability and Tunable Properties". In: *Adv. Opt. Mater.* 5.3 (2017), pp. 1–8. ISSN: 2195-1071. DOI: 10.1002/adom.201600788.

[78] Pengzhi Li et al. "Novel synthesis and optical characterization of $CsPb_2Br_5$ quantum dots in borosilicate glasses". In: *Mater. Lett.* 209 (2017), pp. 483–485. ISSN: 0167-577X. DOI: 10.1016/j.matlet.2017.08.079.

[79] Pengzhi Li et al. "Photoluminescence properties and device application of $CsPb_2Br_5$ quantum dots in glasses". In: *Mater. Res. Bull.* 105.April (2018), pp. 63–67. ISSN: 0025-5408. DOI: 10.1016/j.materresbull.2018.04.028.

[80] Guopeng Li et al. "Shape and phase evolution from $CsPbBr_3$ perovskite nanocubes to tetragonal $CsPb_2Br_5$ nanosheets with an indirect bandgap". In: *Chem. Commun.* 52.75 (2016), pp. 11296–11299. ISSN: 1364-548X. DOI: 10.1039/c6cc05877a.

[81] Jing Li et al. "Synthesis of all-inorganic $CsPb_2Br_5$ perovskite and determination of its luminescence mechanism". In: *RSC Adv.* 7.85 (2017), pp. 54002–54007. ISSN: 2046-2069. DOI: 10.1039/c7ra10693a.

[82] Bo Qiao et al. "Water-resistant, monodispersed and stably luminescent $CsPbBr_3/CsPb_2Br_5$ core-shell-like structure lead halide perovskite nanocrystals". In: *Nanotechnology* 28 (2017), p. 445602. ISSN: 1361-6528. DOI: 10.1088/1361-6528/aa892e.

[83] Yichuan Ling et al. "Composite Perovskites of Cesium Lead Bromide for Optimized Photoluminescence". In: *J. Phys. Chem. Lett.* 8.14 (2017), pp. 3266–3271. ISSN: 1948-7185. DOI: 10.1021/acs.jpclett.7b01302.

[84] Guoqing Tong et al. "Dual-Phase $CsPbBr_3$–$CsPb_2Br_5$ Perovskite Thin Films via Vapor Deposition for High-Performance Rigid and Flexible Photodetectors". In: *Small* 14.7 (2018), pp. 1–8. ISSN: 1613-6829. DOI: 10.1002/smll.201702523.

[85] Junwei Xu et al. "Imbedded Nanocrystals of $CsPbBr_3$ in Cs_4PbBr_6: Kinetics, Enhanced Oscillator Strength, and Application in Light-Emitting Diodes". In: *Adv. Mater.* 29.43 (2017), pp. 1–10. ISSN: 1521-4095. DOI: 10.1002/adma.201703703.

[86] Yeshu Tan et al. "Ultrastable and Reversible Fluorescent Perovskite Films Used for Flexible Instantaneous Display". In: 1900730 (2019), pp. 1–9. DOI: 10.1002/adfm.201900730.

[87] Diego Di Girolamo et al. "Dual effect of humidity on cesium lead bromide: Enhancement and degradation of perovskite films". In: *J. Mater. Chem. A* 7.19 (2019), pp. 12292–12302. ISSN: 2050-7496. DOI: 10.1039/c9ta00715f.

[88] G Bergerhoff, I D Brown, F Allen, et al. "Crystallographic databases". In: *Int. Union Crystallogr. Chester* 360 (1987), pp. 77–95.

[89] Harold P. Klug and Leroy E. Alexander. *X-ray diffraction procedures for polyerystalline and amorphous materials*. Second. Wiley, 1974.

[90] Jeremy Karl Cockcroft and Paul Barnes. *Course Index for Powder Diffraction on the Web*. 2006. URL: http://pd.chem.ucl.ac.uk/pd/indexnn.htm.

[91] Harvey Guthrey and John Moseley. "A Review and Perspective on Cathodoluminescence Analysis of Halide Perovskites". In: *Adv. Energy Mater.* 1903840 (2020), pp. 1–33. ISSN: 1614-6840. DOI: 10.1002/aenm.201903840.

[92] Felix Vietmeyer et al. "Carrier recombination dynamics in individual CdSe nanowires". In: *Phys. Rev. B - Condens. Matter Mater. Phys.* 83.11 (2011), pp. 1–10. ISSN: 1098-0121. DOI: 10.1103/PhysRevB.83.115319.

[93] Jacques I. Pankove. *Optical Processes in Semiconductors*. New York: Dover Publications, Inc., 1975. ISBN: 0-486-60275-3.

[94] Thomas Kirchartz et al. "Photoluminescence-Based Characterization of Halide Perovskites for Photovoltaics". In: *Adv. Energy Mater.* 1904134 (2020), p. 1904134. DOI: 10.1002/aenm.201904134.

[95] T. Schmidt, K. Lischka, and W. Zulehner. "Excitation-power dependence of the near-band-edge photoluminescence of semiconductors". In: *Phys. Rev. B* 45.16 (1992), pp. 8989–8994. ISSN: 0163-1829. DOI: 10.1103/PhysRevB.45.8989.

[96] Jaesun Lee et al. "Room-temperature band-edge photoluminescence from cadmium telluride". In: *Phys. Rev. B* 49.3 (1994), pp. 1668–1676. ISSN: 0163-1829. DOI: 10.1103/PhysRevB.49.1668.

[97] Joseph I. Goldstein et al. *Scanning Electron Microscopy and X-ray Microanalysis*. New York: Springer, 2017.

[98] B. G. Yacobi and D. B. Holt. *Cathodoluminescence Microscopy of Inorganic Solids*. 1. 1990, pp. 1–289. ISBN: 978-1-4757-9597-4. DOI: 10.1007/978-1-4757-9595-0.

[99] E Abbe. "Beiträge zur Theorie des Mikroskops und der mikroskopischen Wahrnehmung". In: *Arch. für Mikroskopische Anat.* 9.1 (1873), pp. 413–468. ISSN: 0176-7364. DOI: 10.1007/BF02956173.

[100] T.E. Everhart and P.H. Hoff. "Determination of Kilovolt Electron Energy Dissipation vs Penetration Distance in Solid Materials". In: *J. Appl. Phys.* 42.13 (1971), pp. 5837–5846. DOI: 10.1063/1.1660019.

[101] Daniel Abou-Ras, Thomas Kirchartz, and Uwe Rau. *Advanced Characterization Techniques for Thin Film Solar Cells: Second Edition*. Ed. by Daniel Abou-Ras, Thomas Kirchartz, and Uwe Rau. Vol. 1-2. WILEY-VCH Verlag, 2016, pp. 1–681. ISBN: 9783527699025. DOI: 10.1002/9783527699025.

[102] D D Perovic et al. "Field-emission SEM imaging of compositional and doping layer semiconductor superlattices". In: *Ultramicroscopy* 58.1 (1995), pp. 104–113. ISSN: 0304-3991. DOI: 10.1016/0304-3991(94)00183-N.

[103] E. Rutherford. " LXXIX. The scattering of α and β particles by matter and the structure of the atom ". In: *London, Edinburgh, Dublin Philos. Mag. J. Sci.* 21.125 (1911), pp. 669–688. ISSN: 1941-5982. DOI: 10.1080/14786440508637080.

[104] Heiner Jaksch. "Strain related Contrast mechanisms in crystalline materials imaged with AsB detection BT - EMC 2008 14th European Microscopy Congress 1–5 September 2008, Aachen, Germany". In: ed. by Martina Luysberg, Karsten Tillmann, and Thomas Weirich. Berlin, Heidelberg: Springer Berlin Heidelberg, 2008, pp. 553–554. ISBN: 978-3-540-85156-1.

[105] J.-L. MAURICE and Y. MARFAING. *Theoretical Study of High Injection Effects in Ebic Measurements of Grain Boundary Recombination Velocity in Silicon*. 1991. DOI: 10.1051/jp4:1991614.

[106] Daniel Abou-Ras and Thomas Kirchartz. "Electron-Beam-Induced Current Measurements of Thin-Film Solar Cells". In: *ACS Appl. Energy Mater.* 2.9 (2019), pp. 6127–6139. ISSN: 2574-0962. DOI: 10.1021/acsaem.9b01172.

[107] Pietro Caprioglio et al. "Nano-emitting heterostructures violate optical reciprocity and enable efficient photoluminescence in halide-segregated MA-free wide bandgap perovskites". In: *Submitted to Nat. Photonics* (2020).

[108] Connor Gregory and Connor Gregory Bischak. "Elucidating Heterogeneities and Dynamic Processes at the Nanoscale with Cathodoluminescence and Cathodoluminescence-Activated Microscopies". PhD thesis. UC Berkeley, 2017.

[109] Sebastián Caicedo-Dávila et al. "Spatial Phase Distributions in Solution-Based and Evaporated Cs–Pb–Br Thin Films". In: *J. Phys. Chem. C* 123.29 (July 2019), pp. 17666–17677. ISSN: 1932-7447. DOI: 10.1021/acs.jpcc.9b02567.

[110] Sebastián Caicedo-Dávila et al. "Effect of Post-deposition Annealing on the Luminescence of Mixed-phase $CsPb_2Br_5$/$CsPbBr_3$ Thin Films". In: *J. Phys. Chem. C* 124.36 (Sept. 2020), pp. 19514–19521. DOI: 10.1021/acs.jpcc.0c06955.

[111] Louis Brus. "Electronic wave functions in semiconductor clusters: Experiment and theory". In: *J. Phys. Chem.* 90.12 (1986), pp. 2555–2560. ISSN: 0022-3654. DOI: 10.1021/j100403a003.

[112] Al. L. Efros and M. Rosen. "NANOCRYSTALS, THE ELECTRONIC STRUCTURE OF SEMICONDUCTOR". In: *Annu. Rev. Mater. Sci.* 30 (2000), pp. 475–521.

[113] L Bányai and S W Koch. *Semiconductor Quantum Dots*. Vol. Volume 2. WORLD SCIENTIFIC, May 1993, p. 256. ISBN: 978-981-02-1390-9. DOI: 10.1142/2019.

[114] L. V. Keldysh. "Coulomb interaction in thin semiconductir and semimetal films". In: *Pis'ma Zh. Eksp. Teor. Fiz.* 29.11 (1979), pp. 716–719. URL: http://www.jetpletters.ac.ru/ps/1458/article%7B%5C_%7D22207.pdf.

[115] V S Dneprovskii et al. "Linear and nonlinear excitonic absorption in semiconducting quantum wires crystallized in a dielectric matrix". In: *J. Exp. Theor. Phys.* 87.2 (1998), pp. 382–387. ISSN: 1090-6509. DOI: 10.1134/1.558671.

[116] E A Muljarov et al. "Dielectrically enhanced excitons in semiconductor-insulator quantum wires: Theory and experiment". In: *Phys. Rev. B* 62.11 (Sept. 2000), pp. 7420–7432. DOI: 10.1103/PhysRevB.62.7420.

[117] L D Landau and E M Lifshits. *Electrodynamics of continuous media*. Translated from the Russian by J.B. Sykes and J.S. Bell. Oxford; New York: Pergamon Press, 1960.

[118] John David Jackson. *Classical electrodynamics*. Third edition. New York : Wiley, [1999] ©1999, 1962.

[119] Bert Conings et al. "Intrinsic Thermal Instability of Methylammonium Lead Trihalide Perovskite". In: *Adv. Energy Mater.* 5.15 (2015), pp. 1–8. ISSN: 1614-6840. DOI: 10.1002/aenm.201500477.

[120] Yue-Yu Zhang et al. "Intrinsic Instability of the Hybrid Halide Perovskite Semiconductor $CH_3NH_3PbI_3$". In: *Chinese Phys. Lett.* 35.3 (Mar. 2018), p. 036104. ISSN: 0256-307X. DOI: 10.1088/0256-307X/35/3/036104.

[121] G. Kresse and J. Furthmüller. "Efficient iterative schemes for ab initio total-energy calculations using a plane-wave basis set". In: *Phys. Rev. B - Condens. Matter Mater. Phys.* 54.16 (1996), pp. 11169–11186. ISSN: 1550-235X. DOI: 10.1103/PhysRevB.54.11169.

[122] John P Perdew, Kieron Burke, and Yue Wang. "Generalized gradient approximation for the exchange-correlation hole of a many-electron system". In: *Phys. Rev. B* 54.23 (1996), pp. 16533–16539. ISSN: 0163-1829. DOI: 10.1103/PhysRevB.54.16533.

[123] Alexandre Tkatchenko and Matthias Scheffler. "Accurate molecular van der Waals interactions from ground-state electron density and free-atom reference data". In: *Phys. Rev. Lett.* 102.7 (2009), pp. 6–9. ISSN: 0031-9007. DOI: 10.1103/PhysRevLett.102.073005.

[124] Tomáš Bučko et al. "Improved density dependent correction for the description of London dispersion forces". In: *J. Chem. Theory Comput.* 9.10 (2013), pp. 4293–4299. ISSN: 1549-9618. DOI: 10.1021/ct400694h.

[125] Tomáš Bučko et al. "Extending the applicability of the Tkatchenko-Scheffler dispersion correction via iterative Hirshfeld partitioning". In: *J. Chem. Phys.* 141.3 (2014), p. 034114. ISSN: 0021-9606. DOI: 10.1063/1.4890003.

[126] P. E. Blöchl. "Projector augmented-wave method". In: *Phys. Rev. B* 50.24 (1994), pp. 17953–17979. ISSN: 0163-1829. DOI: 10.1103/PhysRevB.50.17953.

[127] D. Kresse, G.; Joubert. "From ultrasoft pseudopotentials to the projector augmented-wave method". In: *Phys. Rev. B - Condens. Matter Mater. Phys.* 59.3 (1999), pp. 1758–1775. ISSN: 1550-235X. DOI: 10.1103/PhysRevB.59.1758.

[128] Tomáš Bučko, Jürgen Hafner, and János G. Ángyán. "Geometry optimization of periodic systems using internal coordinates". In: *J. Chem. Phys.* 122.12 (2005), p. 124508. ISSN: 0021-9606. DOI: 10.1063/1.1864932.

[129] Francisco Palazon et al. "Mechanochemical synthesis of inorganic halide perovskites: Evolution of phase-purity, morphology, and photoluminescence". In: *J. Mater. Chem. C* 7.37 (2019), pp. 11406–11410. ISSN: 2050-7526. DOI: 10.1039/c9tc03778k.

[130] M Rodová, J Brožek, and K. Nitsch. "Phase transitions in ternary caesium lead bromide". In: *J. Therm. Anal.* 71.62 (2003), pp. 667–673. ISSN: 1388-6150. DOI: 10.1023/A:1022836800820.

[131] Eugen Posnjak and Ralph W G Wyckoff. "The crystal structures of the alkali halides. II". In: *J. Washingt. Acad. Sci.* 12.10 (May 1922), pp. 248–251. ISSN: 0043-0439. URL: http://www.jstor.org/stable/24532679.

[132] Wheeler P Davey. "The Absolute Sizes of Certain Monovalent and Bivalent Ions". In: *Phys. Rev.* 19.3 (1922), pp. 248–251. DOI: 10.1103/PhysRev.19.248.2.

[133] Dandan Zhang et al. "Solution-Phase Synthesis of Cesium Lead Halide Perovskite Nanowires". In: *J. Am. Chem. Soc.* 137.29 (2015), pp. 9230–9233. ISSN: 1520-5126. DOI: 10.1021/jacs.5b05404. eprint: 0402594v3.

[134] Wenkang Wang et al. "$CsPbBr_3/Cs_4PbBr_6$ Nanocomposites: Formation Mechanism, Large-scale and Green Synthesis, and Application in White Light-Emitting Diodes". In: *Cryst. Growth Des.* 18 (2018), pp. 6133–6141. ISSN: 1528-7505. DOI: 10.1021/acs.cgd.8b01013.

[135] Sunqi Lou et al. "Chemical Transformation of Lead Halide Perovskite into Insoluble, Less Cytotoxic, and Brightly Luminescent $CsPbBr_3/CsPb_2Br_5$ Composite Nanocrystals for Cell Imaging". In: *ACS Appl. Mater. Interfaces* 11.27 (2019), pp. 24241–24246. ISSN: 1944-8252. DOI: 10.1021/acsami.9b05484.

[136] Alexandra J. Ramadan et al. "Revealing the Stoichiometric Tolerance of Lead Trihalide Perovskite Thin Films". In: *Chem. Mater.* 32.1 (2020), pp. 114–120. ISSN: 1520-5002. DOI: 10.1021/acs.chemmater.9b02639.

[137] David Nečas and Petr Klapetek. "Gwyddion: An open-source software for SPM data analysis". In: *Cent. Eur. J. Phys.* 10.1 (2012), pp. 181–188. ISSN: 1895-1082. DOI: 10.2478/s11534-011-0096-2.

[138] J.J.M. Binsma, L.J. Giling, and J. Bloem. "Luminescence of $CuInS_2$". In: *J. Lumin.* 27 (1982), pp. 35–53.

[139] Thomas F Kelly et al. "Atom Probe Tomography of Electronic Materials". In: *Annu. Rev. Mater. Res.* 37.1 (2007), pp. 681–727. DOI: 10.1146/annurev.matsci.37.052506.084239.

[140] Pierre Villars and Karin Cenzual, eds. *$CsPb_2Br_5$ Crystal Structure: Datasheet from "PAULING FILE Multinaries Edition – 2012" in SpringerMaterials.* URL: https://materials.springer.com/isp/crystallographic/docs/sd%7B%5C%%7D7B%7B%5C%%7D5C%7B%5C_%7D%7B%5C%%7D7D1818160.

[141] Ling Yi Huang and Walter R.L. Lambrecht. "Electronic band structure, phonons, and exciton binding energies of halide perovskites $CsSnCl_3$, $CsSnBr_3$, and $CsSnI_3$". In: *Phys. Rev. B - Condens. Matter Mater. Phys.* 88.16 (2013), pp. 1–12. ISSN: 1098-0121. DOI: 10.1103/PhysRevB.88.165203.

[142] M. Sebastian et al. "Excitonic emissions and above-band-gap luminescence in the single-crystal perovskite semiconductors $CsPbBr_3$ and $CsPbCl_3$". In: *Phys. Rev. B - Condens. Matter Mater. Phys.* 92.23 (2015), pp. 1–9. ISSN: 1550-235X. DOI: 10.1103/PhysRevB.92.235210.

[143] C. J. Glassbrenner and Glen A. Slack. “Thermal conductivity of silicon and germanium from 3°K to the melting point”. In: *Phys. Rev.* 134.4A (1964), A1058–A1069. ISSN: 0031-899X. DOI: 10.1103/PhysRev.134.A1058.

[144] Hugh D Young and Francis Weston Sears. *University physics.* English. Reading, Mass.: Addison-Wesley Pub. Co., 1992. ISBN: 0201196514 9780201196511.

[145] Young Kwang Jung et al. “Intrinsic doping limit and defect-assisted luminescence in Cs_4PbBr_6”. In: *J. Mater. Chem. A* 7.35 (2019), pp. 20254–20261. ISSN: 2050-7496. DOI: 10.1039/c9ta06874k.

[146] Jun Yin et al. “Intrinsic Lead Ion Emissions in Zero-Dimensional Cs_4PbBr_6 Nanocrystals”. In: *ACS Energy Lett.* 2.12 (2017), pp. 2805–2811. ISSN: 2380-8195. DOI: 10.1021/acsenergylett.7b01026.

[147] Nicolas Riesen et al. “On the origins of the green luminescence in the "zero-dimensional perovskite" Cs_4PbBr_6: Conclusive results from cathodoluminescence imaging”. In: *Nanoscale* 11.9 (2019), pp. 4001–4007. ISSN: 2040-3372. DOI: 10.1039/c8nr09255a.

[148] Chr. K. Moller. “The Structure Of Perovskite-Like Cæsium Plumbo Trihalides”. In: *Mat. Fys. Medd. Dan. Vid. Selsk* 32.2 (1959).

[149] A Le Bail, H Duroy, and J L Fourquet. “Ab-initio structure determination of $LiSbWO_6$ by X-ray powder diffraction”. In: *Mater. Res. Bull.* 23.3 (1988), pp. 447–452. ISSN: 0025-5408. DOI: 10.1016/0025-5408(88)90019-0.

[150] R. A. Varin, J. Bystrzycki, and A. Calka. “Effect of annealing on the microstructure, ordering and microhardness of ball milled cubic ($L1_2$) titanium trialuminide intermetallic powder”. In: *Intermetallics* 7.7 (1999), pp. 785–796. ISSN: 0966-9795. DOI: 10.1016/S0966-9795(98)00127-7.

[151] G. Caglioti, A. Paoletti, and F. P. Ricci. “Choice of collimators for a crystal spectrometer for neutron diffraction”. In: *Nucl. Instruments* 3.4 (1958), pp. 223–228. ISSN: 0369-643X. DOI: 10.1016/0369-643X(58)90029-X.

[152] G. K. Williamson and W. H. Hall. “X-ray line broadening from filed Aluminium and Wolfram”. In: *Acta Metall.* 1.1 (1953), pp. 22–31. ISSN: 0001-6160. DOI: 10.1016/0001-6160(53)90006-6.

[153] M. Nikl et al. “Photoluminescence and decay kinetics of CsPbCl3 single crystals”. In: *Chem. Phys. Lett.* 220.1-2 (1994), pp. 14–18. ISSN: 0009-2614. DOI: 10.1016/0009-2614(94)00127-8.

[154] Jüri Krustok, Heikki Collan, and Kari Hjelt. “Does the low-temperature Arrhenius plot of the photoluminescence intensity in CdTe point towards an erroneous activation energy?” In: *J. Appl. Phys.* 81.3 (1997), pp. 1442–1445. ISSN: 0021-8979. DOI: 10.1063/1.363903.

[155] Christoph Wolf and Tae Woo Lee. “Exciton and lattice dynamics in low-temperature processable $CsPbBr_3$ thin-films”. In: *Mater. Today Energy* 7 (2018), pp. 199–207. ISSN: 2468-6069. DOI: 10.1016/j.mtener.2017.09.010.

[156] Pierre Villars and Karin Cenzual, eds. *$CsPbBr_3$ Crystal Structure: Datasheet from “PAULING FILE Multinaries Edition – 2012” in SpringerMaterials.* URL: https://materials.springer.com/isp/crystallographic/docs/sd%7B%5C_%7D0545372.

[157] Loredana Protesescu et al. "Nanocrystals of Cesium Lead Halide Perovskites ($CsPbX_3$, X = Cl, Br, and I): Novel Optoelectronic Materials Showing Bright Emission with Wide Color Gamut". In: *Nano Lett.* 15.6 (2015), pp. 3692–3696. ISSN: 1530-6992. DOI: 10.1021/nl5048779.

[158] Pierre Villars and Karin Cenzual, eds. *Cs_4PbBr_6 Crystal Structure: Datasheet from "PAULING FILE Multinaries Edition – 2012" in SpringerMaterials.* URL: https://materials.springer.com/isp/crystallographic/docs/sd%7B%5C_%7D1602012.

[159] Masami Kumagai and Toshihide Takagahara. "Excitonic and nonlinear-optical properties of dielectric quantum-well structures". In: *Phys. Rev. B* 40.18 (1989), pp. 12359–12381. ISSN: 0163-1829. DOI: 10.1103/PhysRevB.40.12359.

[160] P. G. Bolcatto and C. R. Proetto. "Shape and dielectric mismatch effects in semiconductor quantum dots". In: *Phys. Rev. B - Condens. Matter Mater. Phys.* 59.19 (1999), pp. 12487–12498. ISSN: 1550-235X. DOI: 10.1103/PhysRevB.59.12487.

[161] J. L. Movilla and J. Planelles. "Image charges in spherical quantum dots with an off-centered impurity: Algorithm and numerical results". In: *Comput. Phys. Commun.* 170.2 (2005), pp. 144–152. ISSN: 0010-4655. DOI: 10.1016/j.cpc.2005.03.109.

[162] Josep Planelles. "Simple correlated wave-function for excitons in 0D, quasi-1D and quasi-2D quantum dots". In: *Theor. Chem. Acc.* 136.7 (2017), pp. 1–16. ISSN: 1432-881X. DOI: 10.1007/s00214-017-2107-x.

[163] Fernando Rajadell, Juan I. Climente, and Josep Planelles. "Excitons in core-only, core-shell and core-crown CdSe nanoplatelets: Interplay between in-plane electron-hole correlation, spatial confinement, and dielectric confinement". In: *Phys. Rev. B* 96.3 (2017), pp. 1–10. ISSN: 2469-9969. DOI: 10.1103/PhysRevB.96.035307.

[164] T. Takagahara. "Effects of dielectric confinement and electron-hole exchange interaction on excitonic states in semiconductor quantum dots". In: *Phys. Rev. B* 47.8 (1993), pp. 4569–4584. ISSN: 0163-1829. DOI: 10.1103/PhysRevB.47.4569.

[165] P. G. Bolcatto and C. R. Proetto. "Partially confined excitons in semiconductor nanocrystals with a finite size dielectric interface". In: *J. Phys. Condens. Matter* 13.2 (2001), pp. 319–334. ISSN: 0953-8984. DOI: 10.1088/0953-8984/13/2/309.

[166] F. Rajadell et al. "Theory of dielectrically induced surface excitonic states in spherical quantum dots". In: *Phys. Rev. B - Condens. Matter Mater. Phys.* 76.11 (2007), pp. 1–5. ISSN: 1098-0121. DOI: 10.1103/PhysRevB.76.115312.

[167] M. Gajdoš et al. "Linear optical properties in the projector-augmented wave methodology". In: *Phys. Rev. B - Condens. Matter Mater. Phys.* 73.4 (2006), pp. 1–9. ISSN: 1098-0121. DOI: 10.1103/PhysRevB.73.045112.

[168] Gerald. Bastard. *Wave mechanics applied to semiconductor heterostructures.* English. Les Ulis Cedex, France; New York, N.Y.: Les Editions de Physique ; Halsted Press, 1988.

[169] M. Royo et al. "Dielectric confinement of excitons in type-I and type-II semiconductor nanorods". In: *J. Phys. Condens. Matter* 23.1 (2011). ISSN: 09538984. DOI: 10.1088/0953-8984/23/1/015301.

[170] Gregory H. Wannier. "The structure of electronic excitation levels in insulating crystals". In: *Phys. Rev.* 52.3 (1937), pp. 191–197. ISSN: 0031-899X. DOI: 10.1103/PhysRev.52.191.

[171] Sangyeon Cho and Seok Hyun Yun. "Structure and optical properties of perovskite-embedded dual-phase microcrystals synthesized by sonochemistry". In: *Commun. Chem.* 3.1 (2020). ISSN: 2399-3669. DOI: 10.1038/s42004-020-0265-6.

[172] Peter C. Sercel et al. "Exciton Fine Structure in Perovskite Nanocrystals". In: *Nano Lett.* 19.6 (2019), pp. 4068–4077. ISSN: 1530-6992. DOI: 10.1021/acs.nanolett.9b01467.

[173] Lucy D. Whalley et al. "Impact of nonparabolic electronic band structure on the optical and transport properties of photovoltaic materials". In: *Phys. Rev. B* 99.8 (2019), pp. 1–11. ISSN: 2469-9969. DOI: 10.1103/PhysRevB.99.085207.

[174] Claude A. Klein. "Bandgap dependence and related features of radiation ionization energies in semiconductors". In: *J. Appl. Phys.* 39.4 (1968), pp. 2029–2038. ISSN: 0021-8979. DOI: 10.1063/1.1656484.

[175] W Ehrenberg and D. J. Gibbons. *Electron bombardment induced conductivity and its applications*. Academic Press, 1981, p. 348. ISBN: 9780122333507. URL: https://inis.iaea.org/search/search.aspx?orig%7B%5C_%7Dq=RN:15068855.

[176] H.-J. Hunger, L Küchler, and Short Notes. "Measurements of the electron backscattering coefficient for quantitative EPMA in the energy range of 4 to 40 keV". In: *Phys. status solidi* 56.1 (1979), K45–K48. DOI: 10.1002/pssa.2210560157.

[177] Charles Kittel. *Introduction to Solid State Physics*. 8th ed. Vol. 8th editio. John Wiley & Sons, Inc., 1995. ISBN: 0471111813.

[178] John H Davies. *The Physics of Low-dimensional Semiconductors: An Introduction*. Cambridge University Press, 1997. DOI: 10.1017/CBO9780511819070.

[179] Attila Szabo and Neil S Ostlund. *Modern quantum chemistry: introduction to advanced electronic structure theory*. Courier Corporation, 2012.

[180] Peter Y. Yu and Manuel Cardona. *Fundamentals of semiconductors*. 4th ed. Springer, 2010. ISBN: 978-3-642-00710-1.

[181] Jacky Even et al. "Importance of spin-orbit coupling in hybrid organic/inorganic perovskites for photovoltaic applications". In: *J. Phys. Chem. Lett.* 4.17 (2013), pp. 2999–3005. ISSN: 1948-7185. DOI: 10.1021/jz401532q.

[182] Wahyu Setyawan and Stefano Curtarolo. "High-throughput electronic band structure calculations: Challenges and tools". In: *Comput. Mater. Sci.* 49.2 (2010), pp. 299–312. ISSN: 0927-0256. DOI: 10.1016/j.commatsci.2010.05.010.

[183] Center for Autonomous Materials Design. *AFLOW: Automatic-FLOW for materials discovery*. URL: http://materials.duke.edu/awrapper.html.

A

Electron-hole generation in cathodoluminescence

Assuming that backscattered electrons lose a negligible amount of energy when interacting with the sample, the amount of electron-hole pairs generated per incident electron can be estimated as:

$$G_{eh} = \frac{E_b(1-\eta)}{E_{eh}} \tag{A.1}$$

where E_b is the electron beam energy, η is the backscattering coefficient, E_{eh} is the energy necessary to generate an electron-hole pair from ionizing radiation, which can be estimated as independent of the beam energy and as a function of the band gap using a common relationship [98, 174, 175]

$$E_{eh} = 2.1E_g + 1.3 \tag{A.2}$$

where E_g is the band gap of the material. The backscattering coefficient η is the fractional beam energy loss due to backscattered electrons and can be estimated as a function of E_b and the material composition as [176]:

$$\eta = E_b^m c \tag{A.3a}$$

$$m = 0.1382 - \frac{0.9211}{Z^{1/2}} \tag{A.3b}$$

$$c = 0.1904 - 0.2235 \ln Z + 0.1292 \ln Z^2 - 0.01491 \ln Z^3 \tag{A.3c}$$

where Z is the atomic number. A weighted sum of the backscattering coefficients η_i for each element, for a multi-element material can be used for compounds [91].

$$\eta = \sum_i C_i \eta_i \tag{A.4a}$$

$$Ci = \frac{n_i A_i}{\sum_i n_i A_i} \tag{A.4b}$$

where A_i is the atomic weight of element i and c_i its number of atoms per formula unit.

The generation rate per unit volume per second, can be then obtained from G_{eh} in equation A.1 simply by multiplying with the beam current I_b and dividing by the elemental charge e and the interaction volume V [105, 106]:

$$G(E_b, I_b, E_g) = \frac{I_b G_{eh}}{eV} \tag{A.5}$$

In the simplest way, the interaction volume can be estimated using a simple spherical approach, where we calculate the diameter of the interaction sphere from the Gruen penetration depth (equation 3.4) as the diameter of the sphere. If we recall equation 3.3 and the discussion in section 3.2.2, the injection conditions, which depend on the Generation rate G, depend thus in a CL experiment from the beam energy (acceleration voltage) and beam current. Studies of excitation-dependent CL measurements demonstrated that the emission intensity depends on the beam current as a power law [91]:

$$I_{em-CL} \propto I_b^m \tag{A.6}$$

where m varies between 1.0–1.12 for a n-type materials, and between 1.0–1.8 for p-type materials. m values between 1–2 indicate mixed high and low injection conditions, and $m = 1$ indicate low injection conditions. However, for low doped materials, low injection conditions are difficult to achieve, since very high generation rates may be required to get a measurable CL signal.

B

Effective mass and envelope wavefunction approximations

B.1 Effective mass approximation

In a perfect crystal, it can be considered that electrons feel the influence of an average, periodic electrostatic potential $V_{crys}(\mathbf{r}) = V_{crys}(\mathbf{r} + \mathbf{T})$ — where $\mathbf{T}$ is the crystal translation vector — that describe the interaction of the electron with other electrons in the crystal and the nuclei. The wavefunction describing the system is then the solution of the following Schrödinger equation:

$$\left(-\frac{\hbar^2}{2m_0}\nabla^2 + V_{crys}(\mathbf{r})\right)\psi(\mathbf{r}) = E\psi(\mathbf{r}) \tag{B.1}$$

where m_0 is the mass of the electron and E the energy. The solutions to equation B.1 are:

$$\psi(\mathbf{r}) = u_{\mathbf{k}}(\mathbf{r})e^{i\mathbf{k}\cdot\mathbf{r}} \tag{B.2}$$

where $e^{i\mathbf{k}\cdot\mathbf{r}}$ is a plane wave slowly varying along the crystal, and $u_{\mathbf{k}}(\mathbf{r} + \mathbf{T}) = u_{\mathbf{k}}(\mathbf{r})$ is a Bloch function that has the same periodicity as the crystal potential $V_{crys}(\mathbf{r})$ and describes the changes of the wavefunction within the unit cell [177]. Under the assumption that only states from a narrow region in $\mathbf{k}$-space have a significant contribution, the energy near the band edge can be approximated as:

$$E_c(\mathbf{k}) = E_g + \frac{\hbar^2}{2m_e^*} \mid \mathbf{k} \mid^2 \tag{B.3}$$

where $E_c(\mathbf{k})$ is the energy of the conduction band, E_g is the (electronic) band gap of the semiconductor and m_e^* is the Bloch electron effective mass in the crystal. A similar relation can be obtained for the holes in the valence band.

B.2 Envelope function approximation

In confined systems, the dimensions of the confined region is usually large, compared with the lattice constant of the crystal. Therefore, it is reasonable to assume as a first approximation that the changes in the band structure of the confined system is weak [113]. Under this approximation, the wavefunction can be expanded as the product of an envelope function $\chi(\mathbf{r})$ and the Bloch function. A detailed derivation of the wavefunction is elegantly presented by Davies [178]. Here it is sufficient to state that the envelope function can be treated as a localized quasi-particle, and that the system can be described by the Schrödinger equation with an effective Hamiltonian:

$$\left(-\frac{\hbar^2}{2m_e^*}\nabla^2 + V_{ext}(\mathbf{r})\right)\chi(\mathbf{r}) = (E - E_g)\chi(\mathbf{r}) \tag{B.4}$$

where V_{ext} is the external potential, that describes — for instance — the confinement effects. A similar equation can be used to describe the holes.

The simplest approximation to a confined system is the infinite potential well. Assuming a spherical confined nanocrystal, within the effective mass and envelope function approximations, the lowest electron energy of an electron in a crystal confined in an infinite spherical potential quantum well can be solved using a hydrogenic wavefunction, which will not be discussed in detail in this thesis and can be found in several text books (see, for instance Szabo and Ostlund [179]) [113]:

$$E \simeq E_g + \frac{h^2}{8m_e^* r^2} \tag{B.5}$$

where r is the radius of the sphere.

B.3 Excitons in the envelope function approximation

When an electron is excited to the conduction band, and a hole is generated in the valence band, they can form bound electron-hole pairs known as excitons, owing to their mutual Coulomb attraction. One of the simplest models used to study excitons within the effective mass theory is the Wannier-Mott model [170], which solves the exciton envelope wavefunction, $\Phi(\mathbf{R}_e, \mathbf{R}_h)$, from the wave equation [180]:

$$\left[-\frac{\hbar^2}{2m_e^*}\nabla^2_{\mathbf{R}_e} - \frac{\hbar^2}{2m_h^*}\nabla^2_{\mathbf{R}_h} - \frac{e^2}{4\pi\varepsilon\varepsilon_0 \mid \mathbf{R}_e - \mathbf{R}_h \mid}\right]\Phi(\mathbf{R}_e, \mathbf{R}_h) = E_{exc}\Phi(\mathbf{R}_e, \mathbf{R}_h) \tag{B.6}$$

where $m^*_{e/h}$ is the electron/hole effective mass, $\mathbf{R}_{e/h}$ is the electron/hole position, ε is the relative effective dielectric constant, ε_0 is the vacuum permittivity, e is the electron charge and E_{exc} is the exciton energy.

Equation B.6 can be expressed in terms of the center of mass coordinates, $\mathbf{R} = \frac{m_e\mathbf{R}_e + m_h\mathbf{R}_h}{m_e+m)h}$, and the relative position of electron and hole, $\mathbf{r} = \mathbf{R}_e - \mathbf{R}_h$, as a separable equation:

$$-\frac{\hbar^2}{2M}\nabla^2_{\mathbf{R}}\psi(\mathbf{R}) = E_R\psi(\mathbf{R}) \tag{B.7a}$$

$$\left[-\frac{\hbar^2}{2\mu^*}\nabla^2_{\mathbf{r}} - \frac{e^2}{4\pi\varepsilon\varepsilon_0 \mid \mathbf{r} \mid}\right]\phi(\mathbf{r}) = E_r\phi(\mathbf{r}) \tag{B.7b}$$

where $M = m_e + m_h$ and μ^* is the reduced mass of electron and hole:

$$\frac{1}{\mu^*} = \frac{1}{m_e^*} + \frac{1}{m_h^*} \tag{B.8}$$

The solution to equation B.7a is that of a free particle with kinetic energy:

$$E_R = \frac{\hbar^2 K^2}{2M} \tag{B.9}$$

where K is the norm of the wave vector of the particle. On the other hand, equation B.7b can be solved in a similar fashion to equation B.5. Assuming isotropic effective masses, the eigenvalues will depend only on the principal quantum number n, and the solutions to equation B.7b is of the form:

$$E_r = E_{cont} - \frac{\mu^* e^4}{8\varepsilon^2\varepsilon_0^2 h^2 n^2} \tag{B.10}$$

where E_{cont} is the lowest energy of continuum states, which in the case of a semiconductor is the gap energy E_g. Notice that the second term is related to the Coulomb interaction between the electron and hole, and describes the exciton binding energy E_b. The total energy of the exciton is given by:

$$E_{exc} = E_g + \frac{\hbar^2 K^2}{2M} - \frac{\mu^* e^4}{8\varepsilon^2\varepsilon_0^2 h^2 n^2} \tag{B.11}$$

If the transition of interest is that close to the Γ point, the second term in equation B.11 vanishes, and the optical transition energy of the exciton is the difference between the band gap and the exciton binding energy.

C

Band structures and dielectric tensor of Cs–Pb–Br ternary phases

C.1 Band structures of the Cs–Pb–Br ternary phases

Figure C.1 shows the band structures calculated at the PBE and PBE + SOC levels. The band gap calculated at the PBE level is in good agreement with the experimentally measured value for the $CsPbBr_3$ and Cs_4PbBr_6. However, this is a fortuitous agreement, due to a cancellation of errors at the PBE level for halide perovskites [181]. The inclusion of spin-orbit coupling changes reduces the band gap of $CsPbBr_3$ in $\sim 42\%$, that of Cs_4PbBr_6 in $\sim 19\%$ and that of $CsPb_2Br_5$ in $\sim 17\%$. SOC also splits the lower conduction bands and changes the dispersion. These changes are also more pronounced for the $CsPbBr_3$, whose bands become more disperse, and for the Cs_4PbBr_6, whose bands lose dispersion. The bands of $CsPb_2Br_5$ also split, but the band dispersion remains almost unchanged. These results suggest that the influence of spin-orbit coupling on the band structure is related to the dimensionality of the crystal and the Pb coordination, which is very different in the $CsPb_2Br_5$. Although interesting, this phenomenon is out of the scope of the present thesis. It is sufficient to understand that the inclusion of SOC provides reasonable band characteristics, with exception of the band-gap energy, as it has already been shown in the literature [46].

C.2 Anisotropy of the dielectric tensor in Cs–Pb–Br ternary phases

The dielectric tensors of the three Cs–Pb–Br ternary phases are diagonal due to the symmetry of the crystals. Table C.1 summarizes the diagonal elements of the dielectric tensor for all the three phases, calculated with and without spin-orbit coupling. The magnitude of the dielectric constant is not largely affected by the spin-orbit coupling. However, for the $CsPbBr_3$, there is a change in the relative magnitude of the tensor components. For the $CsPb_2Br_5$ the dielectric constant changes only slightly, and that of the Cs_4PbBr_6 does not change at all by including

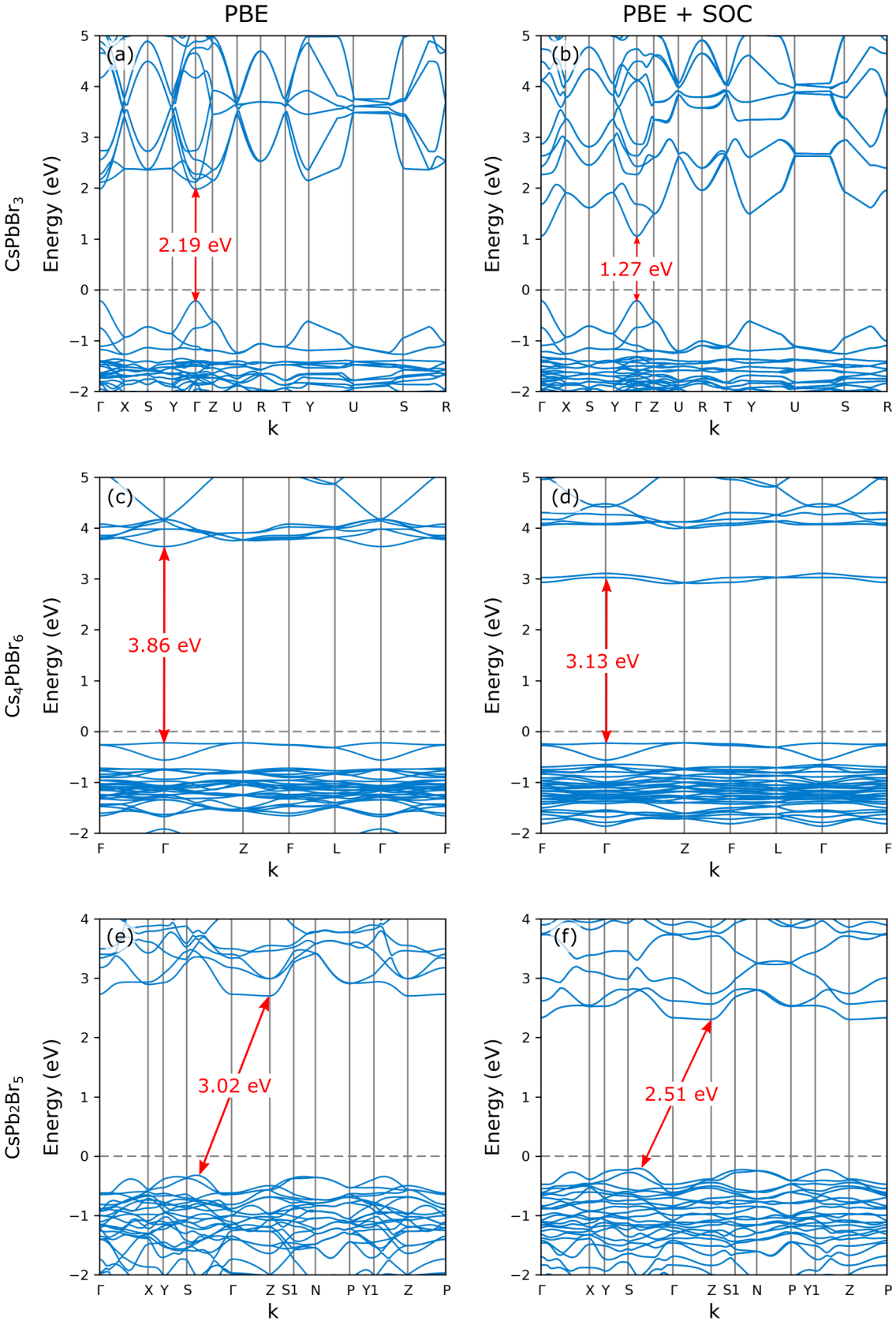

Figure C.1: Band structure of the ternary phases of Cs–Pb–Br, calculated at the PBE (a, c, e) and PBE + SOC (b,d,f) level of theory. Notice that including SOC splits the bands in the conduction band and modifies the dispersion of the conduction bands. The effect is more pronounced for the $CsPbBr_3$ and Cs_4PbBr_6, than for the $CsPb_2Br_5$

SOC. The latter result could be related to the low dispersion of both valence and conduction bands (see Figures C.1c and d), which does not change with SOC. The more disperse bands of $CsPbBr_3$ and $CsPb_2Br_5$ are more affected by the band splitting induced by SOC, especially $CsPbBr_3$. These results emphasize once more the importance of SOC in the calculation of the electronic structure of halide perovskites and related materials, but a more in-depth study is necessary to draw definitive conclusions.

Table C.1: High frequency dielectric tensor (diagonal components) of the three ternary phases of the Cs–Pb–Br system caculated at the PBE and PBE+SOC level

Phase	**PBE**			**PBE + SOC**		
	$\varepsilon^{\infty}_{xx}$	$\varepsilon^{\infty}_{yy}$	$\varepsilon^{\infty}_{zz}$	$\varepsilon^{\infty}_{xx}$	$\varepsilon^{\infty}_{yy}$	$\varepsilon^{\infty}_{zz}$
$CsPbBr_3$	4.2	4.2	4.0	4.1	4.5	4.0
Cs_4PbBr_6	3.1	3.1	3.1	3.1	3.1	3.1
$CsPb_2Br_5$	5.0	5.0	3.7	5.2	5.2	3.8

For $CsPbBr_3$ the dielectric constant is larger in the direction of the b lattice vector (see Figure 6.12)a in the main text), which is the largest one of the orthorhombic structure ($b = 11.75\,\text{Å}$). The second largest dielectric constant is that along the $a = 8.54\,\text{Å}$ lattice vector, and finally that along the $c = 8.06\,\text{Å}$ direction. This suggests that in the $CsPbBr_3$, the polarizability increases as the unit cell is stretched, which results of the octahedra tilting. This phenomena appears to be related to the one described by Kang and Biswas [46], in which the aligned Pb–Br bonds yield large Born effective charges and dielectric constants. On the other hand, the dielectric constant of Cs_4PbBr_6 is isotropic, and can be understood when looking at the primitive cell in Figure 6.12b (obtained as with the AFLOW-online tool [182, 183]). The disjoint octahedra not only reduces the band dispersion, but also hinders the lattice polarization which results in a lower dielectric constant. The orientation of the octahedra relative to one another seems to influence little the dielectric response of the material.

Finally, the $CsPb_2Br_5$ exhibits a strong polarizability in the ab plane, caused by the face-sharing $PbBr_2$ prisms forming planes (see Figure 6.12c). This results is an in-plane dielectric constant that is even larger than that of the $CsPbBr_3$, regardless of the larger band-gap energy. The polarizability in the c direction is closer to that of Cs_4PbBr_6: The discontinuous planes inhibit the lattice polarization in that direction and reduce band dispersion in certain directions (see, for instance Γ–Z or Z–P directions in Figure C.1e and f), which in turn, reduces the dielectric constant in this direction.

D

Quantum and dielectric confinement model: additional results

D.1 Effect of surrounding dielectric on the exciton binding energy for different confinement regimes

Considering the modek with full electron-hole correlation with infinite confinement potential, as described in Section 6.4.3 in the main text, the effect of the dielectric environment was investigated as a function of the well size. The results are plotted in Figure D.1. Note that for $\varepsilon_2 > \varepsilon_1$, quantum confinement has a non-negligible effect on the exciton binding energy in the strong confinement regime ($E_b \simeq 85\,\text{meV}$ when $L_z \simeq 1\,\text{nm}$), while in the moderate and weak confinement regimes, the exciton binding energy is $\sim 60\,\text{meV}$, which is the value reported for bulk $CsPbBr_3$. For $\varepsilon_2 \sim \varepsilon_1$, the effect of confinement on the binding energy is not negligible anymore under the moderate confinement, and it is enhanced in the strong confinement regime, with $E_b \simeq 70 - 160\,\text{meV}$ for $L_z \simeq 6 - 1\,\text{nm}$. Finally, when $\varepsilon_2 < \varepsilon_1$, the binding energy is considerably increased, even in the weak confinement regime, with $E_b \simeq 92\,\text{meV}$ for $L_z \simeq 10\,\text{nm}$, and $E_b \simeq 320\,\text{meV}$ for $L_z \simeq 1\,\text{nm}$, assuming $\varepsilon_2 = 2$.

D.2 Influence of band alignment on the exciton properties

Additional to the effects of confinement discussed in the main text, different types of band alignment and their influence on the emission shift, and the exciton binding energy were investigated. Figure D.2 shows the different types of band alignment modeled. A type I system was modeled by setting the conduction and valence band offsets — ΔE_c and ΔE_v — equal: $\Delta E_c = \Delta E_v = \Delta E_g/2$. A quasi type I system was modeled by setting the conduction band offset as zero, and the adjusting the valence band offset: $\Delta E_c = 0\,\text{eV}$ and $\Delta E_v = \Delta E_g$. Finally, a type II system was modeled by setting a negative conduction band offset, i.e. electrons in the conduction band do not feel confinement on a well, but a potential barrier: $\Delta E_c = -0.1\,\text{eV}$ and $\Delta E_v = \Delta E_g + 0.1\,\text{eV}$.

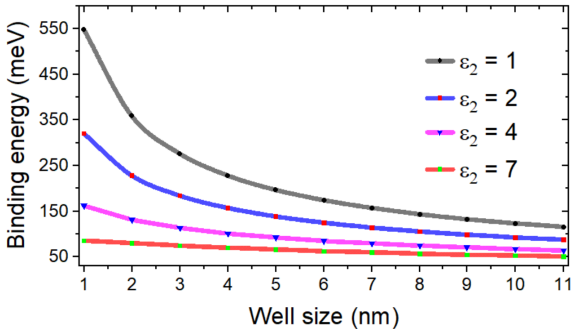

Figure D.1: Calculated exciton binding energy (E_b) for $CsPbBr_3$ nanocrystal, modeled as an infinite potential well, as a function of the well size (L_z). The curves calculated considering different dielectric constants of the surrounding medium (ε_2) are shown. The dielectric constant of $CsPbBr_3$ is assumed as $\varepsilon_1 = 5.0$.

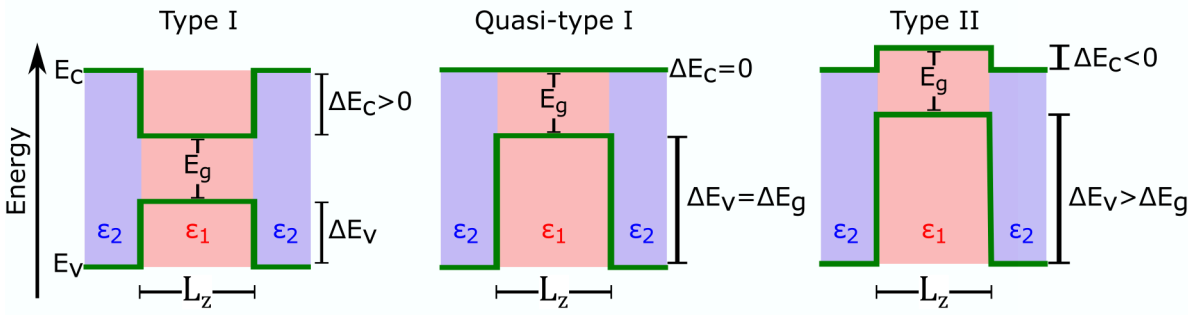

Figure D.2: Three types of band alignment (confinement) are considered. Type I considers effective confinement of the wave functions of the electron and hole, by setting ΔE_v and $\Delta E_c > 0$. Quasi-type I confinement considers a flat conduction band $\Delta E_c = 0$, which results in lost of confinement for the electron. Type II considers a negative potential barrier for the electrons inside the well $\Delta E_c < 0$, which effectively confines electrons to the shell.

D.2.1 $Cs_4PbBr_6/CsPbBr_3/Cs_4PbBr_6$ system

Figure D.3 shows the emission energy and the exciton binding energy as a function of the well size for different types of band alignment. The first interesting feature to notice is that the exciton binding energy is largest for type I confinement. This can be explained by the localization of both electron and hole in the well region, which increases both the wave function overlap and the Coulomb interaction. Thus, the dielectric confinement is enhanced in type I systems. This result is similar to that of a system with infinite potential barriers as the one discussed in Section 6.4.3 in the main text. However, in this case the effect of quantum confinement on the emission shift and binding energy is less pronounced than for the infinite barriers (Figures 6.11 and D.1).

As the conduction band offset is reduced, the electron gets delocalized and the overlap with the hole and their Coulomb attraction is reduced. The results is a weaker electron-hole interaction and a reduced exciton binding energy for quasi-type I and type II systems (Figure D.3). The effect of the band alignment on the emission shift is also interesting. Both the blue and red shift in strong and weak confinement regimes are strongest for the type I system. In order to understand this, it is worth it to analyze the self-interaction of the carriers ($\left\langle V_i^{self} \right\rangle$, Figure D.4a and b) and the Coulomb interaction ($\langle V_c \rangle$, Figure D.4c) for the different band alignments. On the one hand, the self-interaction of the electron is severely affected by the band alignment, and it increases as ΔE_c decreases, since the potential barrier created by the band mismatch hinders the interaction of carriers inside the well with the induced charges outside. In contrast to the electron, the hole remains localized and the self interaction contribution does not change. The Coulomb interaction, on the other hand, decreases (in magnitude) as a result of the electron delocalization as the ΔE_c decreases. The result of a weaker self- and Coulomb interaction contributions for quasi type I and type two systems is a less pronounced emission shift.

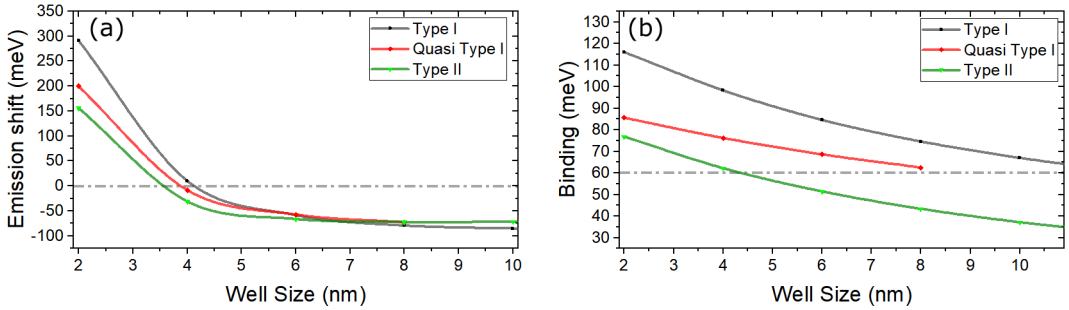

Figure D.3: Calculated (a) emission energy shift and (b) exciton binding energy for a $Cs_4PbBr_6/CsPbBr_3/Cs_4PbBr_6$ system, considering different types of confinement. The effective confinement of both electron and hole in a type I system yields a large exciton binding energy, due to the larger wave function overlap, in comparison with quasi-type I and type II systems. This is also reflected in the emission shift: the type I system exhibits larger blue (red) shift in strong (weak) confinement regimes. The dash-dotted horizontal lines are the zero shift (no shift with respect to the band gap) in (a), and the 60 meV exciton binding energy reported for bulk $CsPbBr_3$

D.2.2 $CsPb_2Br_5/CsPbBr_3/CsPb_2Br_5$ system

A similar calculation was also performed for the $CsPb_2Br_5/CsPbBr_3/CsPb_2Br_5$ system. In this case, $\Delta E_g \simeq 1.4\,\text{eV}$, considering the reported band-gap energies of the phases [19, 56, 58].

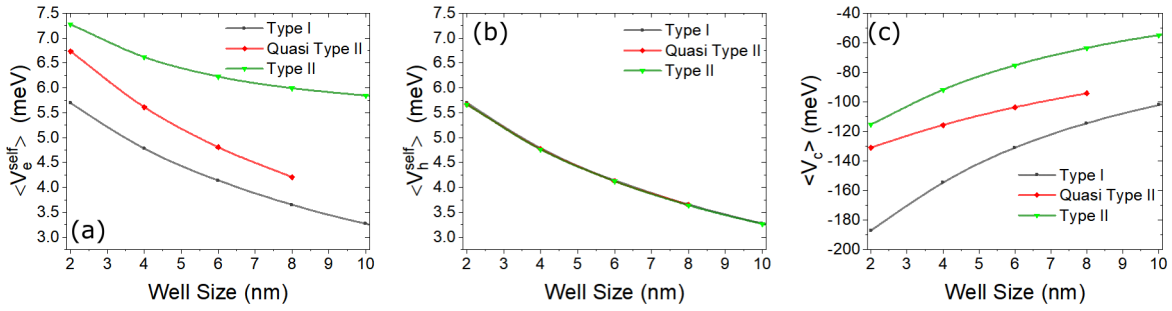

Figure D.4: Calculated (a) electron and (b) hole self-interaction energies as a function of the well size, for different types of confinement. As the electron barrier decreases (type I → type II), the electron self-interaction increases. The hole self-interaction remains unchanged. (c) The Coulomb interaction as a function of the well size, shows the effects of charge delocalization on the electron-hole interaction

Figure D.5 shows the calculated emission shift and binding energy as a function of the well size. The system behaves similarly to the one described above for Cs_4PbBr_6 barriers. However, owing to the smaller ΔE_g and larger dielectric constant, the effects of quantum and dielectric confinement are less pronounced than in the previous model. Therefore, the binding energy, as well as the emission shift, is smaller than in the system described in Section D.2.1 for all the three types of confinement.

In Figure D.5 the emission shift and the binding energy of the system with infinite potential barriers are also shown for comparison. Note that the system confined with infinite potential barriers, even considering the dielectric mismatch effects in a fully correlated way, can lead to overestimation of the blue shift for nanocrystals embedded in a solid matrix. Similar results to those in Figure D.4 were found for the $CsPb_2Br_5$ system.

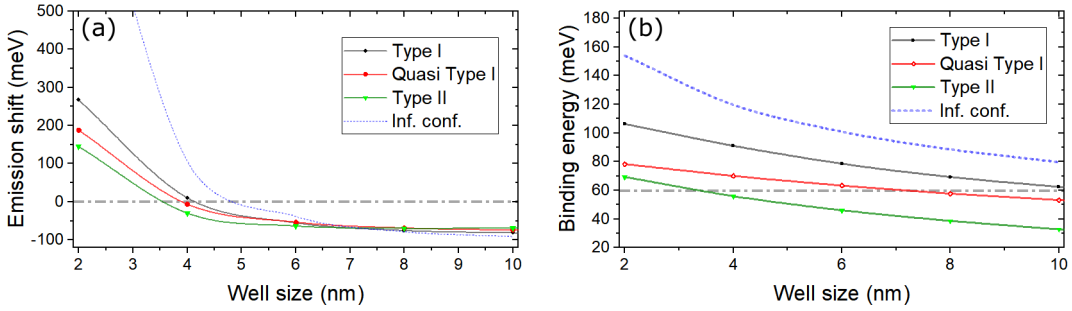

Figure D.5: Calculated (a) emission energy shift and (b) exciton binding energy for a $CsPb_2Br_5/CsPbBr_3/CsPb_2Br_5$ system, considering different types confinement. The results are explained in a similar matter as those in Figure D.3, but for $CsPb_2Br_5$ barriers, the effects of quantum and dielectric confinement are softer owing to the reduced ΔE_g and ε_2. The calculated shift and binding energy for a system confined in an infinite potential well (no band gap mismatch considered) are shown as the dotted blue curves for comparison. The dash-dotted horizontal lines are the zero shift (no shift with respect to the band gap) in (a), and the 60 meV exciton binding energy reported for bulk $CsPbBr_3$

D.2.3 Effect of band alignment in the electron-hole overlap

In contrast to the overlap for type I system (Figure 6.14), that of the quasi type I system is lower and independent of the well size. This particular behavior can be attributed to the differences in localization of electron and hole: while the hole localization depends on the well

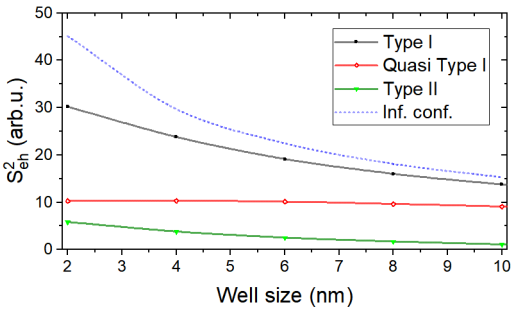

Figure D.6: Calcuated electron-hole overlap for a $CsPb_2Br_5/CsPbBr_3/CsPb_2Br_5$ system as a function of the well size, considering different types of confinement. The overlap of type I system depends strongly on the size, and for larger sizes is comparable to the model with infinite potential barriers (dotted, blue line). The overlap in quasi type I systems is size independent, and that of type II systems only depends weakly on the size.

size, the electron is delocalized owing to the flat conduction band. Therefore, the electron-hole overlap is dominated by the electron degree of localization, and the system is insensitive to the changes in the well size. The enhanced luminescence should be rather insensitive to the nanocrystal size for a quasi-type I system. Finally, for a Type II system, the overlap — and by extension, the oscillator strength — depends weakly on the nanocrystal size. This is attributed to the weak localization of the electron towards the shell (since the system model here considers finite width barrier). However, since electron and hole are localized to different regions, their overlap — and in consequence, luminescence — is low and weakly dependent on the size.

D.2.4 Final remarks

The model proposed here predicts high luminescence for type I strongly confined nanocrystals, resulting from the large electron-hole overlap due to the effective confinement of both carriers. The luminescence is strongly dependent on the size of the nanocrystal, contrary to quasi type I systems with flat conduction band, in which the overlap — and consequently the luminescence — is independent of the size. The transition from net blue to red shift is also dependent on the band alignment: for type I systems the transition takes place at larger nanocrystal sizes than for quasi type I or type II.